

## RECOVERY TECHNOLOGIES: FINAL REPORT

Email the report to [candice.paton@albertainnovates.ca](mailto:candice.paton@albertainnovates.ca)

---

**Project Title: Hydrocarbons in Nanochannels: A Window into Alberta Shale/Tight Oil Production**

**Project Start Date: January 1, 2015**

**Project End Date: August 31, 2019**

**Report Date: August 31, 2019**

---

### CONTACT INFORMATION: PRINCIPAL INVESTIGATOR

**Name: David Sinton**

**Title: Professor**

**Company: University of Toronto**

**Department: Mechanical and Industrial Engineering, and the University of Toronto Institute for Sustainable Energy**

**Address: 5 King's College Rd., Toronto, ON, M5R 3C7**

**Phone: (416) 978-1623**

**Fax: (416) 978-7753**

**Email: [sinton@mie.utoronto.ca](mailto:sinton@mie.utoronto.ca)**

---

---

## Disclaimer

Alberta Innovates – Energy and Environment Solutions (“AI-EES”) and Her Majesty the Queen in right of Alberta make no warranty, express or implied, nor assume any legal liability or responsibility for the accuracy, completeness, or usefulness of any information contained in this publication, nor that use thereof infringe on privately owned rights. The views and opinions of the author expressed herein do not necessarily reflect those of AI-EES or Her Majesty the Queen in right of Alberta. The directors, officers, employees, agents and consultants of AI-EES and the Government of Alberta are exempted, excluded and absolved from all liability for damage or injury, howsoever caused, to any person in connection with or arising out of the use by that person for any purpose of this publication or its contents.

---

## Executive Summary

Production from unconventional shale/tight oil operations is reshaping global energy. The immediate importance of this technology is underscored by the recent increase in North American production, and a marked decrease in oil price – with broad implications in Alberta and Canada. Oil and gas production from fractured reservoirs is governed by complex phase dynamics of hydrocarbon mixtures at high temperature and pressures in nanoscale pores. This is an intensely complex process that is poorly understood. At nanoscales ( $\sim < 100$  nm) significant deviations from classical phase behaviour are expected, though current simulations/models disagree. There is an immediate need for experimental data on the nanoscale phase dynamics central to this process. This project leveraged the expertise, tools, and funding from Schlumberger Canada Ltd. in a 4-year partnership with the Sinton Group at the University of Toronto. The project addressed two process-critical questions: (i) “How are the phase transition conditions for pure hydrocarbons altered in nanopores?” and (ii) “How is the phase change of hydrocarbon mixtures influenced by the combination of nanopores and microfractures, under reservoir conditions?” These measurements focused on (i) reservoir-specific live hydrocarbon mixtures, and (ii) reservoir-specific pore sizes, temperatures and pressures – providing unprecedented insight into Alberta’s tight/shale resources. These measurements were only possible through leveraging collective Schlumberger-NSERC-Alberta Innovates support for new technology development and application. To enable these quantitative measurements, the project leveraged silicon-glass nanofluidic chip technology and high contrast brightfield and darkfield microscopy – a globally distinct approach and competitive advantage. The project directly targeted the AI strategic goals of in Energy (‘production of oil and gas from challenging reservoirs as 15% of total’), with additional benefits in Water and Environmental Management (‘improving the overall efficiency and productivity of water use in Alberta by 30 %’). In addition to the method development and technical findings relevant to operators, service companies, policy makers and the public, this technology is being commercialized through our AB-based startup, Interface Fluidics Ltd, and attracting customers and investors worldwide.

Keywords: Microfluidics, Nanofluidics, Phase-change, Tight oil, Hydrocarbon mixtures

# Table of Contents

1.	Introduction.....	5
2.	Project Description	
	• Challenge .....	6
	• Goals set for this project.....	6
3.	Approach and Results	
	• Literature review.....	10
	• Technology development.....	23
	• Experimental procedures.....	29
	• Results and discussions.....	40
	• Project outcomes.....	72
4.	Relevance and Impact.....	75
5.	Overall Conclusions.....	76
6.	Next Steps.....	78
7.	Scientific Achievements.....	79
8.	Financial Report.....	81

# 1. Introduction

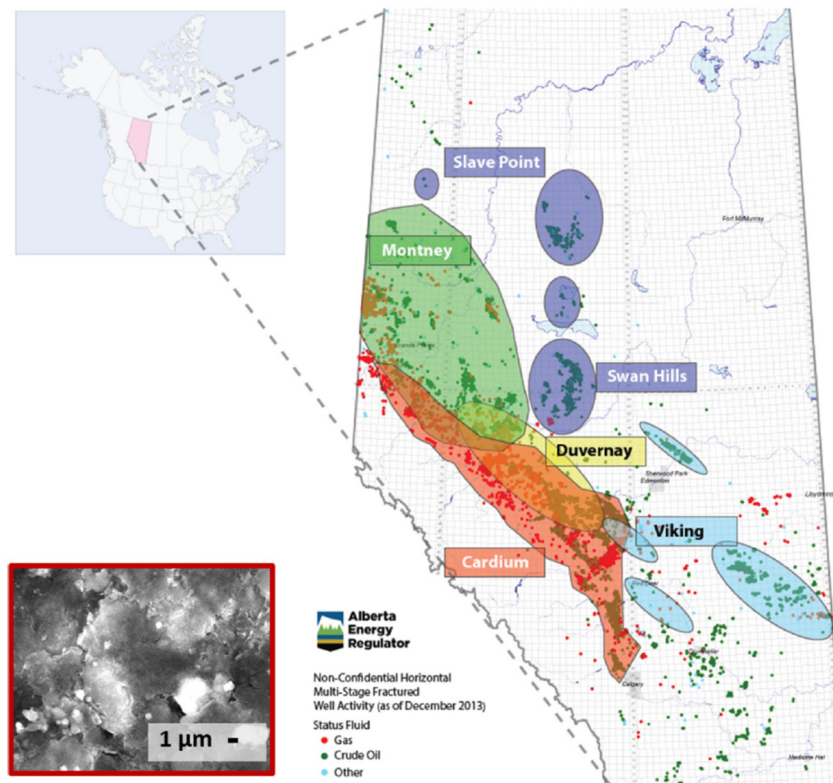


Figure 1 Prospective shale/tight oil basins in Canada (map c/o Alberta Energy Regulator), with nanostructure of a representative shale formation shown inset.

Oil and gas production from fractured reservoirs in Alberta (Figure 1) is dictated by a complex interplay of hydrocarbon mixtures and water-based fracture fluids, at high temperature and pressure, flowing and expanding through natively nano-porous rock, and induced *micro*-fractures that can include both hydrophilic and hydrophobic regions<sup>1,2</sup>. Briefly, after drilling a horizontal well in the shale formation, water (brine) containing different additives is injected through the well at sufficiently high pressure to break into the formation and create a network of fractures connected to the well. The artificially induced fractures may connect and/or open the existing natural fractures, and small particles called proppants included in the fracture fluid ensure the fractures stay open. Once the fracture pressure is relieved (pressure drawdown), production can occur with hydrocarbons expanding from nanoscale pores into progressively larger fractures and eventually to the well. This is a complex process that is poorly understood, a “blank page with huge impact” as noted in a recent review<sup>3</sup>. The immediate need for fundamental and applied research in this area is underscored by both a 2014 special issue of *Science*<sup>4</sup>, and a 2014 report by the Council of Canadian Academies<sup>5</sup>.

Nanofluidics for energy applications has received minimal attention. With the rapid emergence of hydraulic fracturing, this area requires immediate attention – as noted in both my recent review on energy<sup>6</sup> and a thoughtful review on nanofluidics<sup>3</sup> published in the same issue. It is noteworthy that

some in the oil and gas research community are starting to develop nanofluidic systems to study hydrocarbon transport<sup>7,8</sup>. These recent studies show a rich and complicated physics, with significant deviation from classical theory in terms of capillary pressure [8] and interface shape<sup>8,9</sup>. In addition, recent data for pure water shows a significant increase in apparent viscosity reduction at nanoscales, depending on the surface condition<sup>10</sup>. For hydrocarbons, there is effectively no experimental data available on hydrocarbon phase transitions in nanochannels at reservoir-relevant conditions. Real reservoirs present additional complexities of hydrocarbon mixtures, large molecules (analogous to DNA nanofluidics<sup>11</sup>), complex fracture fluids, and high temperatures and pressures. The little data available on nanoconfined hydrocarbons indicate significant deviations from bulk behaviour is expected at sub-100nm scales, and is likely to be compounded at reservoir conditions. This currently unknown physics is critical to process effectiveness, safety, and environmental impact.

1. A. Yethiraj, A. Striolo, Fracking: What Can Physical Chemistry Offer?, *J. Phys. Chem. Lett.* (2013) 687–690.
2. P.J.M. Monteiro, C.H. Rycroft, G.I. Barenblatt, A mathematical model of fluid and gas flow in nanoporous media, *Proc. Natl. Acad. Sci. U. S. A.* 109 (2012) 20309–20313.
3. L. Bocquet, P. Tabeling, Physics and technological aspects of nanofluidics, *Lab Chip.* 14 (2014) 3143–3158.
4. D. Malakoff, The gas surge, *Science* 344 (2014) 1464–1467.
5. Council/of/Canadian/Academies, Environmental Impacts of Shale Gas Extraction, 2014.
6. D. Sinton, Energy: the microfluidic frontier, *Lab Chip.* 14 (2014) 3127–3134.
7. Q. Wu, B. Bai, Y. Ma, J.T. Ok, K.B. Neeves, X. Yin, SPE 164549 Optic Imaging of Two-Phase Flow Behaviour in 1D Nanoscale Channels, in: *SPE*, 2014.
8. S. Kelly, SPE 167635 Experimental Investigation of the Influence of Molecular Surface Interactions on Imbibition in Shale Nano-Pore Proxies, in: *SPE*, 2013.
9. P. Kim, H.-Y. Kim, J.K. Kim, G. Reiter, K.Y. Suh, Multi-curvature liquid meniscus in a nanochannel: evidence of interplay between intermolecular and surface forces, *Lab Chip.* 9 (2009) 3255–3260.
10. D. Ortiz-Young, H.-C. Chiu, S. Kim, K. Voitchovsky, E. Riedo, The interplay between apparent viscosity and wettability in nanoconfined water., *Nat. Commun.* 4 (2013) 2482.
11. E. Orlandini, C. Micheletti, Knotting of linear DNA in nano-slits and nano-channels: a numerical study, *J. Biol. Phys.* 39 (2013) 267–75.

## 2. Project Description

### 2.1 Challenge

There is a growing scientific interest in the booming shale industry, for both environmental and economic reasons. The fundamental complexity at the heart of the shale resource production inefficiency, as well as its environmental impact is, termed here, a “two-mixture” problem. That is, the thermodynamic and fluidic complexities derive from the nature of multi-component fluid mixtures within radically multi-scale “mixed” geometry systems (numerous nanopores at different scales connected by macro fractures) – a fluid mixture, within a mixture of lengthscales. A clear understanding of fundamental fluid behaviors in these systems is an essential piece of the shale puzzle.

Current methodologies in studying fluid behaviors in shale mainly rely on theoretical simulation or experimental core tests. The limitation for simulation is that, at the shale pore relevant scale – nanoscale, classical theories potentially fall, and theoretical assumptions need to be validated through highly controlled and repeated experimental results. While for core tests, due to the extremely tight shale formations, shale core tests usually take a long period (months) and the repeatability is low. While simulations and core experiments will continue to be important methods, however, there is a gap that nanofluidic experiments can address, providing real nanopore scale resolution of processes in shale nanoporous reservoirs.

### 2.2 Goals and Technologies

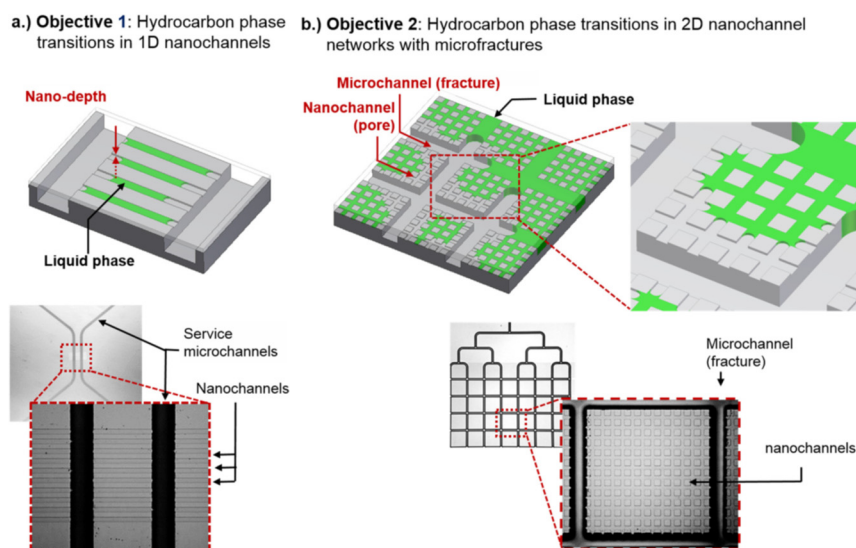


Figure 2 Schematic illustration of the experimental setups employed in this project. Images in the lower panes show the fabricated micro/nanofluidic structures at multiple scales. The nanochannels for the cases shown are  $\sim 10 \mu\text{m}$  wide and  $\sim 100 \text{ nm}$  deep.

A two-pronged approach was applied, as addressed through two concurrent project segments (I & II), with details shown schematically in Figure 2, and detailed below:

**I. Hydrocarbon phase transitions in 1D nanochannels (Figure 2a):** To quantify deviations in liquid-gas hydrocarbon phase transition pressure in nanochannels as compared to micro/bulk conditions. Specifically, for a given test temperature we will (i) quantify the liquid-to-gas phase transition pressure within the nanochannels and (ii) image the shape and velocity of the liquid-gas interface during evaporation. Results of both (i) and (ii) will be compared with associated bulk and microscale tests, and with reference to the Kelvin equation. This segment will focus on pure hydrocarbons and hydrocarbon mixtures relevant to Montney and Viking formations.

Goal	Reporting Period Due	Status
Benchmark low pressure/process testing complete	Year 1	Completed
Montney and Viking pressure/process operation validated	Year 2	Completed
Preliminary full data range for Montney and Viking	Year 3	Completed
Schlumberger-validated full data range for Montney and Viking	Year 4	Completed

**Table 1.** 4-year goals of segment I of project

**II. Hydrocarbon phase transitions in 2D nanochannel networks with microfractures (Figure 2b):** To quantify retention of liquid hydrocarbons in nanopores within with reservoir-relevant fluids (i.e. hydrocarbon mixtures), temperatures and pressures. Specifically, for a given test temperature we (i) quantified the volume of liquid remaining within the nanochannel network as a function of draw-down pressure, and (ii) imaged the evolution of the liquid phase during evaporation. Results of both (i) and (ii) were compared as a function of nanochannel depth (ranging from 10 nm to 200 nm). This segment focused on reservoir-relevant hydrocarbon mixtures that necessarily exhibit a two-phase region. Of particular interest was how the presence of nanochannels can influence the phases present under such reservoir-relevant conditions.

Goal	Reporting Period Due	Status
Loading and draw-down process testing complete	Year 1	Completed
Montney and Viking pressure in micromodel validated	Year 2	Completed
Preliminary full data range for drawdown with Montney and Viking conditions	Year 3	Completed
analysis of Montney and Viking pore and fracture size influence on phase behaviour	Year 4	Completed

---

in those reservoirs, under  
reservoir-relevant conditions

---

**Table 2.** 4-year goals of segment II of project

## 3. Approach and Results

This progress report focuses on the work done in Segment I and II. Seven components were conducted in Segment I and Segment II: (1) single component hydrocarbon condensation in 1-D sub-100 nm channels, (2) single component hydrocarbon condensation in 1-D sub-10 nm channels, (3) single component hydrocarbon bubble nucleation in 1-D sub-100 nm channels, (4) mixture hydrocarbon phase behavior at a mixed nano-macro length scale, (5) single component hydrocarbon evaporation in 2-D sub-10 nm nanogrids, (6) 2-D nanogrids in screening enhanced tight oil recovery strategies, (7) 2-D nanogrids in simulating shale gas primary recovery.

All have produced important results, the first Segment explores fundamental phase change thermodynamics of hydrocarbon mixtures within a fracture-nanopore connected structure. The second Segment starts from fundamental hydrocarbon phase change, to industrial application. One project applies light oil highly relevant to the Montney and Viking reservoirs at ~60 nm pore scale, and tests different gas injections strategies for enhanced tight oil recovery. Another project includes a system designed for the Montney and Viking tests with both large nanopores (~100 nm) connected by a small nanothroat (~5 nm). In addition, a start-up (Interface Fluidics Ltd.) founded in Alberta within this period by our previous lab members is now providing services for industries with a nanofluidic approach that benefited from the foundational work here.

### 3.1 Literature review

#### **Component 1: Single component hydrocarbon condensation in 1-D sub-100 nm channels**

Phase change and fluid flow at the nanoscale play important roles in the environment<sup>1-3</sup> and unconventional oil and gas recovery<sup>4-6</sup>. To understand these systems, it is crucial to understand phase change of nanoconfined reservoir fluids, particularly as reservoir pressurization and depressurization alter the phase state<sup>8</sup>. Despite the emergence and global importance of unconventional oil and gas recovery, the fundamental physics governing phase change at the nanoscale remains poorly understood, and the available classical theories and simulation techniques have proven to be inadequate<sup>7</sup>.

As system size decreases, the classical approach for studying phase change starts to fail<sup>9</sup>. For the condensation process specifically, the condensate growth will drive vapor flow at the nanoscale. When the characteristic length of the system ( $h$ ) becomes close to the mean free path of the vapor molecule ( $l$ ), the flow behavior can deviate from the bulk behavior predicted by the Navier-Stokes equations<sup>10</sup>, and affect the condensate growth process. Furthermore, at very small scales the saturation pressure can change as a result of liquid-gas curvature (known as the capillary condensation<sup>11</sup>). The condensation process is a vapor-to-liquid phase transition, and there is a profound need for targeted experiments and theory to better understand this phenomenon<sup>7,9</sup>.

Optically accessible nanofabricated channels can provide a much needed window into the relevant phase phenomena at these scales.

In this component, we study condensation and condensate growth of a pure substance in sub-100 nm confinement using propane as a model fluid. Two different condensation mechanisms at the nanoscale are distinguished and compared with previous simulation results<sup>12,13</sup>: continuous growth, and discontinuous growth due to liquid bridging ahead of the meniscus. The directly observed effects of pressure and temperature on the condensate growth and growth rate are compared with those predicted by a developed thermo-fluid resistance model. In contrast to phase change at larger scales, where heat and mass transfer processes at the liquid-vapor interface dominate the condensation and condensate growth process<sup>14,15</sup>, the rate of liquid condensate growth is found to be limited mainly by vapor flow resistance in channels at the nanoscale. These findings illustrate the condensation and condensate growth of a pure substance in nanoporous systems, which deviates from bulk conditions.

- 1 Ehn, M.; Thornton, J. A.; Kleist, E.; Sipilä, M.; Junninen, H.; Pullinen, I.; Springer, M.; Rubach, F.; Tillmann, R.; Lee, B., A Large Source of Low-Volatility Secondary Organic Aerosol. *Nature* 2014, 506 (7489), 476-479.
- 2 Kulmala, M.; Kontkanen, J.; Junninen, H.; Lehtipalo, K.; Manninen, H. E.; Nieminen, T.; Petäjä, T.; Sipilä, M.; Schobesberger, S.; Rantala, P., Direct Observations of Atmospheric Aerosol Nucleation. *Science* 2013, 339 (6122), 943-946.
- 3 Bones, D. L.; Reid, J. P.; Lienhard, D. M.; Krieger, U. K., Comparing the Mechanism of Water Condensation and Evaporation in Glassy Aerosol. *Proceedings of the National Academy of Sciences* 2012, 109 (29), 11613-11618.
- 4 Patzek, T. W.; Male, F.; Marder, M., Gas Production in the Barnett Shale Obeys a Simple Scaling Theory. *Proceedings of the National Academy of Sciences* 2013, 110 (49), 19731-19736.
- 5 Monteiro, P. J.; Rycroft, C. H.; Barenblatt, G. I., A Mathematical Model of Fluid and Gas Flow in Nanoporous Media. *Proceedings of the National Academy of Sciences* 2012, 109 (50), 20309-20313.
- 6 Kar, A.; Chiang, T.-Y.; Ortiz Rivera, I.; Sen, A.; Velegol, D., Enhanced Transport into and out of Dead-End Pores. *ACS nano* 2015, 9 (1), 746-753.
- 7 Cueto-Felgueroso, L.; Juanes, R., Forecasting Long-Term Gas Production from Shale. *Proceedings of the National Academy of Sciences* 2013, 110 (49), 19660-19661.
- 8 Devegowda, D.; Sapmanee, K.; Civan, F.; Sigal, R. F. In *Phase Behavior of Gas Condensates in Shales Due to Pore Proximity Effects: Implications for Transport, Reserves and Well Productivity*, SPE Annual Technical Conference and Exhibition, Society of Petroleum Engineers: 2012.
- 9 Li, D., *Encyclopedia of Microfluidics and Nanofluidics*. Springer Science & Business Media: 2008.
- 10 Ali Beskok, G. E. K., Report: A Model for Flows in Channels, Pipes, and Ducts at Micro and Nano Scales. *Microscale Thermophysical Engineering* 1999, 3 (1), 43-77.
- 11 Fisher, L.; Gamble, R.; Middlehurst, J., The Kelvin Equation and the Capillary Condensation of Water. *Nature* 1981, 290 (5807).
- 12 Nguyen, P. T.; Do, D.; Nicholson, D., On the Irreversibility of the Adsorption Isotherm in a Closed-End Pore. *Langmuir : the ACS journal of surfaces and colloids* 2013, 29 (9), 2927-2934.
- 13 Schneider, D.; Valiullin, R.; Monson, P. A., Filling Dynamics of Closed End Nanocapillaries. *Langmuir : the ACS journal of surfaces and colloids* 2014, 30 (5), 1290-1294.
- 14 Shekriladze, I.; Gomelauri, V., Theoretical Study of Laminar Film Condensation of Flowing Vapour. *International Journal of Heat and Mass Transfer* 1966, 9 (6), 581-591.
- 15 Chen, Y.; Shi, M.; Cheng, P.; Peterson, G., Condensation in Microchannels. *Nanoscale and Microscale Thermophysical Engineering* 2008, 12 (2), 117-143.

## Component 2: Single component hydrocarbon condensation in 1-D sub-10 nm channels

Substantial deviations of fluid dynamics from bulk conditions can result at sub-10 nm scales. New methods and associated studies at this scales reveal a rich and complicated physics which remain largely unknown. For example, pioneering studies in channels between 40-100 nm have reported that the effective bulk liquid-phase viscosity increases by as much as 40% in nanoconfinement,<sup>1,2</sup> while others have claimed that the effective viscosity decreases.<sup>3</sup> At smaller, sub-10 nm scales, existing methods for direct visualization are ineffective. For example, Severin et al. studied water wetting dynamics in 1-nm confinement, but were unable to use optical microscopy at such small

scales. Instead, they used scanning force microscopy (SFM), but could not resolve the fluid dynamics due to the scan time limitation of 4 minutes per image.<sup>4</sup> Conversely, indirect methods, such as measuring volumetric flow rates in larger neighboring channels gives an average description of the sub-10 nm nanofluidic dynamics,<sup>5</sup> but cannot resolve local fluid dynamics. Thus, fluid dynamics at the sub-10 nm scale remains poorly understood and there is an urgent need for direct experimental methods.

Optical microscopy is the predominant method used to directly visualize fluid dynamics in channels (>20 nm), and a staple of experiments in capillary filling,<sup>5-7</sup> evaporation,<sup>8,9</sup> cavitation,<sup>10</sup> and condensation.<sup>11,12</sup> However, upon decreasing the channel height to sub-10 nm scales, the ultra-short optical path in the channel results in a negligible phase difference between liquid and gas, providing insufficient optical contrast for discrimination between the fluid phases.

Several methods exist to differentiate fluid phases at sub-10 nm scales, including soluble fluorescent dyes,<sup>13,14</sup> differential interference contrast (DIC) imaging,<sup>7</sup> and Fabry-Perot interferometry.<sup>15</sup> However, dyes can change the thermophysical properties of fluids under test, and suffer photobleaching at long exposure times; DIC does not sufficiently distinguish different fluid phases in sub-10 nm channels; and micro Fabry-Perot interferometers require elaborate fabrication and specific geometries and surface materials in order to integrate the requisite silver mirrors. In light of these challenges, transmission electron microscope (TEM) has been used to study the in-situ fluid dynamics in nanotubes with sub-10 nm dimensions,<sup>16</sup> but TEM can only image static fluid dynamics in closed nanotubes with thin walls, and there are additional restrictions in terms of test liquids due to the autoclave treatment required for filling.<sup>11</sup>

In this component, we demonstrate an optical microscopy-based method to directly visualize liquid and gas phases in sub-10 nm slit-nanochannels. Central to this approach is the Si<sub>3</sub>N<sub>4</sub> layer below the nanochannel, the thickness of which is crucial for achieving contrast. This layer plays an additional role in avoiding channel collapse during the anodic bonding process. We demonstrate this approach by directly observing capillary filling in 8-nm high channels with a variety of test fluids (water, hexane, octane, and hexadecane). Our filling experiments do not indicate any significant change to bulk fluid properties at the sub-10 nm scale. This result is surprising in light of recent work indicating the need to modify the bulk viscosity in order for classical theories to match with filling experiments in nanochannels, at even larger scales (40-100 nm).

1. N. R. Tas, J. Haneveld, H. V. Jansen, M. Elwenspoek and A. van den Berg, *Appl. Phys. Lett.*, 2004, 85, 3274-3276.
2. N. A. Mortensen and A. Kristensen. *Appl. Phys. Lett.*, 2008, 92, 063110.
3. F. Calabrò, K. P. Lee and D. Mattia, *Appl. Math. Lett.*, 2013, 26, 991-994.
4. N. Severin, P. Lange, I. M. Sokolov and J. P. Rabe, *Nano Lett.*, 2012, 12, 774-779.
5. M. A. Alibakhshi, Q. Xie, Y. Li and C. Duan, *Sci. Rep.*, 2016, 6, 24936.
6. D. Schneider, R. Valiullin and P. A. Monson, *Langmuir*, 2014, 30, 1290-1294.
7. J. Haneveld, N. R. Tas, N. Brunets, H. V. Jansen and M. Elwenspoek, *J. Appl. Phys.*, 2008, 104, 014309.
8. V. N. Phan, N. T. Nguyen, C. Yang, P. Joseph and A. M. Gué, *J. Heat Transfer*, 2012, 134, 051012.
9. T. Tsukahara, T. Maeda, A. Hibara, K. Mawatari and T. Kitamori, *RSC Adv.*, 2012, 2, 3184-3186.
10. C. Duan, R. Karnik, M. C. Lu and A. Majumdar, *Proc. Natl. Acad. Sci. U.S.A.*, 2012, 109, 3688-3693.
11. M. P. Rossi, H. Ye, Y. Gogotsi, S. Babu, P. Ndungu and J. C. Bradley, *Nano Lett.*, 2004, 4, 989-993.
12. J. Zhong, S. H. Zandavi, H. Li, B. Bao, A. H. Persad, F. Mostowfi and D. Sinton, *ACS Nano.*, 2017, 11, 304-313.
13. J. Gu, R. Gupta, C. Chou, Q. Wei and F. Zenhausern, *Lab Chip*, 2007, 7, 1198-1201.
14. D. Xia, J. Yan and S. Hou, *Small*, 2012, 8, 2787-2801.
15. K. M. van Delft, J. C. T. Eijkel, D. Mijatovic, T. S. Druzhinina, H. Rathgen, N. R. Tas, A. van den Berg and
16. F. Mugele, *Nano Lett.*, 2007, 7, 345-350.
17. N. Naguib, H. Ye, Y. Gogotsi, A. G. Yazicioglu, C. M. Megaridis and M. Yoshimura, *Nano Lett.*, 2004, 4, 2237-2243.

### Component 3: Single component hydrocarbon bubble nucleation in 1-D sub-100 nm channels

The pores in shale and tight oil formations are mostly nano-sized (few to tens of nanometers), necessitating fundamental understanding of fluid phase and transport properties of nanoconfined reservoir fluids, particularly as pressurization and depressurization alter the phase state<sup>1,2, 3-5</sup>. The fundamental physics governing phase change at the nanoscale remains poorly understood, and the available classical theories and simulation techniques have proven inadequate<sup>3</sup>.

Liquids at temperatures above (or pressures below) the saturation become metastable and susceptible to transform to a stable vapor phase via vapor bubble nucleation (cavitation or boiling)<sup>6</sup>. A review of experimental approaches for measuring the limit of metastability of liquids in the bulk/macro systems can be found elsewhere<sup>7,8</sup>. Significant discrepancies between experimental results and classical homogeneous nucleation theory have been reported<sup>9,10</sup>. These discrepancies are usually attributed to differences in surface tension<sup>11,12</sup>, surface roughness and channel corrugations<sup>9,12,13</sup>, heterogeneity in wetting<sup>9,10,14</sup>, external perturbations<sup>9</sup>, and/or the presence of bubbles or particles<sup>9</sup>.

Recent advances in micro- and nano-technology allow the investigation of fluid phase transition in structures at this scale. Ando et al.<sup>15</sup> reported homogeneous bubble nucleation achieved by a laser-induced shock on a free surface in micro-fluidic channels. Nagashima et al.<sup>16</sup> detected a single bubble nucleation in a single nanopore with the radius of 43.5 nm by extreme pulsed superheating. Vincent et al.<sup>17</sup> observed the bubble nucleation and growth during the drying process of water in the ink-bottle nanostructure and found that the liquid phase pressure at cavitation was less negative than that expected from the nucleation theory. Witharana et al.<sup>18</sup> found that larger micrometer-sized cavities nucleate vapor at a lower superheated temperature than smaller nanometer-sized cavities. Duan et al.<sup>19</sup> reported evaporation-induced cavitation of water in 20-120 nm deep nanochannels. Collectively these relatively recent results indicate a rich and complex physics, deviating significantly from bulk behavior.

Here, we study the liquid-to-vapor phase transition of propane in sub 100-nm channels under isothermal pressure drawdown process. The micro/nanofluidic chip allows direct visualization of bubble nucleation and growth. The measured nucleation temperatures and pressures are compared with nucleation theory. We also investigate the growth rate of vapor bubble column after nucleation. Two growth mechanisms are distinguished, with results compared to a fluid dynamics model for evaporation rate, liquid velocity, and bubble pressure.

- 1 D. Malakoff, *Science* (80-. ). 344, 1464 (2014).
- 2 T. W. Patzek, F. Male, and M. Marder, *Proc. Natl. Acad. Sci. U. S. A.* 110, 19731 (2013).
- 3 L. Cueto-Felgueroso and R. Juanes, *Proc. Natl. Acad. Sci.* 110, 19660 (2013).
- 4 P. J. M. Monteiro, C. H. Rycroft, and G. I. Barenblatt, *Proc. Natl. Acad. Sci.* 109, 20309 (2012).
- 5 B. Bai, M. Elgmati, H. Zhang, and M. Wei, *Fuel* 105, (2013).
- 6 T. D. Wheeler and A. D. Stroock, *Nature* 455, 208 (2008).
- 7 F. Caupin and E. Herbert, *Comptes Rendus Phys.* 7, 1000 (2006).
- 8 C. T. Avedisian, *J. Phys. Chem. Ref. Data* 14, 695 (1985).
- 9 C. E. Brennen, *Cavitation and Bubble Dynamics* (Oxford University Press, Oxford, 1995).
- 10 I. T. Chen, D. A. Sessoms, Z. M. Sherman, E. Choi, O. Vincent, and A. D. Stroock, *J Phys Chem B* 120, 5209 (2016).
- 11 N. Bruot and F. Caupin, *Phys. Rev. Lett.* 116, 1 (2016).
- 12 M. E. M. Azouzi, C. Ramboz, J.-F. Lenain, and F. Caupin, *Nat. Phys.* 9, 38 (2013).
- 13 T. Hoffman, D. Wallacher, P. Jan, S. Koyiloth Vayalil, and H. Patrick, *Langmuir* 32, 2928 (2016).

- 14 C. J. Rasmussen, G. Y. Gor, and A. V. Neimark, *Langmuir* 28, 4702 (2012).  
15 K. Ando, A. Q. Liu, and C. D. Ohl, *Phys. Rev. Lett.* 109, 1 (2012).  
16 G. Nagashima, E. V. Levine, D. P. Hoogerheide, M. M. Burns, and J. A. Golovchenko, *Phys. Rev. Lett.* 113, 1 (2014).  
17 O. Vincent, D. A. Sessoms, E. J. Huber, J. Guioth, and A. D. Stroock, *Phys. Rev. Lett.* 113, 1 (2014).  
18 S. Witharana, B. Phillips, S. Strobel, H. D. Kim, T. McKrell, J. B. Chang, J. Buongiorno, K. K. Berggren, L. Chen, and Y. Ding, *J. Appl. Phys.* 112, (2012).  
19 C. Duan, R. Karnik, M.-C. Lu, and A. Majumdar, *Proc. Natl. Acad. Sci.* 109, 3688 (2012).

#### **Component 4: Mixture hydrocarbon phase behavior at a mixed nano-macro length scale**

Due to the presence of extensive nanopores networks in kerogen and clay minerals, where significant amounts of hydrocarbons are believed to be stored, the permeability of shale is extremely low<sup>1-4</sup>. Fracturing methods such as hydraulic fracturing<sup>5</sup>, while controversial<sup>6</sup>, are commonly employed to create additional connections between nanopores in addition to the natural macro fractures. Hydrocarbons confined in nanopores are then released into macro fractures and produced under pressure and chemical potential gradients<sup>2</sup>. The fundamental complexity here lies in the hydrocarbon mixture phase behavior in a multi-scale system (numerous nanopores connected by macro-scale fractures). Fundamental understanding of the thermodynamics in these complex systems is critical to estimate production<sup>7</sup>, reduce decline rates<sup>8</sup>, and assess potential enhanced oil recovery strategies<sup>9</sup>. More broadly, nanoscale thermodynamics of fluid mixtures has relevance to renewable energy technologies such as CO<sub>2</sub> conversion via electro/photo-catalysis<sup>10-12</sup> and fuel cells<sup>13</sup>, where various fluid mixtures are flowed through nanoporous materials to enhance chemical reactions<sup>14</sup>.

Previous work aimed at understanding the nanoscale thermodynamic properties of fluid mixtures have employed computations<sup>15</sup>. A large number of computational works based on equation of state (EOS) coupled with capillarity predict that the bubble point pressure of nano-confined hydrocarbon mixtures is reduced<sup>16-19</sup>, which has a significant impact on the prediction of well performance and ultimate oil recovery in shale/tight oil reservoirs<sup>20</sup>. These results have been incorporated into reservoir simulators (e.g., UTcomp) to predict shale well productivity and conduct history matching. However, these computational approaches are limited in that their theoretical basis is classical bulk-scale thermodynamics and fluid mechanics<sup>15</sup>. At the nanoscale, the fluid properties are additionally affected by fluid-surface interactions and surface adsorption<sup>21-23</sup>. Particularly, given the complexity of systems of fluid mixtures in connected multi-scale geometries, experimental verification of classical theory and computational results is valuable. The central challenges for experiments are creating representative nanoconfined geometries and accurately probing the dynamics within. For example, unconsolidated nanoporous media has been used to study water-related transport<sup>24-28</sup> and hydrocarbon capillary condensation<sup>29</sup>. However, the internal nanopores are distributed within a range (e.g., SBA-15, 2-5 nm)<sup>30</sup>, and the fluid behaviour throughout the volume is not directly optically accessible. As a result, even using the same experimental method (e.g., Differential Scanning Calorimetry)<sup>31-32</sup>, researchers have obtained different results (e.g., unique or dual mixture vaporization points in nanopores). Other approaches such as using a surface force apparatus<sup>33</sup> can generate nanoconfinement without using nanoporous media and have been used to study the capillary condensation of hydrocarbon mixture where force is the direct measurand. While applicable to condensation, this approach is not currently applicable to the bubble nucleation phenomena of importance to tight oil and shale gas. Nanofluidic devices have been used to study ion transport in water<sup>34-35</sup>. The adoption of nanofluidic methods has recently enabled the fabrication of precise silicon-based nanochannels with dimensions of a few

nanometers<sup>36</sup> and with direct optical access<sup>37</sup>, providing ideal controlled confinement suitable for probing fundamental thermodynamic and transport phenomena at the nanoscale to the exclusion of other factors. The silicon/silica surface is oil-wet<sup>36</sup>, whereas in kerogen the surface is expected to be more heterogeneous. The uniform oil-wet surface condition here provides a relevant and controlled surface for fundamental tests of interest. Additionally, silicon fluidics are robust at both high temperatures and pressures<sup>38</sup>, and have been applied to quantify phase change of single-component fluids at the nanoscale<sup>39-42</sup>. Complex hydrocarbon fluid mixtures have been employed routinely in microscale systems<sup>43-44</sup>, where classical thermodynamics is readily applicable. While collectively these efforts have enriched our understanding, they have not captured the inherently coupled complexity of fluid mixture thermodynamics in the mixed nano-macro geometries.

In this component, we directly visualize the phase transition of a sample hydrocarbon mixture (methane: propane = 1:4, mole ratio) in connected channels spanning four orders of magnitude (~10 nm to 10  $\mu$ m). The binary mixture chosen here is somewhat simplified. Shale gas mixtures are generally more complex in composition, although light components (methane, ethane and propane) dominate (>90%). Nanochannels are connected to a deep microchannel to simulate shale nanopores connected to larger pores or fractures (natural or induced). We observe early condensation under nanoconfinement, and with support from density functional theory we attribute this effect to a combination of capillarity and preferential adsorption of the heavy component. We observe late vaporization under nanoconfinement, occurring at system pressure below the bulk dew point in a near-equilibrium pressure drawdown process relevant to long-term shale oil production. During this process, methane is released and the propane accumulates in the nanochannel because of both competitive adsorption and preferential evaporation of methane into the relatively large connected microchannel. Nevertheless, in a fast non-equilibrium pressure drawdown process, the molecular exchange between nanochannel and microchannel is limited, and the nanochannel can be effectively isolated. Cavitation in that case occurs above the bulk dew point. These initial bubbles either collapse or grow depending on channel size and its relation to the unstable bubble equilibrium radius. Collectively these findings show that during the primary shale gas/oil recovery, heavy hydrocarbon components are likely to be trapped inside the nanopores with mostly light components released to the fracture to be produced, resulting in a deeply suppressed mixture bubble point in nanoconfinement. Such a scenario would dampen shale gas production by trapping the valuable heavy fraction, but may be favorable to shale oil operation by effectively restricting bubble formation in nanopore throats and maintaining some liquid connectivity during pressure drawdown. Our findings provide fundamental insight into the physics of connected nanopore systems, with implications for reserve estimations and energy security more generally.

1. Hughes, J. D., Energy: a reality check on the shale revolution. *Nature* 2013, 494, 307.
2. Lee, T.; Bocquet, L.; Coasne, B., Activated desorption at heterogeneous interfaces and long-time kinetics of hydrocarbon recovery from nanoporous media. *Nat. Commun.* 2016, 7, 11890.
3. Yang, J.; Hatcherian, J.; Hackley, P. C.; Pomerantz, A. E., Nanoscale geochemical and geomechanical characterization of organic matter in shale. *Nat. Commun.* 2017, 8, 2179.
4. Falk, K.; Coasne, B.; Pellenq, R.; Ulm, F.-J.; Bocquet, L., Subcontinuum mass transport of condensed hydrocarbons in nanoporous media. *Nat. Commun.* 2015, 6, 6949.
5. Montgomery, C. T.; Smith, M. B., Hydraulic fracturing: history of an enduring technology. *J. Pet. Technol.* 2010, 62, 26-40.
6. Howarth, R. W.; Ingraffea, A.; Engelder, T., Natural gas: should fracking stop? *Nature* 2011, 477, 271.
7. Zhao, X.; Rui, Z.; Liao, X.; Zhang, R., A simulation method for modified isochronal well testing to determine shale gas well productivity. *J. Nat. Gas Sci. Eng.* 2015, 27, 479-485.
8. Patzek, T. W.; Male, F.; Marder, M., Gas production in the Barnett Shale obeys a simple scaling theory. *Proc. Natl. Acad. Sci.* 2013, 110, 19731-19736.

9. Sheng, J. J., Enhanced oil recovery in shale reservoirs by gas injection. *J. Nat. Gas Sci. Eng.* 2015, 22, 252-259.
10. Kim, T. W.; Choi, K.-S., Nanoporous BiVO<sub>4</sub> photoanodes with dual-layer oxygen evolution catalysts for solar water splitting. *Science* 2014, 1245026.
11. Kas, R.; Hummadi, K. K.; Kortlever, R.; De Wit, P.; Milbrat, A.; Luiten-Olieman, M. W.; Benes, N. E.; Koper, M. T.; Mul, G., Three-dimensional porous hollow fibre copper electrodes for efficient and high-rate electrochemical carbon dioxide reduction. *Nat. Commun.* 2016, 7, 10748.
12. Lu, Q.; Rosen, J.; Zhou, Y.; Hutchings, G. S.; Kimmel, Y. C.; Chen, J. G.; Jiao, F., A selective and efficient electrocatalyst for carbon dioxide reduction. *Nat. Commun.* 2014, 5, 3242.
13. Debe, M. K., Electrocatalyst approaches and challenges for automotive fuel cells. *Nature* 2012, 486 (7401), 43.
14. Luc, W.; Jiao, F., Nanoporous Metals as Electrocatalysts: State-of-the-Art, Opportunities, and Challenges. *ACS Catal.* 2017, 7, 5856-5861.
15. Salahshoor, S.; Fahes, M.; Teodoriu, C., A review on the effect of confinement on phase behavior in tight formations. *J. Nat. Gas Sci. Eng.* 2017, 51, 89-103.
16. Luo, S.; Lutkenhaus, J. L.; Nasrabadi, H., Confinement-induced supercriticality and phase equilibria of hydrocarbons in nanopores. *Langmuir* 2016, 32, 11506-11513.
17. Sandoval, D. R.; Yan, W.; Michelsen, M. L.; Stenby, E. H., Influence of Adsorption and Capillary Pressure on Phase Equilibria inside Shale Reservoirs. *Energy Fuels* 2018, 32, 2819-2833.
18. Nojabaei, B.; Johns, R. T.; Chu, L., Effect of Capillary Pressure on Phase Behavior in Tight Rocks and Shales. *SPE Reservoir Eval. Eng.* 2013, 16, 281-289.
19. Dong, X.; Liu, H.; Hou, J.; Wu, K.; Chen, Z., Phase Equilibria of Confined Fluids in Nanopores of Tight and Shale Rocks Considering the Effect of Capillary Pressure and Adsorption Film. *Ind. Eng. Chem. Res.* 2016, 55, 798-811.
20. Luo, S.; Nasrabadi, H.; Lutkenhaus Jodie, L., Effect of confinement on the bubble points of hydrocarbons in nanoporous media. *AIChE J.* 2016, 62, 1772-1780.
21. Jin, Z.; Firoozabadi, A., Thermodynamic Modeling of Phase Behavior in Shale Media. *SPE J.* 2016, 21, 190-207.
22. Posocco, P.; Gentilini, C.; Bidoggia, S.; Pace, A.; Franchi, P.; Lucarini, M.; Fermeglia, M.; Priol, S.; Pasquato, L., Self-organization of mixtures of fluorocarbon and hydrocarbon amphiphilic thiolates on the surface of gold nanoparticles. *ACS Nano* 2012, 6, 7243-7253.
23. Phan, A.; Cole, D. R.; Weiß, R. G.; Dzubiella, J.; Striolo, A., Confined water determines transport properties of guest molecules in narrow pores. *ACS Nano* 2016, 10, 7646-7656.
24. Chiavazzo, E.; Fasano, M.; Asinari, P.; Decuzzi, P., Scaling behaviour for the water transport in nanoconfined geometries. *Nat. Commun.* 2014, 5, 3565.
25. Mameka, N.; Markmann, J.; Weissmüller, J., On the impact of capillarity for strength at the nanoscale. *Nat. Commun.* 2017, 8, 1976.
26. Fasano, M.; Humplik, T.; Bevilacqua, A.; Tsapatsis, M.; Chiavazzo, E.; Wang, E. N.; Asinari, P., Interplay between hydrophilicity and surface barriers on water transport in zeolite membranes. *Nat. Commun.* 2016, 7, 12762.
27. Yoon, D.; Lee, C.; Yun, J.; Jeon, W.; Cha, B. J.; Baik, S., Enhanced condensation, agglomeration, and rejection of water vapor by superhydrophobic aligned multiwalled carbon nanotube membranes. *ACS Nano* 2012, 6, 5980-5987.
28. Xiao, K.; Zhou, Y.; Kong, X.-Y.; Xie, G.; Li, P.; Zhang, Z.; Wen, L.; Jiang, L., Electrostatic-charge-and electric-field-induced smart gating for water transportation. *ACS Nano* 2016, 10, 9703-9709.
29. Barsotti, E.; Tan, S. P.; Saraji, S.; Piri, M.; Chen, J.-H., A review on capillary condensation in nanoporous media: Implications for hydrocarbon recovery from tight reservoirs. *Fuel* 2016, 184, 344-361.
30. Cho, H.; Bartl, M. H.; Deo, M., Bubble Point Measurements of Hydrocarbon Mixtures in Mesoporous Media. *Energy Fuels* 2017, 31, 3436-3444.
31. Pathak, M.; Kweon, H.; Deo, M.; Huang, H., Kerogen Swelling and Confinement: Its Implication on Fluid Thermodynamic Properties in Shales. *Sci. Rep.* 2017, 7, 12530.
32. Luo, S.; Lutkenhaus, J. L.; Nasrabadi, H., Use of differential scanning calorimetry to study phase behavior of hydrocarbon mixtures in nano-scale porous media. *Journal of Petroleum Science and Engineering* 2016, 163, 731-738.
33. Kohonen, M. M.; Christenson, H. K., Capillary condensation from vapors of n-hexane/perfluoro-n-hexane mixtures. *J. Phys. Chem. B* 2002, 106, 6685-6695.
34. Perry, J. M.; Zhou, K.; Harms, Z. D.; Jacobson, S. C., Ion transport in nanofluidic funnels. *ACS Nano* 2010, 4, 3897-3902.
35. Kim, B.; Heo, J.; Kwon, H. J.; Cho, S. J.; Han, J.; Kim, S. J.; Lim, G., Tunable ionic transport for a triangular nanochannel in a polymeric nanofluidic system. *ACS Nano* 2012, 7, 740-747.
36. Li, H.; Zhong, J.; Pang, Y.; Zandavi, S. H.; Persad, A. H.; Xu, Y.; Mostowfi, F.; Sinton, D., Direct visualization of fluid dynamics in sub-10 nm nanochannels. *Nanoscale* 2017, 9, 9556-9561.
37. Zhong, J.; Talebi, S.; Xu, Y.; Pang, Y.; Mostowfi, F.; Sinton, D., Fluorescence in sub-10 nm channels with an optical enhancement layer. *Lab Chip* 2018, 18, 568-573.
38. Bao, B.; Zandavi, S. H.; Li, H.; Zhong, J.; Jatukaran, A.; Mostowfi, F.; Sinton, D., Bubble nucleation and growth in nanochannels. *Phys. Chem. Chem. Phys.* 2017, 19 (12), 8223-8229.
39. Zhong, J.; Riordon, J.; Zandavi, S. H.; Xu, Y.; Persad, A. H.; Mostowfi, F.; Sinton, D., Capillary Condensation in 8-nm Deep Channels. *J. Phys. Chem. Lett.* 2018, 9, 497-503.
40. Jatukaran, A.; Zhong, J.; Persad, A. H.; Xu, Y.; Mostowfi, F.; Sinton, D., Direct Visualization of Evaporation in a Two-Dimensional Nanoporous Model for Unconventional Natural Gas. *ACS Appl. Nano Mater.* 2018, 1, 1332-1338.

- 41.Xie, Q.; Alibakhshi, M. A.; Jiao, S.; Xu, Z.; Hempel, M.; Kong, J.; Park, H. G.; Duan, C., Fast water transport in graphene nanofluidic channels. *Nat. Nanotechnol.* 2018, 13, 238-245.
- 42.Zhong, J.; Zandavi, S. H.; Li, H.; Bao, B.; Persad, A. H.; Mostowfi, F.; Sinton, D., Condensation in One-Dimensional Dead-End Nanochannels. *ACS Nano* 2017, 11, 304-313.
- 43.Xu, L.; Abedini, A.; Qi, Z.; Kim, M.; Guerrero, A.; Sinton, D., Pore-scale analysis of steam-solvent coinjection: azeotropic temperature, dilution and asphaltene deposition. *Fuel* 2018, 220, 151-158.
- 44.Song, W.; Kovsky, A. R., Functionalization of micromodels with kaolinite for investigation of low salinity oil-recovery processes. *Lab Chip* 2015, 15, 3314-3325.

## Component 5: Single component hydrocarbon evaporation in 2-D sub-10 nm nanogrids

Evaporation and vapour transport in two-dimensional (2D) nanoporous media plays an important role in many natural processes and synthetic systems such in biological membranes<sup>1</sup>, plant hydrodynamics<sup>2,3</sup>, electronic cooling devices<sup>4</sup>, steam generation<sup>5-8</sup>, water desalination strategies<sup>9</sup> and the recovery of hydrocarbons from unconventional oil and gas reservoirs<sup>10-13</sup>. There is particular urgency regarding the latter. These reservoirs are typically characterized by pores that can be smaller than 10 nm<sup>14</sup>. Experimental techniques to study the onset and dynamics of evaporation in porous media at such length scales are urgently required to validate the applicability of classical theories, improve the efficiency of production, and inform policy makers and the public.

Recent advances in nanofluidics promote studying phase change at the nanoscale. Liquid to vapour transitions such as evaporation<sup>15-19</sup> and cavitation<sup>20-22</sup>, in particular, have garnered significant attention. Despite this growth, experimental techniques to study evaporation at the nanoscale are hindered by both the challenge of fabricating precise 2D nanoscopic conduits and the difficulty in directly visualizing vapour and liquid phases in extreme nanoconfinement (<10 nm). As such, literature on the direct visualization of liquid to vapour transitions is limited to studies in idealized one-dimensional nanochannels where the smallest critical nanoscale dimension reported has been 20 nm<sup>20</sup>.

In this component, we directly visualize the liquid evaporation in a well-controlled 2D sub-10 nm nanoporous media (composing of a network of nanopores fabricated on nanofluidic device with a height of 9 nm and a width of ~200 nm) using propane as a working fluid. A silicon nitride layer below the nanopores forms a Fabry-Perot optical resonance cavity to enhance the contrast between liquid and vapour phases<sup>23</sup>. The onset of evaporation in the 2D nanoporous media is measured at a wide range of temperature and pressure conditions, showing significant deviation comparing to the classical Kelvin equation predictions. Evaporation dynamics are directly detected at sub-10 nm scale for the first time, and is found to be chiefly governed by the vapor transport resistance in the nanopores, deviating strongly from the classical Hertz-Knudsen equation predictions. We also observe the initial liquid-phase saturation conditions can lead to different types of evaporation mechanisms (continuous evaporation and discontinuous evaporation with isolated cavitation), as a unique phenomenon for sub-10 nm system. In providing a clear picture of evaporation in the sub-10 nm nanoporous media, this work demonstrates the breakdown of classical theories for evaporation at sub-10 nm confinement.

1. O. Beckstein and M. S. P. Sansom, "Liquid – vapor oscillations of water in hydrophobic nanopores," *Proc. Natl. Acad. Sci. U. S. A.*, vol. 100, pp. 7063–7068, 2003.

2. T. D. Wheeler and A. D. Stroock, "The transpiration of water at negative pressures in a synthetic tree," *Nature*, vol. 455, no. September, pp. 208–212, 2008.

3. J. Comtet, K. H. Jensen, R. Turgeon, A. D. Stroock, and A. E. Hosoi, "Passive phloem loading and long-distance transport in a synthetic tree-on-a-chip," *Nat. Plants*, vol. 3, p. 17032, 2017.
4. A. Alabastri, M. Malerba, E. Calandrini, A. Manjavacas, F. De Angelis, A. Toma, and R. P. Zaccaria, "Controlling the Heat Dissipation in Temperature-Matched Plasmonic Nanostructures," *Nano Lett.*, 2017.
5. H. Ghasemi, G. Ni, A. M. Marconnet, J. Loomis, S. Yerci, N. Miljkovic, and G. Chen, "Solar steam generation by heat localization," *Nat. Commun.*, vol. 5, pp. 1–7, 2014.
6. J. Yang, Y. Pang, W. Huang, S. K. Shaw, J. Schi, M. A. Pillers, X. Mu, S. Luo, T. Zhang, Y. Huang, G. Li, S. Ptasinska, M. Lieberman, and T. Luo, "Functionalized Graphene Enables Highly Efficient Solar Thermal Steam Generation," *ACS Nano*, vol. 11, pp. 5510–5518, 2017.
7. Z. Fang, Y.-R. Zhen, O. Neumann, A. Polman, F. J. G. de Abajo, P. Nordlander, and N. J. Halas, "Evolution of Light-Induced Vapor Generation at a Liquid-Immersed Metallic Nanoparticle," *Nano Lett.*, vol. 13, pp. 1736–1742, 2013.
8. M. S. Zielinski, J. Choi, T. La Grange, M. Modestino, S. Mohammad, H. Hashemi, Y. Pu, S. Birkhold, A. Hubbell, and D. Psaltis, "Hollow Mesoporous Plasmonic Nanoshells for Enhanced Solar Vapor Generation," *Nano Lett.*, vol. 16, pp. 2159–2167, 2016.
9. L. Zhou, Y. Tan, J. Wang, W. Xu, Y. Yuan, W. Cai, S. Zhu, and J. Zhu, "3D self-assembly of aluminium nanoparticles for plasmon-enhanced solar desalination," *Nat. Photonics*, vol. 10, pp. 393–398, 2016.
10. P. J. M. Monteiro, C. H. Rycroft, and G. I. Barenblatt, "A mathematical model of fluid and gas flow in nanoporous media," *Proc. Natl. Acad. Sci. U. S. A.*, vol. 110, pp. 20309–20313, 2013.
11. L. Cueto-felgueroso and R. Juanes, "Forecasting long-term gas production from shale," *Proc. Natl. Acad. Sci. U. S. A.*, vol. 110, pp. 19660–19661, 2013.
12. J. Zhong, S. H. Zandavi, H. Li, B. Bao, A. H. Persad, F. Mostowfi, and D. Sinton, "Condensation in One-Dimensional Dead-End Nanochannels," *ACS Nano*, vol. 11, pp. 304–313, 2016.
13. B. Bao, J. Riordon, D. Sinton, and B. Bao, "Lab on a Chip characterization for industrial CO<sub>2</sub>, oil and gas," *Lab Chip*, vol. 17, pp. 2740–2759, 2017.
14. H. E. King, A. P. R. Eberle, C. Walters, C. E. Kliewer, D. Ertas, and C. Huynh, "Pore Architecture and Connectivity in Gas Shale," *Energy & Fuels*, vol. 29, pp. 1375–1390, 2015.
15. O. Vincent, A. Szenicer, and A. D. Stroock, "Capillarity-driven flows at the continuum limit," *Soft Matter*, vol. 12, pp. 6656–6661, 2016.
16. Y. Li, M. A. Alibakhshi, Y. Zhao, and C. Duan, "Exploring Ultimate Water Capillary Evaporation in Nanoscale Conduits," *Nano Lett.*, 2017.
17. Q. Xie, S. Xiao, and C. Duan, "Geometric Dependent Drying in Dead-End Nanochannels," *Langmuir*, 2017.
18. V.-N. Phan, N.-T. Nguyen, C. Yang, P. Joseph, and A.-M. Gue, "Fabrication and Experimental Characterization of Nanochannels," *J. Heat Transfer*, vol. 134, p. 51012, 2012.
19. J. C. T. Eijkel, B. Dan, H. W. Reemeijer, D. C. Hermes, J. G. Bomer, and A. Van Den Berg, "Strongly Accelerated and Humidity-Independent Drying of Nanochannels Induced by Sharp Corners," *Phys. Rev. Lett.*, vol. 95, p. 256107, 2005.
20. C. Duan, R. Karnik, M. Lu, and A. Majumdar, "Evaporation-induced cavitation in nanofluidic channels," *Proc. Natl. Acad. Sci. U. S. A.*, vol. 109, no. 10, pp. 3688–3693, 2012.
21. B. Bao, S. H. Zandavi, H. Li, J. Zhong, A. Jatukaran, F. Mostowfi, and D. Sinton, "Bubble nucleation and growth in nanochannels," *Phys. Chem. Chem. Phys.*, vol. 19, pp. 8223–8229, 2017.
22. O. Vincent, D. A. Sessoms, E. J. Huber, J. Guioth, and A. D. Stroock, "Drying by Cavitation and Poroelastic Relaxations in Porous Media with Macroscopic Pores Connected by Nanoscale Throats," *Phys. Rev. Lett.*, vol. 113, no. SEPTEMBER, pp. 1–5, 2014.
23. H. Li, J. Zhong, Y. Pang, S. H. Zandavi, A. H. Persad, Y. Xu, and D. Sinton, "Direct visualization of fluid dynamics in sub-10 nm nanochannels," vol. 9, pp. 9556–9561, 2017.

## Component 6: 2-D nanogrids in screening enhanced tight oil recovery strategies

The massive scale of unconventional oil and gas recovery results in impacts on CO<sub>2</sub> that are globally significant and diverse. For instance, increased production of shale gas has led to a reduction in more carbon intensive coal-based electricity production, with significant climate benefit. Natural gas emits 45% CO<sub>2</sub> of coal from generating the same amount of electrical energy<sup>3</sup>, and is thus regarded as a bridge energy to future carbon-free energy by slowing the rising global warming trend. At the same time, the sheer volume of shale resources – including both natural gas and oil – represents a massive CO<sub>2</sub> source and associated climate threat. Extensive water and pumping energy use in hydraulic fracturing, as well as methane leakage of abandoned wells are additional environmental concerns<sup>4-5</sup>, particularly as the current energy return is well below potential. For these reasons, the field is in search of enhanced oil recovery (EOR) strategies. One

of particular interest is CO<sub>2</sub> injection, which can in principle achieve a combination of more efficient resource recovery while sequestering CO<sub>2</sub>. This process is well-established in conventional oil and gas operations, and constitutes the single largest global industrial use of CO<sub>2</sub> which would otherwise be a greenhouse gas emission<sup>6</sup>. Compared to conventional reservoirs, however, shale reservoirs typically have nanometer pores (< 100 nm), low porosity (~10%) and low permeability (nano Darcy to micro Darcy)<sup>7-8</sup>, which significantly limits well productivity<sup>9-10</sup>. Assessing existing EOR strategies, as well as developing new ones for unconventional reservoirs is thus of both academic and commercial interest.

Numerical simulations<sup>11-13</sup>, core flood tests<sup>14-15</sup> and field pilot tests<sup>16</sup> are currently the primary means in studying EOR strategies in unconventional reservoirs. Although they have provided some insights into tight oil EOR, there are limitations for these approaches. For the numerical simulation, a fundamental challenge is the applicability of classical fluid mechanics and thermodynamics at relevant nanoscales<sup>17</sup> – a criticism that can only be addressed with experimental validation. In conventional core testing, the resolution of the experimental results is limited by the opacity of the system. The extremely small pore sizes exacerbate this deficiency. A full field pilot is the ultimate test of an EOR strategy, but this option is very expensive and slow, with effectively low resolution and the influence of the strategy under test can be confounded by external factors within the reservoir. Field pilots should be reserved as final validations for strategies optimized through rapid iteration with informative, high resolution, controlled tests. Recent progress in micro/nanofluidics has allowed accurate fluid analysis down to a few nanometers, such as hydrocarbon phase behavior measurements<sup>18-20</sup> and liquid transport<sup>21-23</sup>. While these works provide fundamental insights into the primary production in shale reservoirs, such methods have not been applied to the critical challenge of assessing EOR strategies in unconventional oil recovery – a system with complex fluid mixture transport and interactions under nanoconfinement.

In this component, we propose a nanofluidic approach targeting rapid screening of EOR strategies for unconventional tight oil recovery. A nanomodel with 10<sup>6</sup> 2-D nanoarrays are fabricated, defining a nanoporous system with a pore size of 60 nm (close to the major pore size in a majority of unconventional oil formations<sup>24</sup>), while matching the low porosity (here ~14%) and permeability (here ~ 10 μD) of shale. The nanomodel allows direct in-situ observation of nanopore-scale complex fluid behaviors, enabling rapid evaluation of EOR mechanisms and strategies rapidly, (a few hours) compared to core (days) or field tests (months). We demonstrate application to screen the most promising EOR strategies in shale reservoirs: gas flooding (N<sub>2</sub> and CO<sub>2</sub>), and huff-and-puff (CO<sub>2</sub>). We assess the feasibility of these strategies previously established in microporous conventional reservoirs, in tight oil and shale relevant nanoconfinement, and quantify performance as a function of parameters relevant to field operations. Importantly, we find a significant initiation pressure threshold for immiscible gas flooding that is unique to operations at this scale. Miscible gas flooding can reduce the threshold, and improve the recovery efficiency. In the huff-and-puff processes, the initial injection gas pressure strongly affects the final recovery efficiency via both gas solubility and miscibility. A sufficient gas pressure drawdown rate during the recovery stage is also essential to limit gas diffusion and generate recovery via gas breakout. The developed nanomodel is a powerful platform for probing and screening emerging unconventional reservoir-technologies. More generally, it can also be applied in addressing issues within other emerging energy and environmental topics, such as fuel cell<sup>25</sup> and crude-oil-repellent membranes<sup>26</sup>.

1. Hughes, J. D., Energy: A reality check on the shale revolution. *Nature* 2013, 494, 307.
2. Conti, J. J.; Holtberg, P. D.; Beamon, J.; Schaal, A. M.; Ayoub, J.; Turnure, J. T., Annual energy outlook 2018. US Energy Information Administration 2018.
3. Kerr, R. A., Natural gas from shale bursts onto the scene. *Science* 2010, 328, 1624-1626.
4. Howarth, R. W.; Ingraffea, A.; Engelder, T., Natural gas: Should fracking stop? *Nature* 2011, 477, 271-275.
5. Vidic, R. D.; Brantley, S. L.; Vandenbossche, J. M.; Yoxtheimer, D.; Abad, J. D., Impact of shale gas development on regional water quality. *Science* 2013, 340, 1235009.
6. Lackner, K. S., A guide to CO<sub>2</sub> sequestration. *Science* 2003, 300, 1677-1678.
7. Burnham, A. K., Porosity and permeability of Green River oil shale and their changes during retorting. *Fuel* 2017, 203, 208-213.
8. Sayed, M. A.; Al-Muntasheri, G. A.; Liang, F., Development of shale reservoirs: Knowledge gained from developments in North America. *J. Pet. Sci. Technol.* 2017, 157, 164-186.
9. Zhao, J.; Jin, Z.; Hu, Q.; Jin, Z.; Barber, T. J.; Zhang, Y.; Bleuel, M., Integrating SANS and fluid-invasion methods to characterize pore structure of typical American shale oil reservoirs. *Sci. Rep.* 2017, 7, 15413.
10. Liu, K.; Ostadhassan, M.; Zhou, J.; Gentzis, T.; Rezaee, R., Nanoscale pore structure characterization of the Bakken shale in the USA. *Fuel* 2017, 209, 567-578.
11. Alfarge, D.; Wei, M.; Bai, B., Factors Affecting CO<sub>2</sub>-EOR in Shale-Oil Reservoirs: Numerical Simulation Study and Pilot Tests. *Energy Fuels* 2017, 31, 8462-8480.
12. Lai, F.; Li, Z.; Fu, Y.; Yang, Z.; Li, H., A simulation research on evaluation of development in shale oil reservoirs by near-miscible CO<sub>2</sub> flooding. *J. Geophys. Eng.* 2015, 12, 702.
13. Phan, A.; Cole, D. R.; Weiß, R. G.; Dziubiella, J.; Striolo, A., Confined water determines transport properties of guest molecules in narrow pores. *ACS Nano* 2016, 10, 7646-7656.
14. Li, L.; Zhang, Y.; Sheng, J. J., Effect of the Injection Pressure on Enhancing Oil Recovery in Shale Cores during the CO<sub>2</sub> Huff-n-Puff Process When It Is above and below the Minimum Miscibility Pressure. *Energy Fuels* 2017, 31, 3856-3867.
15. Abedini, A.; Torabi, F.; Mosavat, N., Performance of immiscible and miscible CO<sub>2</sub> injection process in a tight carbonate reservoir (experimental and simulation approach). *Int. J. Oil Gas Coal Technol.* 2015, 9, 265-279.
16. Sheng, J. J., Enhanced oil recovery in shale reservoirs by gas injection. *J. Nat. Gas Sci. Eng.* 2015, 22, 252-259.
17. Jin, Z., Bubble/dew point and hysteresis of hydrocarbons in nanopores from molecular perspective. *Fluid Phase Equilib.* 2018, 458, 177-185.
18. Zhong, J.; Riordon, J.; Zandavi, S. H.; Xu, Y.; Persad, A. H.; Mostowfi, F.; Sinton, D., Capillary Condensation in 8-nm Deep Channels. *J. Phys. Chem. Lett.* 2018, 9, 497-503.
19. Jatukaran, A.; Zhong, J.; Persad, A. H.; Xu, Y.; Mostowfi, F.; Sinton, D., Direct Visualization of Evaporation in a Two-Dimensional Nanoporous Model for Unconventional Natural Gas. *ACS Appl. Nano Mater.* 2018, 1, 1332-1338.
20. Zhong, J.; Zandavi, S. H.; Li, H.; Bao, B.; Persad, A. H.; Mostowfi, F.; Sinton, D., Condensation in One-Dimensional Dead-End Nanochannels. *ACS Nano* 2017, 11, 304-313.
21. Xie, Q.; Alibakhshi, M. A.; Jiao, S.; Xu, Z.; Hempel, M.; Kong, J.; Park, H. G.; Duan, C., Fast water transport in graphene nanofluidic channels. *Nature nanotechnology* 2018, 13, 238-245.
22. Kelly, S. A.; Torres-Verdín, C.; Balhoff, M. T., Subsurface to substrate: dual-scale micro/nanofluidic networks for investigating transport anomalies in tight porous media. *Lab Chip* 2016, 16, 2829-2839.
23. Liu, S.; Ma, Y.; Bai, B., Flow patterns of oil-water two-phase flow during pressure-driven process in nanoscale fluidic chips. *Microfluid. Nanofluid.* 2018, 22, 39-50.
24. Nelson, P. H., Pore-throat sizes in sandstones, tight sandstones, and shales. *AAPG Bull.* 2009, 93, 329-340.
25. Alrwashdeh, S. S.; Manke, I.; Markötter, H.; Klages, M.; Göbel, M.; Haußmann, J.; Scholta, J.; Banhart, J., In Operando Quantification of Three-Dimensional Water Distribution in Nanoporous Carbon-Based Layers in Polymer Electrolyte Membrane Fuel Cells. *ACS Nano* 2017, 11, 5944-5949.
26. Zhang, S.; Jiang, G.; Gao, S.; Jin, H.; Zhu, Y.; Zhang, F.; Jin, J., Cupric Phosphate Nanosheets-Wrapped Inorganic Membranes with Superhydrophilic and Outstanding Anticrude Oil-Fouling Property for Oil/Water Separation. *ACS Nano* 2018, 12, 795-803.

## Component 7: 2-D nanogrids in simulating shale gas primary recovery

Transport and thermodynamics of fluid mixtures in nanoporous media with a complex distribution of length scales is critical to a number of fields including biology<sup>1,2</sup> and geology.<sup>3,4</sup> In particular, the importance of the latter is highlighted by the rapid emergence of unconventional shale gas, now a mainstay of North American energy.<sup>5,6,7</sup> The well productivity is initially high due to rapid depletion of reservoir pressure and production from fractures and larger pores (order of meters to microns), and then declines as production shifts to the nanoporous matrix.<sup>3</sup> This relatively new process has had profound impacts in global energy and the environment. Examples of the widely varied impacts include a transition away from coal to less carbon-intensive natural gas in electricity production,<sup>8</sup> establishing US as a major global oil producer,<sup>9,10</sup> depressing global oil and gas prices,

and far-reaching environmental impacts from both the development of these resources (e.g., water use, energy use, CO<sub>2</sub> emissions, seismic activity) and the ultimate use of the produced natural gas.<sup>9–11</sup> While the broad implications of hydraulic fracturing technology are becoming clearer, there is a lack of fundamental understanding of this complex process. Understanding the complex fluid transport and thermodynamics at the heart of this process is essential for predicting production, environmental impacts and ultimately energy security.

The fundamental complexity of shale gas production at the heart of this process is a “dual-mixture” problem, i.e., the thermodynamics of a multi-component fluid mixture, in a media with a mixture of lengthscales. Pore size distributions of shale reservoirs present an interesting dichotomy wherein small pores ( $\leq 10$  nm) dominate in terms of their number and larger pores ( $\sim 100$  nm) dominate in terms of volume<sup>12,13</sup> and store most of the accessible hydrocarbons.<sup>14</sup> During recovery, bubble nucleation and evaporation is likely to be favoured in the larger pores,<sup>1</sup> however, the subsequent transport of fluids in the nanoporous matrix is limited by smaller conduits where nanoconfinement effects such as Knudsen diffusion become significant.<sup>15,16</sup> Further complicating the process is the multicomponent nature of the fluid in these pores, and changes in the composition of liquid and gas phases as production proceeds. Lighter, volatile components vaporize first, enriching the remaining liquid with heavier fractions.<sup>17</sup> Experimental tools are urgently needed to resolve these highly coupled complexities.

While micromodels have become an integral tool for visualizing pore scale mechanisms associated with oil sands and conventional reservoirs,<sup>18–21</sup> physical models with nanoscopic features representing shale gas, or nanomodels, are still in their infancy.<sup>22,23</sup> Advances in nanofabrication have enabled the direct study of nanoconfinement effects at a single length scale in discrete nanochannels,<sup>24</sup> differentiating fluid phases in sub-10 nm deep channels using simple single-component working fluids such as propane<sup>25</sup> and butane.<sup>26</sup> Introducing a model fluid mixture, we recently studied dew point and bubble point in straight 8, 80 and 800-nm channels, finding significant deviation from bulk theory in the smallest channels.<sup>17</sup> In the first work of its kind, Vincent et al. developed a system with 625 discrete micropores connected only via a nanoporous substrate to study drying dynamics of pure water. In this extreme ink-bottle geometry they found evaporation to be governed by stochastic nucleation and poroelastic mass transport, with local evaporation in large pores influencing surrounding pores.<sup>2</sup> While these contributions have provided some insight into the fundamentals of fluid behavior in nanoconfinement, idealized pore-geometries and pure fluid systems do not sufficiently capture the dual-mixture complexity inherent to shale reservoirs.

In this component we develop a nanoscale throat connected physical model of shale that incorporates the dominant pore sizes, with 100-nm large pores connected only through a 5-nm throat network. The model is loaded with a ternary hydrocarbon mixture (methane, propane and pentane) typical of liquid-rich natural gas. Dynamics of vaporization and production of natural gas are recorded by imaging the large pores over time. An analytical model is developed for evaporation in serially-connected 5-nm throats and 100-nm pores. Both the physical and analytical model show the impact of the mixed geometry, and experiments with lower vaporization driving force (lower temperature, higher pressure) resolve the additional influence of mixture dynamics in multiscale pores.

2. O. Vincent, D. A. Sessoms, E. J. Huber, J. Guioth and A. D. Stroock, *Phys. Rev. Lett.*, 2014, 113, 1–5.
3. J. D. Hyman, H. S. Viswanathan, J. W. Carey, M. L. Porter, E. Rougier, S. Karra, Q. Kang, L. Frash, L. Chen, Z. Lei, D. O. Malley and N. Makedonska, *Philos. Trans. A*, 2016, 374, 20150426.
4. P. J. M. Monteiro, C. H. Rycroft and G. I. Barenblatt, *Proc. Natl. Acad. Sci. U. S. A.*, 2012, 109, 20309–20313.
5. T. W. Patzek, F. Male and M. Marder, *Proc. Natl. Acad. Sci. U. S. A.*, , DOI:10.1073/pnas.1313380110.
6. U.S. Energy Information Administration, *Electricity Explained: Electricity in the United States*, [https://www.eia.gov/energyexplained/index.php?page=electricity\\_in\\_the\\_united\\_states](https://www.eia.gov/energyexplained/index.php?page=electricity_in_the_united_states), (accessed 23 September 2018).
7. U.S. Energy Information Administration, *FREQUENTLY ASKED QUESTIONS: How much shale gas is produced in the United States?*, <https://www.eia.gov/tools/faqs/faq.php?id=907&t=8>, (accessed 23 September 2018).
8. L. M. Cathles, *Geochemistry Geophys. Geosystems*, 2012, 13, Q06013.
9. Q. Wang, X. Chen, A. N. Jha and H. Rogers, *Renew. Sustain. Energy Rev.*, 2014, 30, 1–28.
10. R. A. Alvarez, S. W. Pacala, J. J. Winebrake, W. L. Chameides and S. P. Hamburg, *Proc. Natl. Acad. Sci. U. S. A.*, 2012, 109, 6435–6440.
11. M. Melikoglu, *Renew. Sustain. Energy Rev.*, 2014, 37, 460–468.
12. M. E. Curtis, C. H. Sondergeld, R. J. Ambrose and C. S. Rai, *Am. Assoc. Pet. Geol. Bull.*, 2012, 4, 665–677.
13. A. A. Hasham, A. Abedini, A. Jatukaran, A. Persad and D. Sinton, *J. Pet. Sci. Eng.*, 2018, 165, 181–186.
14. J. Zhao, Z. Jin and H. Qinrong, *Sci. Rep.*, 2017, 7, 15413.
15. J. Zhong, S. H. Zandavi, H. Li, B. Bao, A. H. Persad, F. Mostowfi and D. Sinton, *ACS Nano*, 2016, 11, 304–313.
16. A. Jatukaran, J. Zhong, A. H. Persad, Y. Xu, F. Mostowfi and D. Sinton, *ACS Appl. Nano Mater.*, 2018, 1, 1332–1338.
17. J. Zhong, Y. Zhao, C. Lu, Y. Xu, Z. Jin, F. Mostowfi and D. Sinton, *Langmuir*, 2018, 34, 9927–9935.
18. T. W. de Haas, H. Fadaei, U. Guerrero and D. Sinton, *Lab Chip*, , DOI:10.1039/c3lc50612f.
19. A. Anbari, H. Chien, S. S. Datta, W. Deng and D. A. Weitz, *Small*, 2018, 1703575, 1–15.
20. B. Zhao, C. W. Macminn and R. Juanes, *Proc. Natl. Acad. Sci. U. S. A.*, 2016, 113, 10251–10256.
21. K. Xu, T. Liang, P. Zhu, P. Qi, J. Lu, C. Huh and M. Balhoff, *Lab Chip*, 2017, 17, 640–646.
22. M. L. Porter, J. Jiménez-martínez, R. Martínez, Q. McCulloch, J. William and H. S. Viswanathan, *Lab Chip*, 2015, 15, 4044–4053.
23. S. A. Kelly, C. Torres-Verdín and M. T. Balhoff, *Lab Chip*, 2016, 16, 2829–2839.
24. J. Zhong, S. Talebi, Y. Pang, F. Mostowfi and D. Sinton, *Lab Chip*, 2018, 18, 568–573.
25. J. Zhong, J. Riordon, S. H. Zandavi, Y. Xu, A. H. Persad, F. Mostow and D. Sinton, *J. Phys. Chem. Lett.*, 2018, 9, 497–503.
26. Q. Yang, B. Jin, D. Banerjee and H. Nasrabadi, *Fuel*, 2019, 235, 1216–1223.

### Key Alberta Innovates points:

- Hydrocarbon phase behaviors in shale govern the recovery process.
- The shale challenge is multi-component fluid mixtures within radically multi-scale geometries.
- Experimental strategy in probing fluid behaviors at nanoscale is scarce.
- This Alberta Innovates project provided the first geometrically relevant shale gas production model based on nanofluidic device;
- The nanofluidic tools and methods developed in this project aim to help Alberta's energy industry improve recovery process in terms of fundamental physical theories.

## 3.2 Technology development

### 3.2.1 Nanofluidic device fabrication

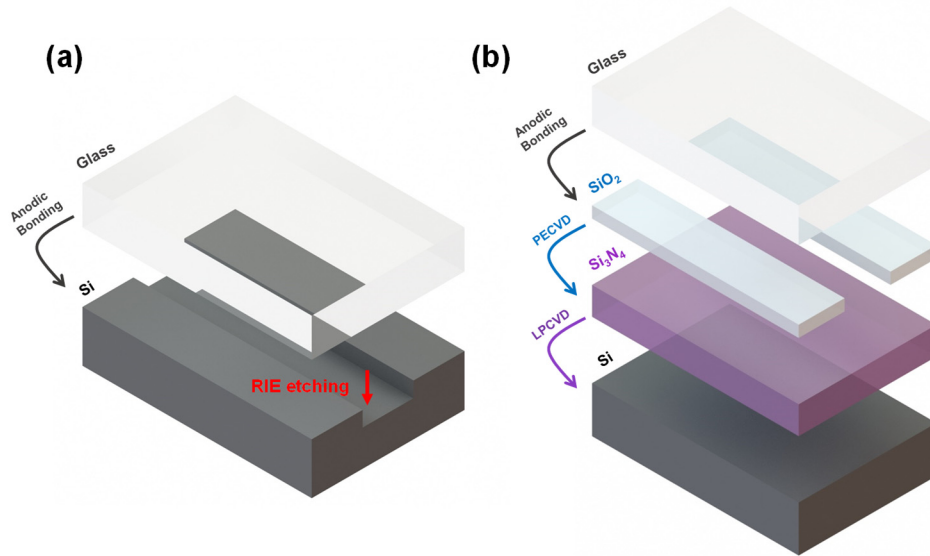


Figure 3 Schematic of fabrication procedure for silicon based nanofluidic device with (a) nanochannel/nanopore depth above 10 nm and (b) below 10 nm (sub-10 nm).

Depending on the nanofeature (nanopore or nanochannel) size required, the nanofluidic chip fabrication follows different procedures. When the nanofeature height is above 10 nm, especially above 50 nm, the nanochannel/nanopore is directly etched on the silicon surface using reactive ion etching (Figure 3, a) with an extreme low etching rate recipe (etching rate at 200 nm/min). In detail, the silicon wafer (1 mm thick, 4 inch) top surface is firstly spin-coated with the S1818 photoresist at 2000 rpm for 90 s (the coated S1818 thickness is  $\sim 2$   $\mu\text{m}$ ). A designed pattern is prepared through photomask (written by HEIDELBERG,  $\mu\text{PG501}$ , Figure 4, a), and transferred onto the photoresist on the silicon wafer through proper exposure (exposed through EVG 620, Figure 4, b). If the pattern with feature size less than 1  $\mu\text{m}$  in plane, it is generated through electron beam lithography instead (Vistec EBPG 5000+ Electron Beam Lithography System, Figure 4, c). After developing in a 50% MF312 aqueous solution (i.e., MF312 : water = 1 : 1, volumetric ratio) for 1 min, the silicon wafer with the designed pattern is etched through reactive ion etching (Oxford Instruments PlasmaPro Estrelas100 DRIE System, Figure 4, d) to reach designed channel depth. Necessary cleaning is conducted in Piranha solution ( $\text{H}_2\text{SO}_4$  :  $\text{H}_2\text{O}_2$  = 3 : 1) for 1 hour. Microchannels and through-holes are fabricated on the wafer afterwards for connecting nanofeatures to tubing and pumps. Lastly, the silicon wafer is anodically bonded with a 2.25 mm thick Borosilicate glass at 600 V and 673 K (through AML AWB-04 Aligner Wafer Bonder, Figure 4, e), and diced into desired shape (through Disco DAD3220 Automatic Dicing Saw, Figure 4, f). The nanofluidic chip fabricated with this procedure can confine fluid up to 20 MPa and 573 K.

Fabricating nanofeatures with depth below 10 nm (sub-10 nm) follows different procedures (Figure 3, b), as the previous procedure at this scale potentially leads to (i) etching inaccuracy and (ii) bonding collapse of nanofeatures, as well as (iii) invisibility of fluid phases confined within the nanochannel/nanopore under the optical microscope. To solve these issues, another nanofluidic fabrication procedure is designed uniquely for sub-10 nm nanofeatures.

The silicon wafer is firstly deposited with a silicon nitride layer through the low pressure chemical vapor deposition (Expertech CTR-200 LPCVD, Figure 4, g), and then a sub-10 nm thick (e.g., 8-nm, depending on required nanofeature depth) silicon dioxide layer through the plasma-enhanced chemical vapor deposition (Oxford Instruments PlasmaLab System 100 PECVD, Figure 4, h). The silicon nitride and dioxide layer thickness is monitored through ellipsometry (Horiba Jobin Yvon UVISEL Ellipsometer, Figure 4, i). Afterwards, the desired pattern is transferred to the silicon dioxide layer surface similar to the previous fabrication procedures. The nanofeature is etched through wet etching of the silicon dioxide (buffered oxide etch, BOE, 10:1), where the depth of nanofeature is defined by the thickness of the silicon dioxide layer due to a high selectivity of BOE between silicon dioxide and silicon nitride. After microchannels and holes being fabricated, the wafer is anodically bonded with a 2.25 mm thick Borosilicate glass at 100 V/673 K, and diced into the desired shape. Important features for this type of nanofluidic device include: (i) accurate control over nanofeature depth through the thickness of deposited silicon dioxide, (ii) avoiding nanochannel/nanopore bonding collapse through the silicon nitride layer sharing the bonding voltage and (iii) enhancing contrast between fluid phases for direct observation by creating a Fabry-Perot cavity. The nanofluidic chip fabricated with this procedure can confine fluid up to 5 MPa and 573 K. Detailed nanofluidic chip fabrication procedures are also discussed in each chapter for specific designs.

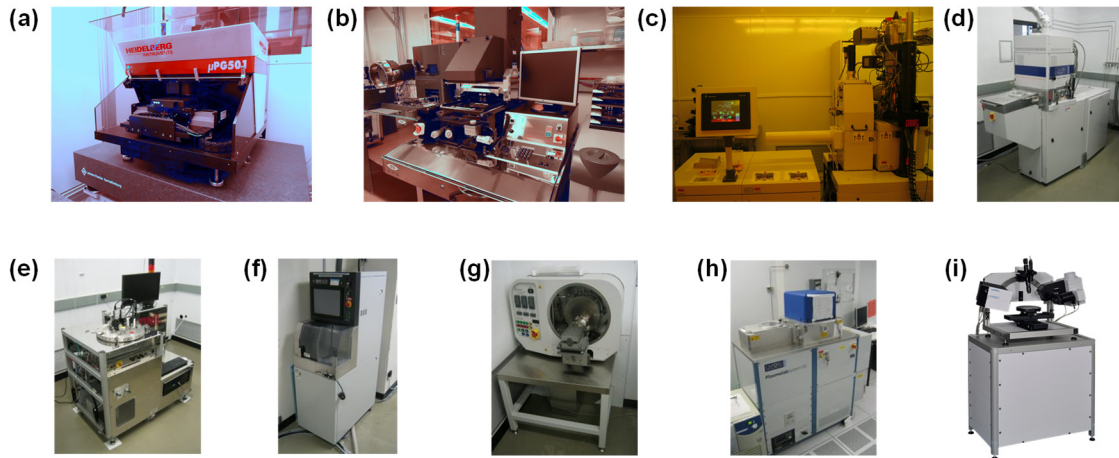


Figure 4 Devices for nanofluidic chip fabrication. (a) Photomask writing device, Heidelberg,  $\mu$ PG501. (b) Mask aligning and exposure device, EVG 620. (c) Electron beam lithography device, Vistec EBP5000+ Electron Beam Lithography System. (d) Reactive ion etching device, Oxford Instruments PlasmaPro Estrelas100 DRIE System. (e) Anodic bonding device, AML AWB-04 Aligner Wafer Bonder. (f) Chip dicing device, Disco DAD3220 Automatic Dicing Saw. (g) Low pressure chemical vapor deposition device, Expertech CTR-200 LPCVD. (h) Plasma-enhanced chemical vapor deposition, Oxford Instruments PlasmaLab System 100 PECVD. (i) Film thickness characterization device, Horiba Jobin Yvon UVISEL Ellipsometer.

To determine the contrast enhancement effect of silicon nitride layer at different layer thickness, the finite-difference time-domain (FDTD) simulation is firstly performed using a commercially available computational electromagnetic software package (Lumerical FDTD) based on the chip structure (Figure 5). Light reflectivity for gas, liquid and wall is calculated first at different visible light wavelength. The contrast between two phases is quantified by a ratio between the reflectivity

of two phases. For example, for a 8-nm deep nanochannel without any silicon nitride layer (Figure 5, a and b), the contrast between gas/wall, liquid/wall or gas/liquid is close to unity at any wavelength of visible light (380 nm to 780 nm). This result indicates that under the optical microscope (bright field), it is unable to distinguish solid wall, liquid and gas within the nanofluidic device, as is demonstrated in the inset of Figure 5, b directly observed under optical microscope. While by adding a silicon nitride layer (Figure 5, c and d), the contrast between, for example gas/liquid, can be enhanced to  $\sim 1.2$  at  $\sim 650$  nm wavelength, indicating the possibility in distinguishing gas and liquid under the optical microscope, as is also proven by the inset of Figure 5, d directly observed under microscope. Similarly, one can effectively distinguish liquid/wall and gas/wall as shown here.

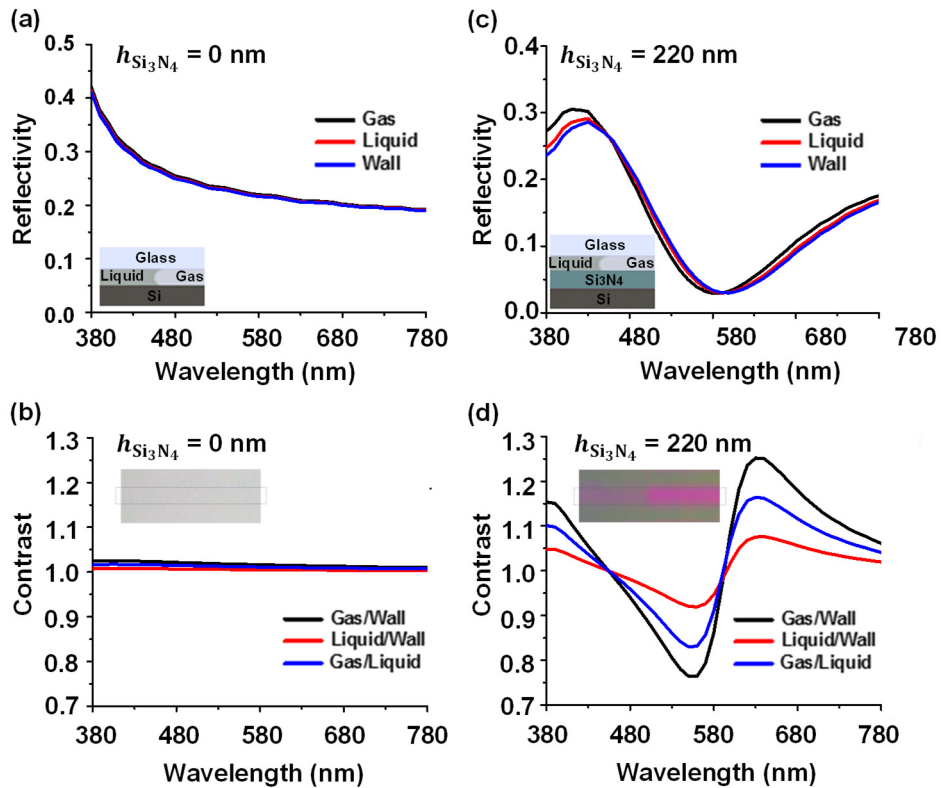


Figure 5 FDTD simulation results of reflectivity and contrast spectra for an 8-nm high channel without (a, b) and with (c, d) the Si<sub>3</sub>N<sub>4</sub> layer.

Different silicon nitride layer thicknesses are calculated for choosing the best performing silicon nitride layer thickness. As shown in Figure 6, when the silicon nitride layer is at 100 nm, 150 nm and 220 nm, the contrast curve between gas/liquid deviates significantly from unity, indicating contrast enhancement between gas and liquid phase confined within the nanochannel. When the layer thickness is increased to 400 nm, the deviation is negligible. As the light source for the bright field microscope includes a wide light spectrum, it is hard to quantitatively and accurately compare the overall enhancement effect directly through the simulation results. Instead, the simulation provides a range of silicon nitride layer thickness (here from 100 nm to 220 nm) that potentially enhances the contrast effectively by comparing the peak and valley of the contrast curve. Experiments on chip are further performed, with results shown in Figure 7. The 220-nm silicon

nitride layer thickness provides the best contrast between gas and liquid phases (1.33) confining in an 8-nm nanochannel, compared to other cases (1.23 for 100 nm, 1.20 for 150 nm and 1.14 for 400 nm).

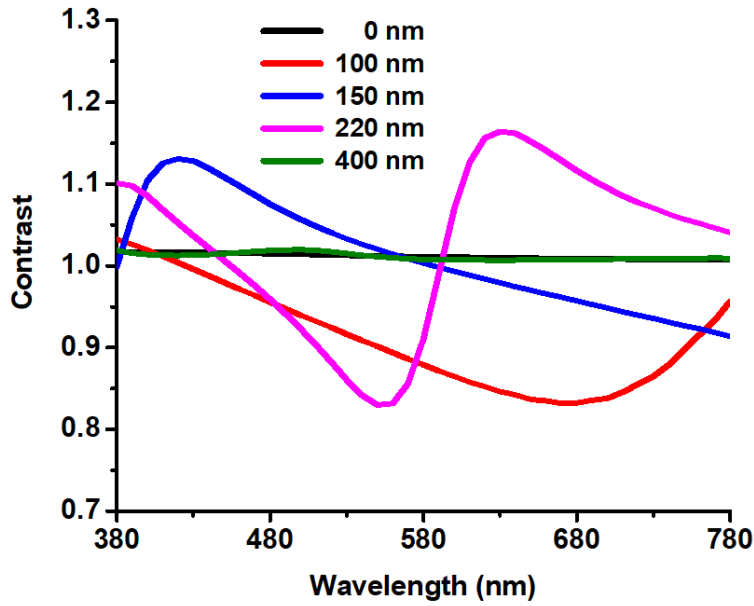


Figure 6 Dependence of gas/liquid contrast on the thickness of the Si<sub>3</sub>N<sub>4</sub> layer.

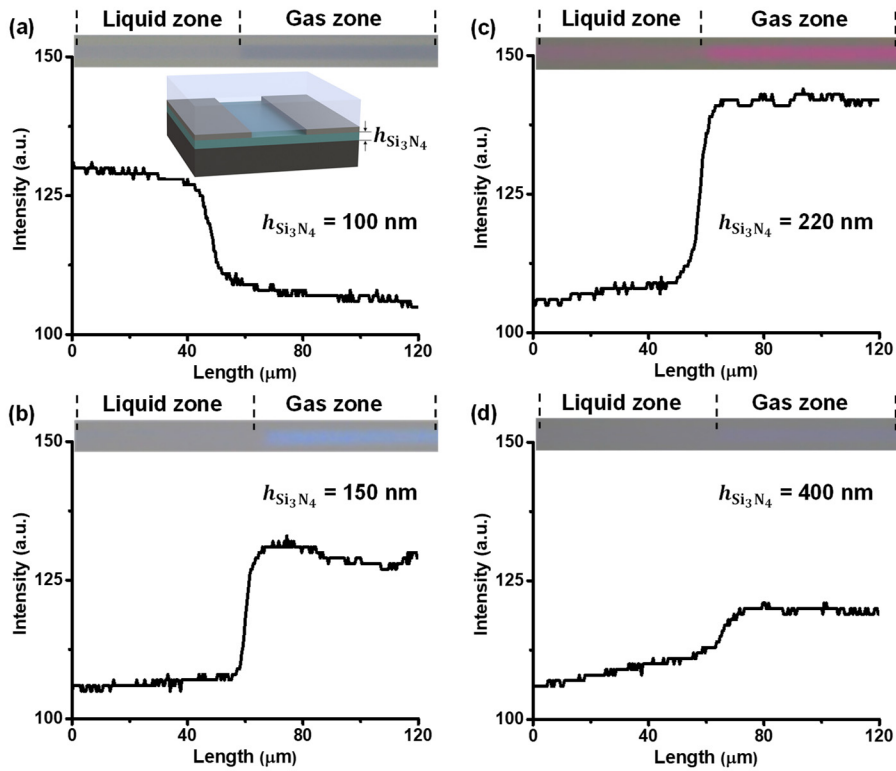


Figure 7 The role of Si<sub>3</sub>N<sub>4</sub> layer height,  $h_{\text{Si}_3\text{N}_4} = 100$  nm (a), 150 nm (b), 220 nm (c), and 400 nm (d) on liquid-gas contrast within 8-nm high channels. Each channel contains both a liquid and gas phases as indicated, with the accompanying contrast spectra.

### 3.2.2 Experimental setup

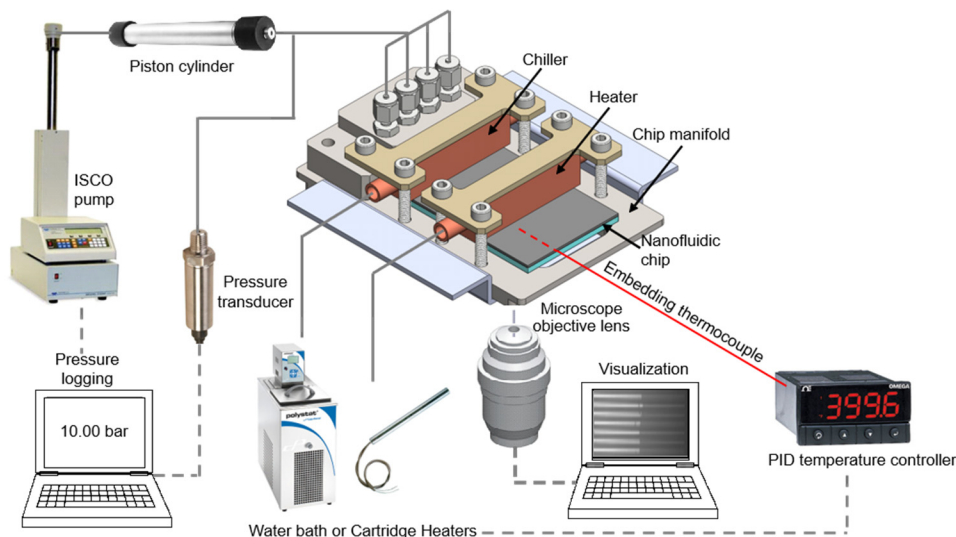


Figure 8 Schematic of the experimental setup connecting nanofluidic chip.

Connecting the nanofeatures on chip to the ‘world’ (e.g., pump) is necessary to allow precise control and measurement of fluid experiments. While the bulk tubing has a minimum diameter at millimeter range, fluid injection from bulky tubing to nanopore on-chip requires an interface. The challenge is to build the interface that can efficiently (i) inject testing fluid into and vacuum the nanopore on-chip through bulky pumps and (ii) monitor the fluid pressure within the nanopore from bulky pressure transducers. To achieve these, in the nanofluidic device, microchannels are fabricated to connect the nanofeatures and big through holes (~1.6 mm in diameter) drilled on the silicon wafer. The through-holes are then connected to tubing through a self-manufactured chip manifold with O-rings to provide good sealing (Figure 8), and further to piston cylinders (HIP 70C3-10-P), pressure transducers (PX409-3.5KGUSBH) or syringe pumps (ISCO pump) for fluid injection as well as pressure control/monitor. Whenever the fluid pressure in the nanopore is an important parameter to test and measure (e.g., probing the initiation of phase change in nanopores), the nanopore is designed as a dead end of the fluidic channel to avoid pressure drop caused by fluid flow. In this case, the pressure measured through the pressure transducer can accurately inform the fluid pressure within the chip and importantly nanopore. In some other cases, nanopores on-chip play as a flow media, where pressure/pressure drop within the connected microchannels are more important, and are also monitored through the pressure transducer connected to the chip.

Another challenge is to control and monitor the temperature around the nanopores. To build a desired temperature field on the chip, depending on the temperature range, either the water bath (278 – 363 K, Cole-Parmer Polystat® Standard 6.5L Heated Bath) or electric cartridge heater (363 K – 573 K, OMEGA CIR-1030) can be used, to connect with copper blocks closely attached to the silicon back surface through heat conductive paste. These heat/cool sources take on-chip temperature as a feedback for control. The on-chip temperature is measured through

thermocouples inserted into the chip through microchannels etched on the silicon. The tips of thermocouples are located close to the nanofeature region (~50 um away from the nanopore) to provide accurate temperature measurement and PID control feedback. In general, the whole area of interest where nanopore located is setting at the same temperature, confirmed by measurement. The in-situ fluid behavior is directly observed through an optical microscope through the glass side of the chip. Images/videos are recorded with a camera connected to the microscope.

### Key Alberta Innovates points:

- Nanofluidics serves as a window in screening enhanced tight oil recovery strategies at the pore-scale highly relevant to Montney and Viking formations.
- High temperature and pressure are achieved within the nanofluidics and manifold to provide close simulation of Alberta shale reservoirs.
- Direct observation enables in-situ quantification of hydrocarbon phase behaviors relevant to Alberta shale reservoirs.

### 3.3 Experimental procedures

#### Component 1: Single component hydrocarbon condensation in 1-D sub-100 nm channels

The assembled nanofluidic chip was installed on a customized manifold enabling appropriate sealing for high pressures. The chip and manifold were connected to a sample source cylinder (research grade propane, Praxair 99.99%), pump (TELEDYNE ISCO MODEL 260D), and piston cylinder (HIP 70C3-10-P) via tubing and valves. The tubing, pump, piston chambers and valves were cleaned thoroughly before connecting to the nanofluidic chip. The entire system was vacuumed at  $2 \times 10^{-7}$  MPa (PFPE RV8) for 3 hours ( $\sim 10 \text{ m}^3/\text{h}$  as the displacement rate) before each set of experiments to minimize the residual air in the system (the mass fraction of the air was less than  $10^{-4}\%$  of the mass of propane in the system during the experiment). Research-grade liquid propane was filled with high pressure (4 MPa) into the nanochannels. The temperature and pressure were then set below the liquid-vapor saturation line to ensure vaporization of liquid propane. The vapor pressure was provided and controlled by the pump and monitored by a pressure transducer (PX409-3.5KGUSBH) near the chip. The temperature in the chip was controlled by a copper block heater (33 mm along the channel direction and 50 mm perpendicular to the channel direction) and chiller (10 mm along the channel direction and 50 mm perpendicular to the channel direction) clamped on the top of the chip (Figure 9).

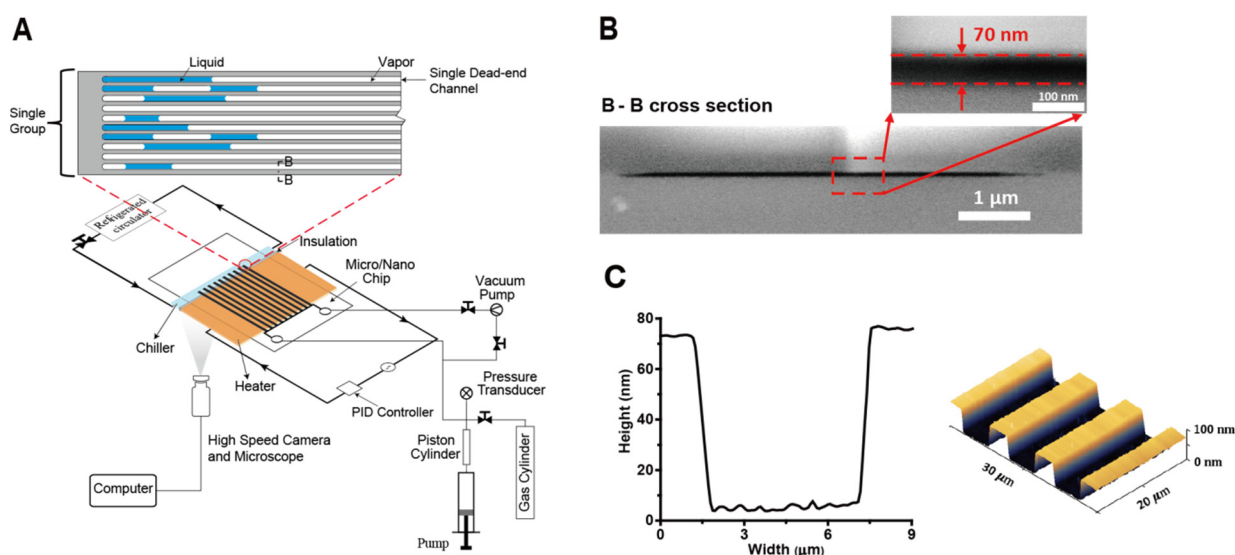


Figure 9 Diagram of the experimental setup and SEM/AFM characterizations of 70-nm high channels. (A) Schematic of the experimental setup. (B) SEM images of the cross-section of one nanochannel. (C) Typical AFM results of a series of nanochannels. Each channel has a width of  $5.5 \mu\text{m}$  and a nominal height of 70 nm (actually  $68.0 \pm 1.1 \text{ nm}$ ). The left image shows the depth profile of a single channel; the right image is a topological scan of 3 adjacent channels.

The test region, the field of view, ( $\sim 1.5 \times 1.5 \text{ mm}$ ) focused on the dead-end portion of the group of 10 nanochannels. To ensure condensation initiated within test region, we introduced a temperature difference across the chip by pairing the heater and chiller. The entrance region of the nanochannels was set at a high temperature ( $T_H$ ) using electric heaters (OMEGA CIR-1030, temperature was constantly set to  $473 \pm 1 \text{ K}$ ) inserted in the block heater controlled by PID, which

covered the first 29 mm length of the nanochannels. The copper dead-end portion of the nanochannel was set at a lower temperature ( $T_C$ ). The temperature in this region was controlled by a refrigerated circulator (Cole-Parmer Polystat® Standard 6.5L Heated Bath, temperature is controlled between  $278.2 \pm 0.3$  K to  $368.2 \pm 0.3$  K) circulating water in the copper block chiller, which covered the last 5 mm length of the nanochannels (the total length of the chiller was 10 mm). Both the heater and the chiller were in close contact with the silicon side of the chip using thermally conductive paste (OMEGATHERM@201) for minimizing contact thermal resistance. An insulation layer (Alumina Oxide Fiber, ~1 mm thick) was placed between them. A high-speed camera (PCO 1200S, 50 frames per second) connected to the inverted optical microscope (LEICA DMI 6000B) with a 10 x objective was used to observe the condensation directly and to record the condensation growth process in the test region of the nanochannels.

For the isothermal condensation experiments (constant  $T_C$ ), the temperature of the water bath was set constant at 318.2 K and we waited 1 hour to reach steady-state thermal conditions. The pressure was increased from 1MPa directly to the target pressure (1.4 MPa to 3.4 MPa, in steps of 0.2 MPa), and for each pressure, we waited 30 minutes to detect any condensation. For the isobaric condensation experiments, the pressure was kept at 1 MPa first, and temperature of the water bath was increased from 303.2 K to 343.2 K (5 K as an incremental step). For each temperature, we waited 1 hour to reach steady-state thermal conditions. Then we increased the pressure from 1 MPa to 2.8 MPa (within 10 seconds). We also waited 30 minutes to detect the condensation. Figure 5 shows the experimental conditions in the phase diagram of propane. As seen there, hollow symbols indicate that condensation was not detected within 30 minutes of observation while the solid symbols indicate that condensation occurred within that period. As can be seen, supercooling was required to detect condensation within the 30 minutes of observation time.

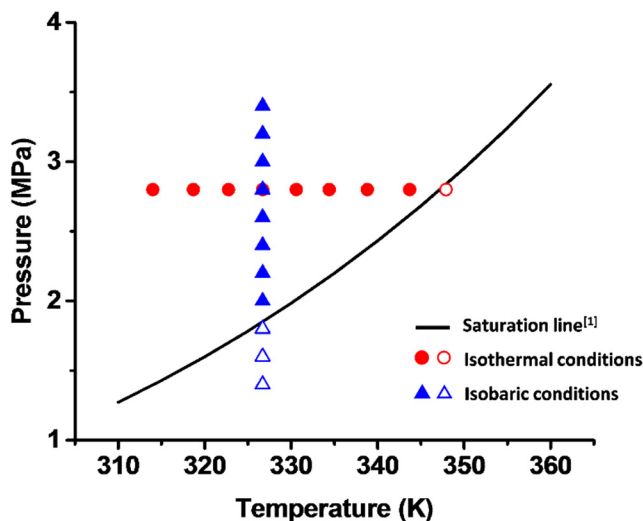


Figure 10 Condensation experimental conditions. The solid symbols indicate that condensation was detected within 30 minutes of observation while the hollow ones indicate no condensation was detected within 30 minutes.

## Component 2: Single component hydrocarbon condensation in 1-D sub-10 nm channels

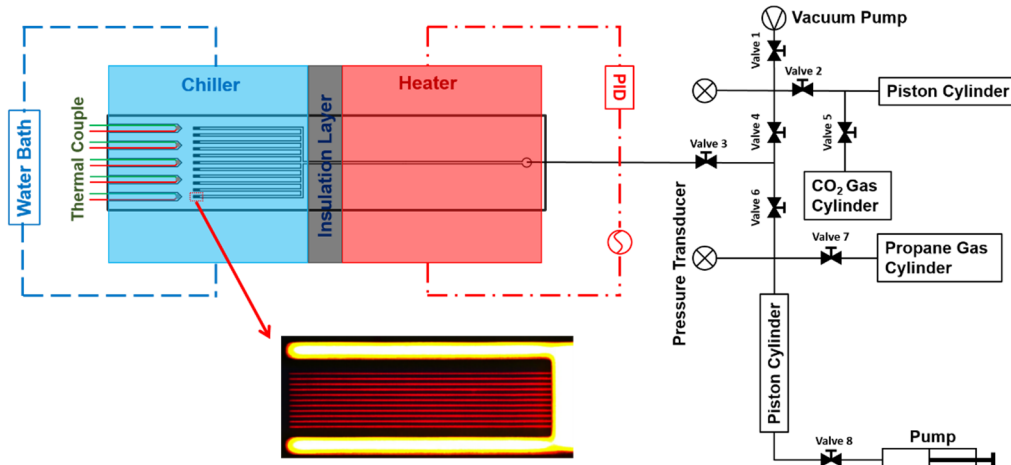


Figure 11 Diagram of the experimental setup. Nanofluidic chip mounted on the manifold, where propane pressure is closely controlled through pump and piston cylinder via tubing and valves, and CO<sub>2</sub> can also be connected to the chip for surface aging test. Temperature gradient on the chip is introduced through a copper chiller controlled by the water bath and a copper heater controlled by the electric cartridge heater.

The diagram of the experimental system is shown in Figure 11. The chip and manifold were connected to a propane gas cylinder (99.99% research grade, Praxair), CO<sub>2</sub> gas cylinder (99.99% research grade, Praxair), pump (TELEDYNE ISCO MODEL 260D), and piston cylinder (HIP 70C3-10-P) via tubing and valves. The tubing, pump, piston chambers and valves were cleaned thoroughly before connection to the nanofluidic chip. At first use of the chip, the entire system was vacuumed at  $2 \times 10^{-7}$  MPa (PFPE RV8) for 3 hrs at room temperature (293.15 K), followed by isolation for another 3 hrs to perform a leak test. Devices were vacuumed for 3 hrs prior to each set of experiments to minimize the residual air in the system (the mass fraction of air within the device during a propane condensation experiment is estimated to be below  $10^{-4}$ % of the mass of propane). Next, propane vapor was introduced into the devices at a temperature and pressure of 373.15 K and 1 MPa for 1 hr to age the channel surface, followed by vacuuming for additional 3 hrs. Channels are then deemed ready for condensation testing. To promote condensation in the nanochannel, the temperature difference across the chip was induced by pairing a cooper block chiller (controlled by a water bath, Cole-Parmer Polystat® Standard 6.5L Heated Bath, error is  $\pm 0.01$  K) and heater (controlled by electric heaters with PID, OMEGA CIR-1030, error is  $\pm 1$  K) clamped on the bottom (silicon side) of the chip with thermally conductive paste (OMEGATHERM@201) for minimizing contact thermal resistance (Figure 11). The chiller (10 mm along the channel direction and 50 mm perpendicular to the channel direction) was positioned over the nanochannel region (the center of the chiller exactly covers the nanochannel region), and was separated by a thick insulation layer (Alumina Oxide Fiber,  $\sim 1$  mm thick) from the heater (10 mm along the channel direction and 50 mm perpendicular to the channel direction) at the chip inlet. The chiller temperature was adjustable according to the experimental conditions, and the heater's temperature was maintained at 473 K ( $\pm 1$  K). For each test, thermal equilibrium was first established and monitored via thermocouples inserted within microchannels adjacent to the nanochannel region (Figure 6a). Afterwards, propane was introduced into the nanofluidic chip (monitored by the pressure transducer, PX409-3.5KGUSBH, Figure 11), and condensation behavior was captured using a camera (Leica DMC 2900) connected to the optical microscope

(Leica DM 2700M). The liquid-vapor interface position and the condensate length were extracted from image sequences using an image processing algorithm using MATLAB.

### **Component 3: Single component hydrocarbon bubble nucleation in 1-D sub-100 nm channels**

Similar to the condensation experimental procedure, the chip and manifold are connected to a sample source cylinder (research grade propane, Praxair 99.99%), syringe pump (TELEDYNE ISCO MODEL 260D), and isolation piston cylinder (HIP 70C3-10-P) via tubing and valves. Research-grade liquid propane is filled into the nanochannels. In the initial filling to a brand new chip, the temperature and pressure are set far below the liquid-vapor saturation line to ensure that vapor propane diffused and completely filled the nanochannel. The temperature in the chip is controlled by a pair of copper-made heater and chiller clamped on the top of the chip.

A high-speed camera (PCO 1200S, 50 frames per second) connected to the optical microscope (LEICA DMI 6000B) with a  $10\times$  objective lens is used to observe the bubble nucleation and to record the vapor column growth. The field of view ( $\sim 1.0\times 1.0$  mm) is located on the dead-end portion of the group of 10 nanochannels. To ensure bubble nucleation initiated within the field of view, we introduced a temperature difference across the chip by pairing a heater and a chiller. The entrance region of the nanochannels is set at a lower temperature ( $T_{low}$ ) using the chiller with a water circulating bath. The dead-end portion of the nanochannel is set at a high temperature ( $T_{high}$ ). The temperature  $T_{high}$  is controlled by the heater with a water / silicon oil circulator bath. The dead-end of nanochannel is located at center of the 10-mm long heater. In other words, the heater covers the last 5 mm length of the nanochannels. Both the heater and the chiller are tightly contacted with the silicon side of the chip using mechanical clamp to minimize contact thermal resistance.

The temperature of the chiller water bath is set constant at 288 K. The temperature of copper heater  $T_{high}$  is set at different temperatures ranging from 342.4 to 375.9 K. For each temperature,  $T_{high}$ , the pressure is initially set at a point above the saturation pressure of  $T_{high}$  to ensure that the fluid in all the nano- and micro-channels is in the liquid phase. For each temperature,  $T_{high}$  is kept constant for 1 hour to reach thermal equilibrium before conducting experiments. The pressure is gradually decreased in steps of 0.1 MPa. At each pressure step, 15-minute waiting time is given to observe bubble nucleation. Cycles of pressure drawdown are repeated until bubble nucleation occurs. Figure 12 shows an example of one round of operation pressures in the propane phase diagram; hollow symbols indicate that bubble nucleation is not detected within 15 minutes of observation while the solid symbols indicate that vapor bubble nucleated within 15 minutes. In total, eight different temperatures ( $T_1 = 342.4, 346.3, 351.3, 356.2, 361.2, 366.1, 371.0$  and 375.9 K) are performed.

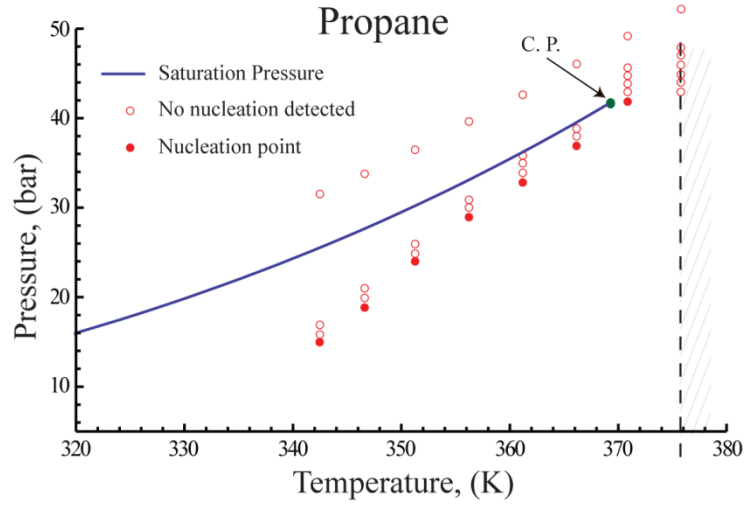


Figure 12 Operation pressures of pressure-drawdown experiment

**Component 4: Mixture hydrocarbon phase behavior at a mixed nano-macro length scale**

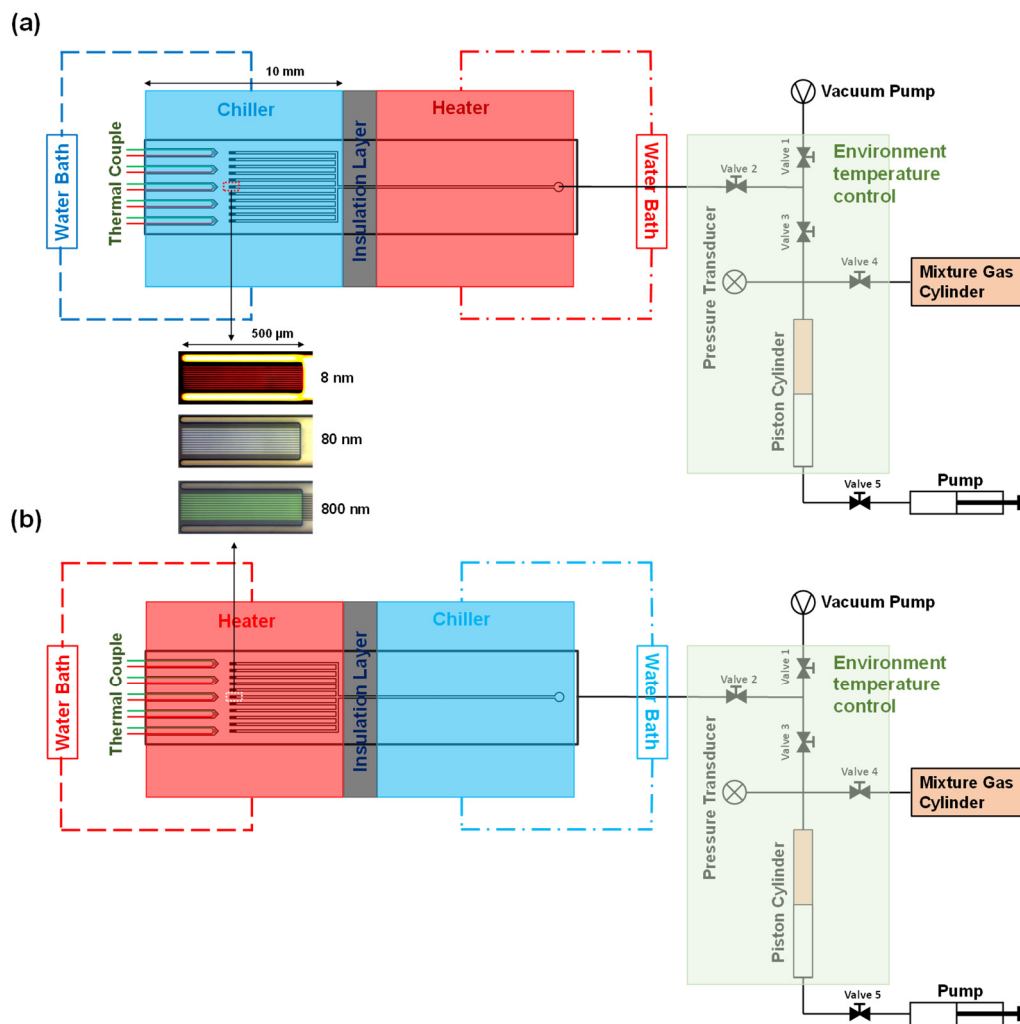


Figure 13 Diagram of the experimental setup. Nanofluidic chip mounted on a manifold capable of connecting the chip to pipelines, where the methane/propane mixture pressure was closely controlled through the pump and piston cylinder. A temperature gradient on the chip was introduced through the copper heater/chiller, controlled by water baths, and monitored by thermocouples inserted into the chip close to the nanochannel. The environmental temperature was also closely controlled during the experiments. To study the mixture dew point, the temperature around nanochannels was set as the lowest within the entire system, (a). To study the mixture bubble point, the temperature around nanochannels was set as the highest within the entire system, (b).

The experimental system is shown in Figure 13. The chip and manifold were connected to a methane/propane mixture gas cylinder (20% mole concentration methane balanced by propane, Praxair Canada Inc., purity > 99.99%), syringe pump (TELEDYNE ISCO MODEL 260D, resolution at 0.001 MPa), and piston cylinder (HIP 70C3-10-P). At first use, the entire system was vacuumed at  $2 \times 10^{-7}$  MPa (PFPE RV8) for 3 hrs at room temperature (293.15 K), ensuring the impurity introduced by air is <0.01%, followed by isolation for another 3 hrs to perform a leak test. The temperature gradient was introduced and controlled by two water baths (Cole-Parmer Polystat® Standard 6.5L Heated Bath, error is  $\pm 0.01$  K), through two copper blocks (10 mm along the channel direction and 50 mm perpendicular to the channel direction) clamped on the silicon side of the chip, namely chiller and heater. The chiller and heater positions could be changed based on the nature of tests performed (i.e., dew point test or bubble point test), and were separated by a thick insulation layer (Alumina Oxide Fiber,  $\sim 1$  mm thick). The region of interest (500  $\mu\text{m}$  long nanochannels) was designed to be covered by the center of the chiller/heater as specified in Figure 6, in which the nanochannels were ensured to be tested under isothermal conditions. During the test, the system pressure was monitored by the pressure transducer (PX409-3.5KGUSBH). Mixture phase behavior was captured directly and observed in real-time using a camera (Leica DMC 2900, recording at 5 frames per second) connected to the optical microscope (Leica DM 2700M). The spatial resolution for the image was 0.3  $\mu\text{m}/\text{pixel}$ . The experimental setup described here is similar to the experimental setup used in our previous work on pure hydrocarbon condensation<sup>1</sup>.

To study the dew point of the mixture, the temperature gradient was first applied on the chip through two water baths. The temperature of the environment, inlet of the chip as well as the microchannel region were maintained at 300.15 K, and the region containing the dead-end nanochannels was set to temperatures from 282.15 to 300.15 K (3 K as the interval). Under these conditions, the condensation was forced to initiate from the dead-end region when the system is pressurized (initially a pure vapor phase). The fluidic network was first vacuumed for three hours, and loaded with premixed methane/propane mixture (1 : 4 mole ratio) at 0.55 MPa and 300.15 K as gas. At isothermal condition, the entire system was pressurized stepwise (0.01 MPa) with a syringe pump. Diffusion in the 500  $\mu\text{m}$  long nanochannel requires  $\sim 3$  min to reach equilibrium. The pressure of the initiation of condensation in nanochannels was detected in real-time via an optical microscope and a pressure transducer monitoring the entire system.

To perform the pressure drawdown for studying the mixture bubble point, similarly a temperature gradient was firstly introduced across the chip. In this case the setup environment, inlet of the chip as well as the microchannel region were maintained at 278.15 K, and the dead-end region was set

at 288.15 K. The cavitation was thus forced to initiate at the dead-end region when the system was depressurized from a pure liquid phase. After vacuuming the system and filling the system with a gas mixture, the entire system was pressurized to 4.5 MPa at isothermal conditions, and the mixture was in liquid phase.

The first pressure drawdown test was in the equilibrium condition as a control group, where the system pressure was reduced stepwise (0.05 MPa) with a 15 min waiting time at each step. The results are recorded for later comparison. Then, continuously pressure drawdown was performed by mixture volume expansion at a constant rate provided by the syringe pump. The slow expansion rate (50  $\mu\text{L}/\text{min}$ ) and fast expansion rate (50 ml/min) led to different pressure drawdown curves. During the slow expansion, the mixture vaporization dynamics and the initiation of vaporization were very close to that detected in the equilibrium pressure drawdown. This similarity explains how such a slow pressure drawdown rate allowed the system to reach pressure and chemical potential equilibrium everywhere at any given moment. Therefore, this test could be considered a near-equilibrium pressure drawdown case. In the fast expansion case, however, the rate of pressure change was much greater than that estimated by the diffusion rate. The results here were very different from the results of the equilibrium pressure drawdown, and thus this test can be considered as an example of non-equilibrium pressure drawdown.

### Component 5: Single component hydrocarbon evaporation in 2-D sub-10 nm nanogrids

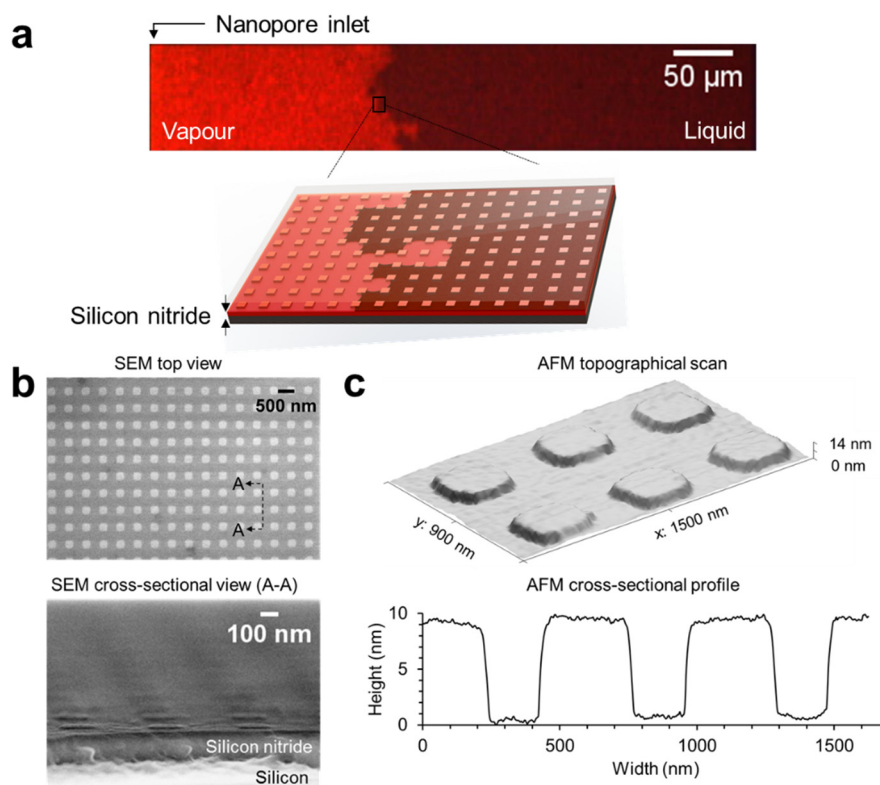


Figure 14 2D sub-10 nm porous media for hydrocarbon evaporation (a) Optical microscopy image of evaporation in the 2D nanoporous media with clear distinction between the vapour (light red)

and the liquid phase (dark red). The nanoporous media is 500  $\mu\text{m}$  long and 80  $\mu\text{m}$  wide. In this example, evaporation proceeds from left (nanopore inlet) to right (dead-end). Panel below shows a sketch of the pore scale evaporation mechanism. (c) Scanning electron microscopy (SEM) images of the nanoporous media showing the top view (top panel) and cross-sectional view (bottom panel). (d) Atomic force microscopy (AFM) image of the porous media topography (top panel) and a cross sectional profile of the pattern (bottom panel). Each pore is 225 nm wide and 9 nm deep.

Figure 14 shows the experimental schematic of the set-up and characterization of the nanoporous media. The nanopores were patterned using electron beam lithography on a silicon wafer coated with 200-nm thick silicon nitride film and a 9-nm thick silicon dioxide film and etched to form the nanopores as shown in SEM and AFM images in Figure 8b and c, respectively (nanopore depth and width of  $8.86 \pm 0.16$  nm and  $224.9 \pm 2.5$  nm, respectively). Following etching of the microchannels and drilling of the inlet holes, the nanopores were sealed via an anodically bonded glass layer to complete the chip fabrication. During the experiments, the pressure of vapor propane and temperature in the nanopores was closely controlled and measured. A typical snapshot of evaporation in the nanoporous media under the bright field of the optical microscope is shown in Figure 14a.

### Component 6: 2-D nanogrids in screening enhanced tight oil recovery strategies

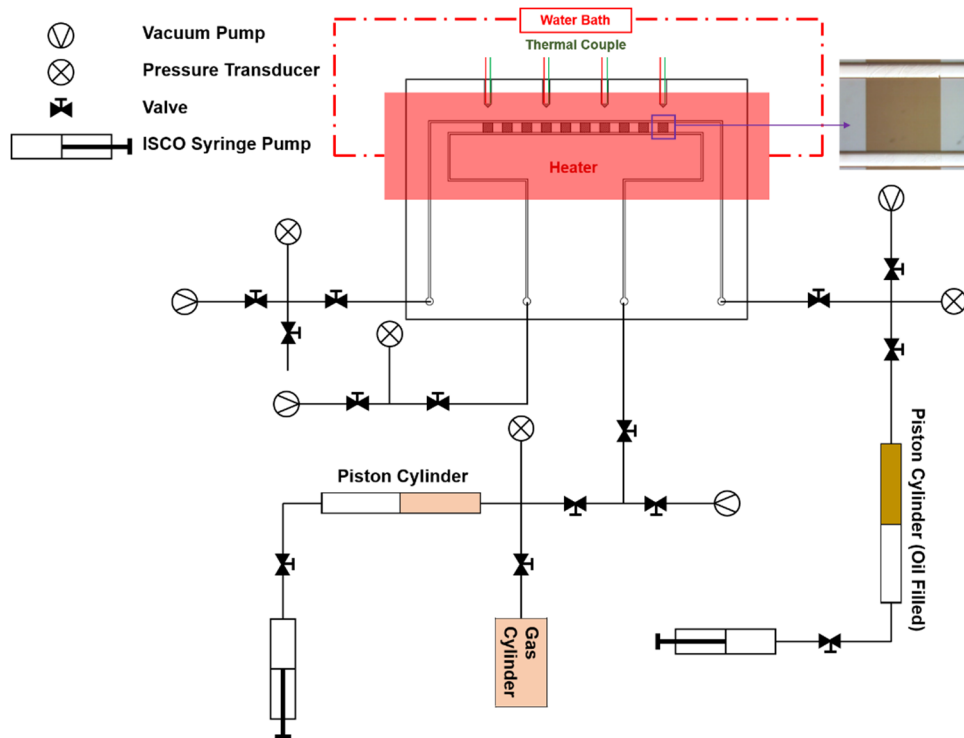


Figure 15 Diagram of the experimental setup for N<sub>2</sub> and CO<sub>2</sub> flooding tests. The nanofluidic chip was mounted on a manifold to connect microchannels with pipes. Pressures of gas as well as oil

were closely controlled through ISCO syringe pump, and monitored through pressure transducers. Temperature on the chip was introduced through a copper heater controlled by a water bath (323.15 K), and monitored by thermocouples inserted into the chip close to the nanoporous media.

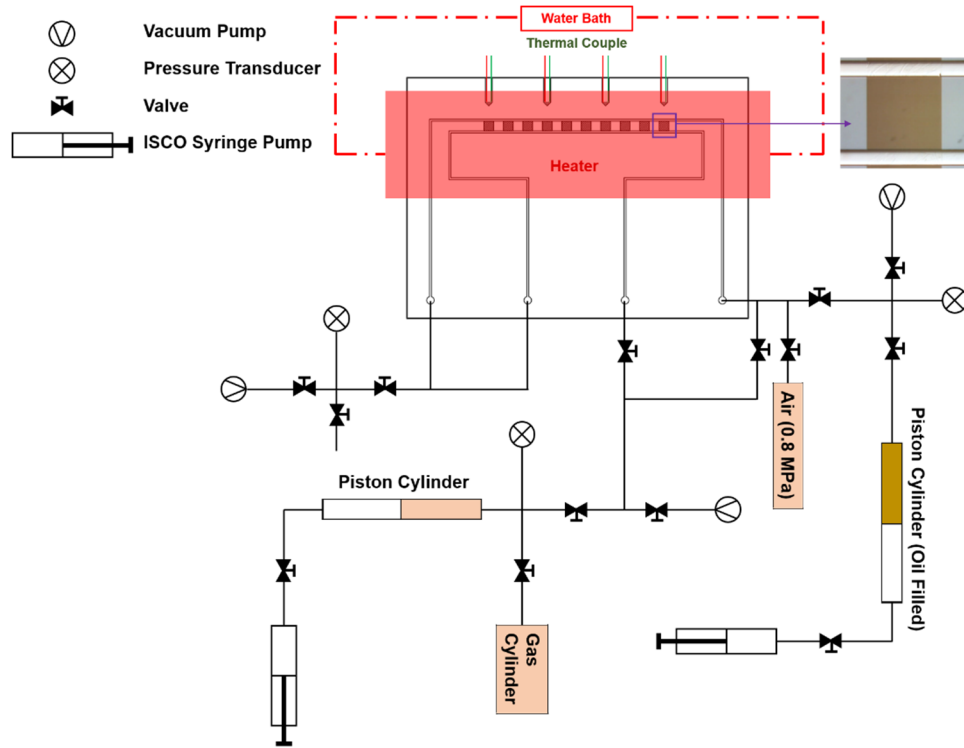


Figure 16 Diagram of the experimental setup for CO<sub>2</sub> huff-and-puff tests.

To perform the flooding tests, the system (Figure 15) was firstly vacuumed at  $2 \times 10^{-7}$  MPa (PFPE RV8) for 3 hrs at room temperature (293.15 K) to ensure oil filling fully into the nanoporous media (i.e., no air trapping in the nanoporous media). After that, the oil was injected into one microchannel through syringe pump (TELEDYNE ISCO MODEL 260D, resolution at 0.001 MPa), as well as the nanoporous media at 1 MPa. Due to the capillary force, the filling would stop at the entrance of the nanoporous media on the gas channel side. Then gas at targeting pressure was injected into another microchannel. During the gas injection, oil was kept at the same pressure with gas to avoid any unexpected flooding below the targeting gas pressure. To start the flooding test, oil pressure was reduced to 5 MPa (taking less than 3 s). Flooding phenomena were observed directly through an optical microscope (Leica DM 2700M) and camera connected (Leica DMC 2900).

To perform the huff-and-puff tests (Figure 16), after vacuuming and oil injection, the oil microchannel was purged by air at 0.8 MPa for 1 hr to clean any residual oil, ensured by the vanishing of any fluorescence signals in the microchannel. The system was then vacuumed for another 1 hr to ensure no air trapped in the system. Afterwards, the gas was injected into both microchannels at targeting pressures, followed by sealing for 1 hr to allow sufficient gas diffusion

into nanoporous media. In the end, the gas pressure was reduced to targeting value (1 MPa) to produce oil from the nanoporous media.

### Component 7: 2-D nanogrids in simulating shale gas primary recovery

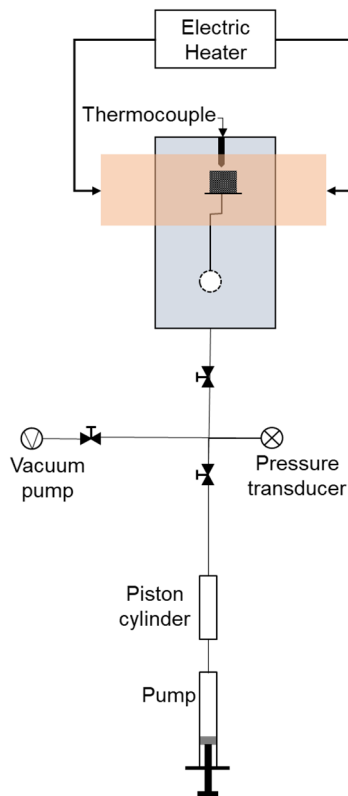


Figure 17 Schematic of the experimental set-up. For clarity, only a nanomodel is shown.

The nanofluidic device was mounted on a custom-built high-pressure, high-temperature manifold and connected to the experimental set-up shown in Figure 17. All components of the set-up (tubing, piston cylinder, valves and manifold) were thoroughly cleaned using DI water and dried using an air gun. The nanofluidic chip was placed under an optical microscope (Leica DM 2700M) with a 10X objective lens, allowing the visualization of evaporation in two different nanoporous media simultaneously. Evaporation was recorded using a camera (Leica DMC 2900).

Temperature was controlled by placing a copper block connected to an electric heater (accuracy  $\pm 0.1$  °C) below the location of the nanomodel. The experimental temperature ( $T$ ) was determined by measuring the temperature close to the nanomodel by inserting a thermocouple in a 400  $\mu\text{m}$  deep channel etched 1-mm above the location of the nanomodel. Over the course of the experiment, the temperature variation was approximately  $\pm 0.5$  °C. The hydrocarbon mixture was produced in-lab by combining a mixture of 80% propane and 20% methane (mol. fraction, Praxair Canada) and pentane (Sigma Aldrich) in a piston cylinder in liquid-phase. The final liquid composition was 10% methane, 40% propane and 50% pentane (mol. fractions). Pressure in the chip was controlled using an ISCO pump and measured using a pressure transducer (accuracy  $\pm 1$  kPa).

Prior to running the experiments, the entire system was vacuumed for three hours at  $2 \times 10^{-4}$  kPa (PFPE RV8) to remove residual air from the system. The nanomodel was initially filled with liquid sample at pressures above the bubble point pressure at room temperature (4 MPa). After waiting ~12 hours to reach the compositional equilibrium condition, temperature was increased to the experimental temperature,  $T$ , using the electric heater. Experimental temperatures here included 42.5°C, 62.5°C and 82.5°C. After waiting one hour to allow the system to reach thermal equilibrium, pressure was lowered to a target pressure below the bubble point pressure to observe evaporation. At each temperature, pressure was lowered to 2 MPa and 1 MPa and finally to vacuum. At each increment, the waiting time of 15 minutes was set to observe vaporization.

### Key Alberta Innovates points:

- Experiments are conducted at conditions highly relevant to Alberta shale reservoir conditions;
- Efficiently screening gas injections for enhanced tight oil recovery for Alberta shale reservoirs;
- Simulating the shale gas production process in a pore throat (5 nm) governed large pore (80 nm) network that is highly relevant to the Montney and Viking shale formations;
- Validating classical thermodynamics at shale nanopore-fracture connected geometries in shale through a nanofluidic device.

## 3.4 Results and discussions

### Component 1: Single component hydrocarbon condensation in 1-D sub-100 nm channels

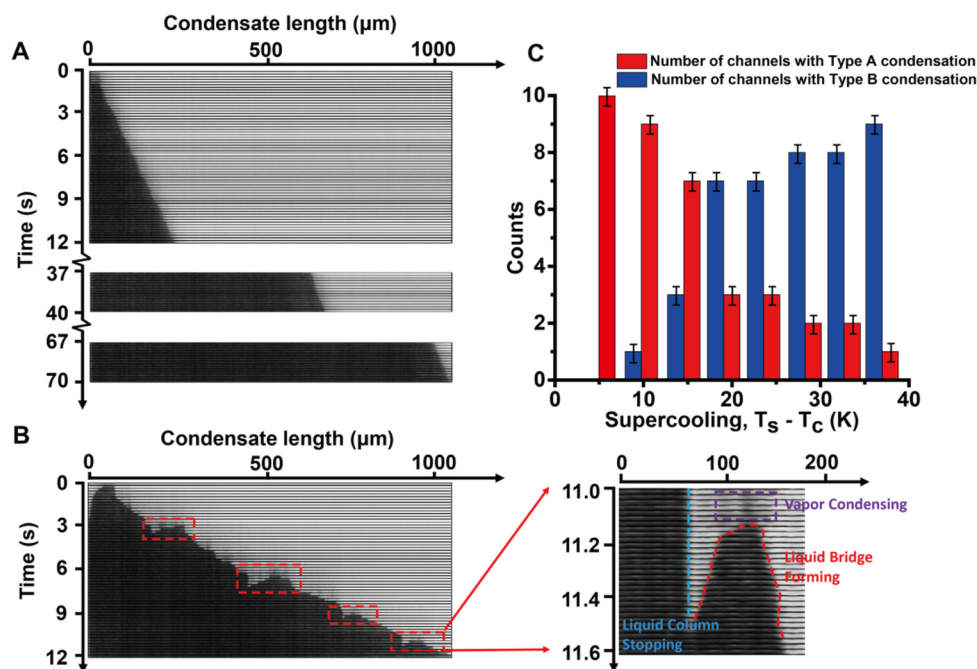


Figure 18 Direct observation of two types of propane condensation (Type A and Type B) in a 70 nm high channel at (A) 2.8 MPa/343.7 K and (B) 2.8 MPa/314.0 K. The time interval between each frame in (A) and (B) is 0.2 s (0.02 s for the zoom-in image in (B)). (C) The number of channels with Type A and Type B condensation in a group of 10 nanochannels and three repeats as a function of supercooling at 2.8 MPa.

Image sequences of the vapor condensation and condensate growth in a nanochannel versus time (with a sampling speed of 50 frames per second) are shown in Figure 18. The condensed liquid phase advanced from the dead end of the channel toward to channel inlet. The corresponding vapor flowed from the inlet toward the dead end. Two different condensation and condensate growth mechanisms were observed, depending on the experimental conditions. Figure 18A shows Type A condensation where the condensation started at the dead end, and the single liquid column grew continuously towards the inlet of the nanochannel as a result of condensation. In Type B condensation, the initiation of condensation was also close to the dead-end point. However, the progression of the liquid-vapor interface was not continuous. Rather, it consisted of a repeating pattern of growth followed by liquid bridging ahead of the liquid column front. An example of this pattern is shown in Figure 18B, and as seen in the inset of Figure 18B, once the liquid bridge initiated, the original interface would stop growing, but the liquid bridge continued to grow in both directions and, eventually, the vapor bubble between the two liquid-vapor interfaces disappeared.

The total condensate length versus time in the 70-nm deep nanochannel at 326.7 K and five different pressures is shown in Figure 8A. For Type B growth cases, the total condensate length was calculated as the sum of the liquid lengths in the nanochannel. Linear relations between the condensate length and time were found for all conditions. The growth rates are plotted vs. pressure

in Figure 19B. Figure 19C shows the total condensate length versus time in the 70-nm high channel at 2.8 MPa for five different temperatures. Similarly, linear relationships between the condensate lengths versus time were found for all temperatures. Figure 19D shows the isobaric condensate growth rate at different temperatures. The condensate growth rates in Figure 19B and D are calculated by fitting a linear regression line to the condensate length of Figure 19A and C.

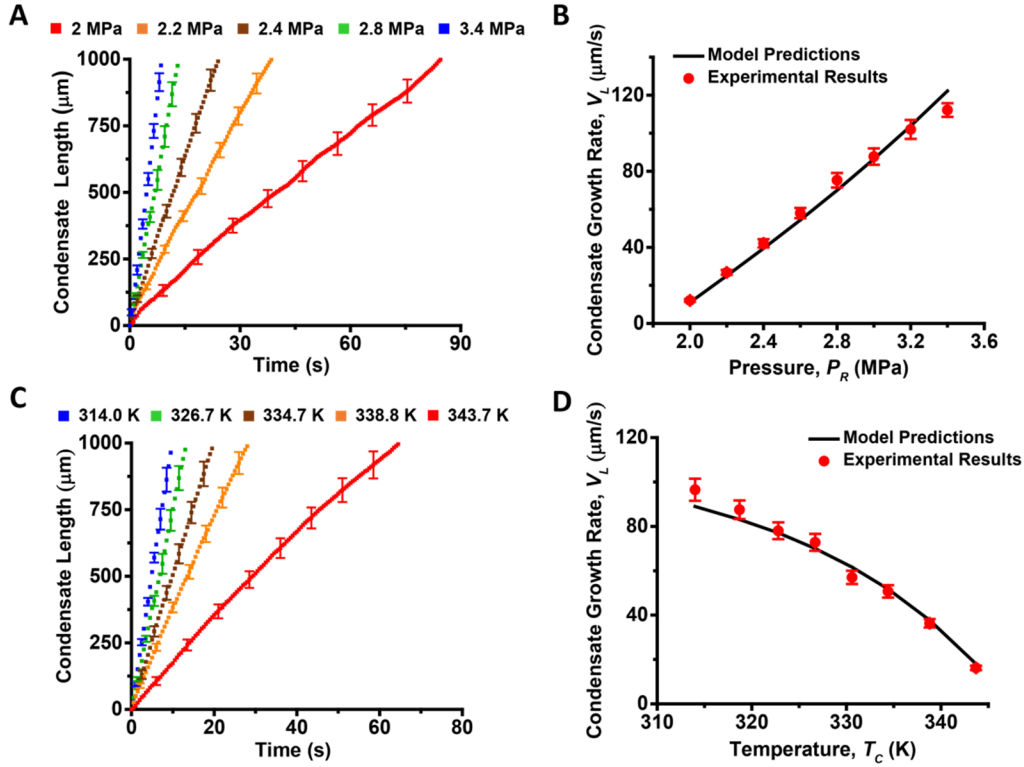


Figure 19 Condensate length and condensate growth rate as a function of pressure and temperature in 70-nm high channel. (A) Condensate length versus time at 326.7 K ( $T_C$ ) and different pressures. Each measurement point is a result of the average of 3 repeated experiments in the 10 nanochannels. Representative error bars are shown for 8 of the measurement points at most (error bars for remaining data points are omitted for clarity). The time interval for each of the two data points plotted is 0.5 s. (B) Condensate growth rate as a function of pressure calculated from the condensate length in (A). (C) Condensate length versus time at 2.8 MPa ( $P_R$ ) and different temperatures (time interval of 0.5 s between data points). (D) Condensate growth rate as a function of temperature calculated from the condensate length in (C).

To analyze the condensate growth in the nanochannel, we employed a resistance model (see Figure 20). During the condensation process, there are three major resistances in series between the nanochannel entrance and the condensed liquid phase: (i) flow resistance in the heater region of the nanochannel (RH), (ii) flow resistance in the chiller region of the nanochannel (RC), and (iii) the resistance to crossing the liquid-vapor interface (RI).

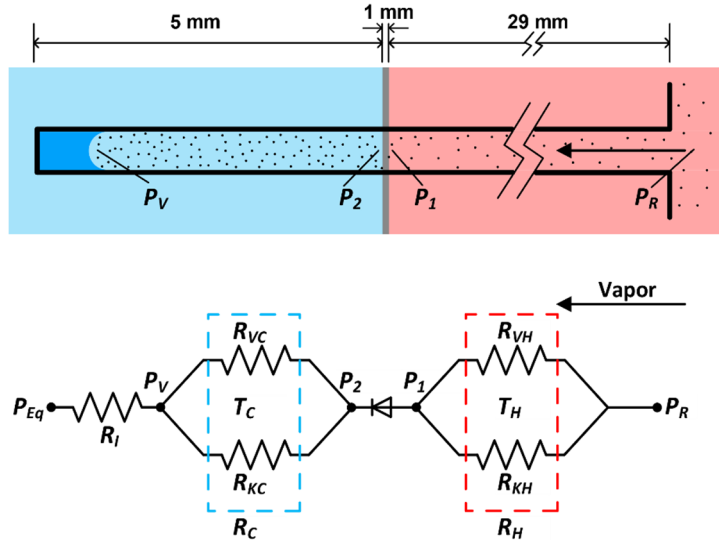


Figure 20 Flow resistance model for condensate growth in the dead-end nanochannel.

The modeling results indicate that flow resistance (i.e.,  $R_H + R_C$ ) accounts for  $\sim 70\%$  of the total resistance in our experiments, especially when the pressure ( $P_R$ ) or temperature ( $T_C$ ) is decreased. For example, the contribution of flow resistance to the total resistance is increased from 71% at 3.4 MPa to 74% at 2.0 MPa in isothermal conditions (Figure 21A), and from 67% at 343.7 K to 76% at 314.0 K in isobaric conditions (Figure 21B). Therefore, it is essential to take both flow resistance and interface resistance into consideration when studying condensate growth in nanoconfinement.

In contrast, if the scale of the system was increased an order of magnitude to 1  $\mu\text{m}$ , the ratio of the flow resistance to the total resistance would decrease from  $\sim 70\%$  to less than 1% (for similar thermodynamic conditions). Thus, at the macro- or microscale, flow resistance can usually be neglected, and only heat and mass transfer processes at the interface dominate the condensation process. In the nanochannels, the Knudsen flow also changes the total resistance by  $\sim 10\%$  (8% to 12% depending on the experimental conditions, as is shown in Figure 21C and D). Thus, it is important for Knudsen effects to be considered within the increasingly important flow resistance as scales decrease. In addition, the nonlinear behaviors between the condensate growth rates versus temperature and pressure are predicted by our model and were found to agree closely with our experiments. The nonlinear behaviors are the result of both flow and interface resistances changing nonlinearly with temperature (via density and viscosity of vapor phase), and with pressure (though to a lesser extent).

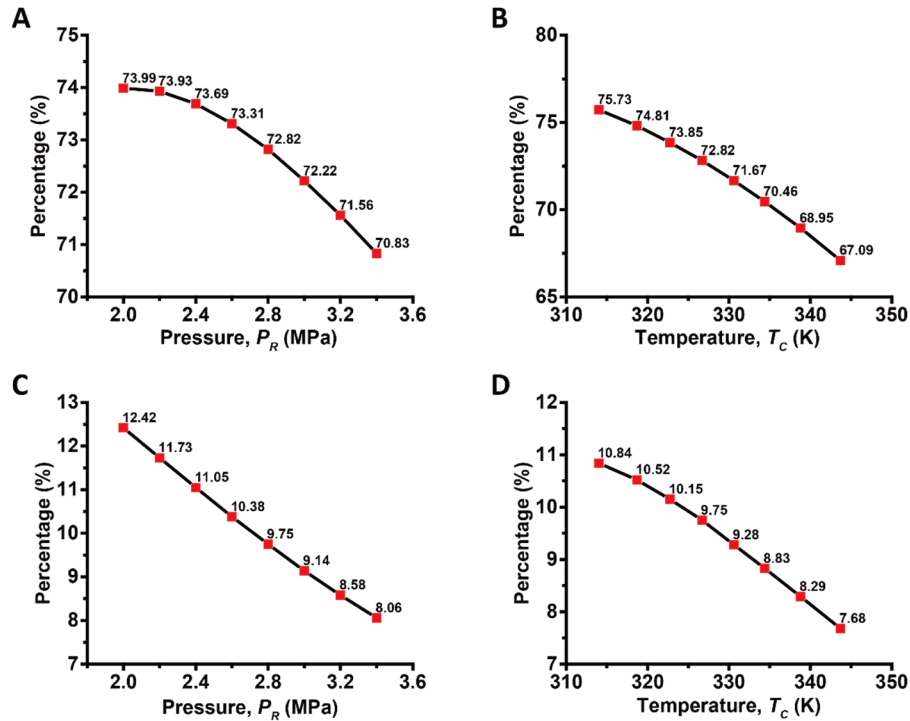


Figure 21 The ratio of flow resistance to the total resistance and Knudsen flow effect to the total resistance without considering Knudsen flow effect at different isothermal and isobaric conditions. (A) The ratio of flow resistance to the total resistance at isothermal conditions. (B) The ratio of flow resistance to the total resistance at isobaric conditions. (C) The Knudsen flow effect to the total resistance at isothermal conditions. (D) The Knudsen flow effect to the total resistance at isobaric conditions.

## Component 2: Single component hydrocarbon condensation in 1-D sub-10 nm channels

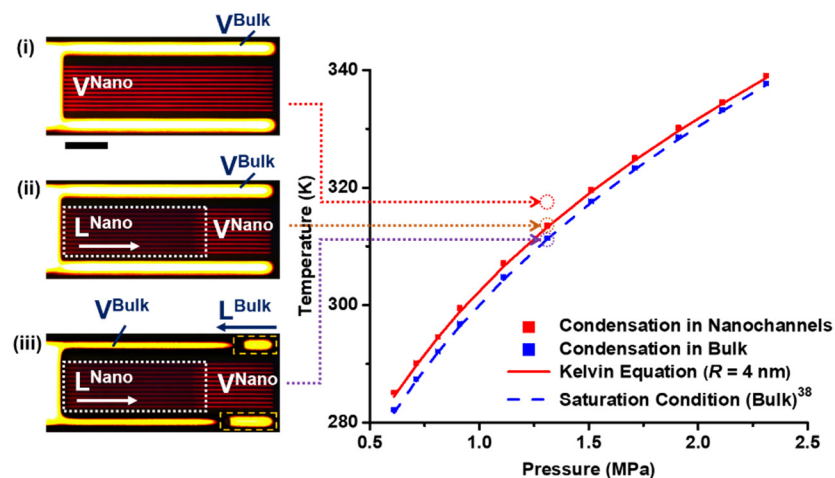


Figure 22 Thermodynamic conditions for condensation at sub-10 nm and bulk scale. Measured condensation conditions at sub-10 nm and in bulk, along with corresponding saturation curves obtained using the Kelvin equation and NIST values, respectively. Each point for the sub-10 nm case represents the average of a total of 33 measurements (3 runs with 11 nanochannels). Each

point for the bulk case represents the average of 6 measurements (3 runs with 2 microchannels). Error bars are smaller than the symbols. Images show system behavior at a pressure of 1.31 MPa at one of three temperatures. When the temperature is above the Kelvin equation prediction, both micro- and nanochannels remain in the vapor phase (light red and light yellow, respectively), (i). When the temperature is near/below the Kelvin equation prediction, capillary condensation occurs, with the condensate growing into the 8-nm nanochannels (the dark red phase), while microchannels remain in the vapor phase (light yellow), (ii). When temperature is near the bulk prediction, condensation occurs and the condensate grows in both the nanochannels and microchannels (dark red and dark yellow, respectively), (iii). The scale bar corresponds to a distance of 100  $\mu\text{m}$  and applies to all microscope images.

We measured the highest condensation temperature for different pressures, at both bulk (i.e., microchannels) and sub-10 nm (i.e., 8-nm nanochannels). In each test, propane was set to the desired pressure first, and pumped into the nanochannel after the target temperature was established on the chip. For each temperature, the system was monitored for up to 1 hr to determine whether condensation initiates, and was fully vacuumed for 30 min between measurements. Testing results are shown in Figure 12, with error bars representing both experimental uncertainty and resolution between runs for a given pressure. The results at sub-10 nm are plotted with that predicted by the Kelvin equation:

$$P^{Eq} - P^S - \frac{R_g T^V}{V_m} \ln \frac{P^{Eq}}{P^S} = \frac{\gamma}{R} \quad (1)$$

Where  $P^{Eq}$  is the equilibrium pressure for capillary condensation under a curved meniscus (i.e., Kelvin pressure),  $P^S$  is the saturation pressure in bulk,  $V_m$  is the specific volume of the liquid at the bulk saturation condition,  $R_g$  is the universal gas constant,  $T^V$  is temperature of the vapor phase,  $\gamma$  is the liquid-vapor interface tension and  $R$  is the main radii of the curved meniscus. We found that within a wide pressure and temperature range ( $\sim 0.6$ - $2.3$  MPa,  $286.15$ - $339.15$  K), predictions from the Kelvin equation based on bulk fluid properties matched the experimental results well. The temperature shift between measured sub-10 nm condensation and bulk condensation (gap between red and blue points, Figure 22,  $\sim 1$ - $3$  K), was at most 8 % different from the temperature shift predicted by the Kelvin equation and bulk phase.

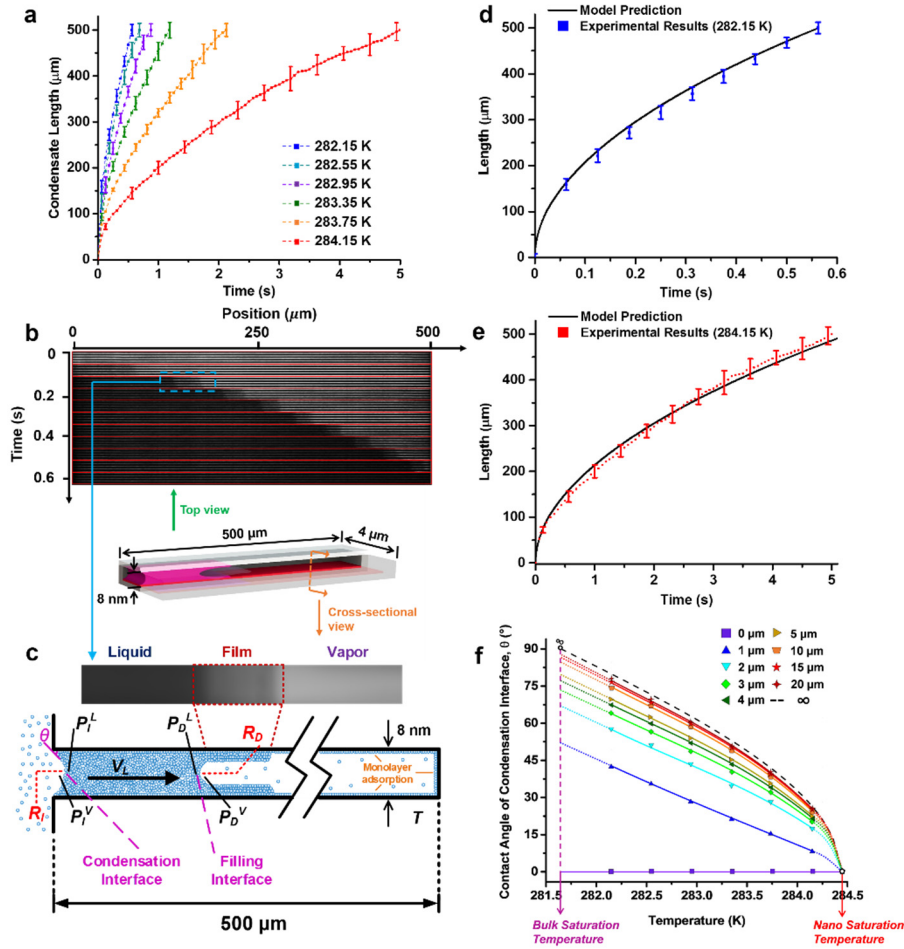


Figure 23 Measurement of condensate growth as a function of superheat at isobaric conditions. (a) Total condensate length versus time for different temperatures, at a pressure of 0.61 MPa. Each point represents the average of a total of 33 measurements (3 runs with 11 nanochannels). Error bars on only selected data points are shown, for clarity. (b) Images depicting condensate growth over time within a group of 5 nanochannels at 282.15 K. Images were stretched horizontally by a factor of 2.5 and contrast-enhanced in black and white for clarity. Red lines separate each frame. (c) Schematic of condensate growth model. The enlarged image of the interface was stretched vertically by a factor of 4 with respect to the original image to highlight the presence of an interfacial film. Fully liquid (black), liquid film (gray) and vapor regions (light gray) are distinguished. (d and e) Model predictions compared to experimental results at 282.15 K and 284.15 K, respectively. (f) The change of contact angle at the condensation interface for different temperatures, as predicted using the model.

The ability to differentiate phases within the sub-10 nm channels uniquely enables the observation of condensation dynamics. Condensate propagation was studied under isobaric conditions (0.61 MPa), with temperature varying between 282.15 K and 284.15 K at 0.4 K intervals. Condensation initiated at the inlet of the nanochannel and grew into the nanochannel with the interface at the inlet pinned. The total condensate length changing over time was measured, and results for

different conditions are shown in Figure 23a. Figure 23b shows typical filling behavior for a group of 5 nanochannels at 282.15 K.

As is shown in Figure 23c, once the initial condensate forms at the inlet, there are two effects that combine to drive condensate growth in the nanochannel: (i) the accumulation of vapor molecules at the condensation interface as a result of capillary condensation, and (ii) the liquid flow as a result of the capillary pressure at the filling interface. We modeled (i) and (ii) with the Hertz-Knudsen equation and Poiseuille law, respectively, and linked these with the conservation of mass. The resulting model expresses condensate length ( $L$ ) changing with time ( $t$ ):

$$\frac{dL}{dt} \frac{h}{2R_I a \sin\left(\frac{h}{2R_I}\right)} = \frac{a}{\rho_L} \sqrt{\frac{M}{2\pi R_g T}} \left( P_I^V - P^S e^{\frac{-\gamma V_m}{R_g T R_I}} \right) \quad (2)$$

Where  $R_I$ , the main radii of the condensation interface, can be expressed as:

$$\frac{1}{R_I} = \frac{2}{h-f} - \frac{dL}{dt} \frac{12\mu L}{h^2\gamma} + \frac{P_I^V - P^S e^{\frac{-2\gamma V_m}{(h-f)R_g T}}}{\gamma} \quad (3)$$

Where  $h$  is the height of the nanochannel,  $f$  is the thickness of the liquid film in front of the filling interface (Figure 23b and c), which was measured through imaging,  $a$  is the condensation coefficient (equals to unity for non-polar molecules),  $\rho_L$  is the liquid phase density,  $M$  is the molar mass of the fluid,  $T$  is the temperature for the system,  $P_I^V$  is the vapor pressure at the condensation liquid-vapor interface,  $\mu$  is the viscosity of the liquid phase. Solving this system numerically for the highest and lowest temperature cases provides the model predictions in Figure 23d and e. In all cases, the model predicts the total condensate growth well. For example, the predicted time for full condensate filling of the nanochannel was within 6% of the experimental.

The change of the contact angle at the condensation interface ( $\theta$ , Figure 23c) is essential in condensate propagation kinetics, as it affects both capillary condensation and capillary filling and can be determined directly from the main radii of the condensation interface ( $R_I$ ). Within the first  $\sim 20$   $\mu\text{m}$  of condensate length, the contact angle at the condensation interface ( $\theta$ ) increases rapidly from zero to  $\sim 97$  % of the equilibrium value predicted through the Kelvin equation (Figure 23f). Within this region, condensate growth is strongly affected by the capillary condensation, as the accumulation rate of n-propane molecules is governed by the radius of the condensation interface ( $R_I$ ), which changes rapidly with  $\theta$  changing. However, beyond the first  $\sim 20$   $\mu\text{m}$  of condensate length, the contact angle changes little ( $< 3$  %), the molecular accumulation rate for capillary condensation becomes approximately constant, and the condensate growth rate depends chiefly on capillary filling.

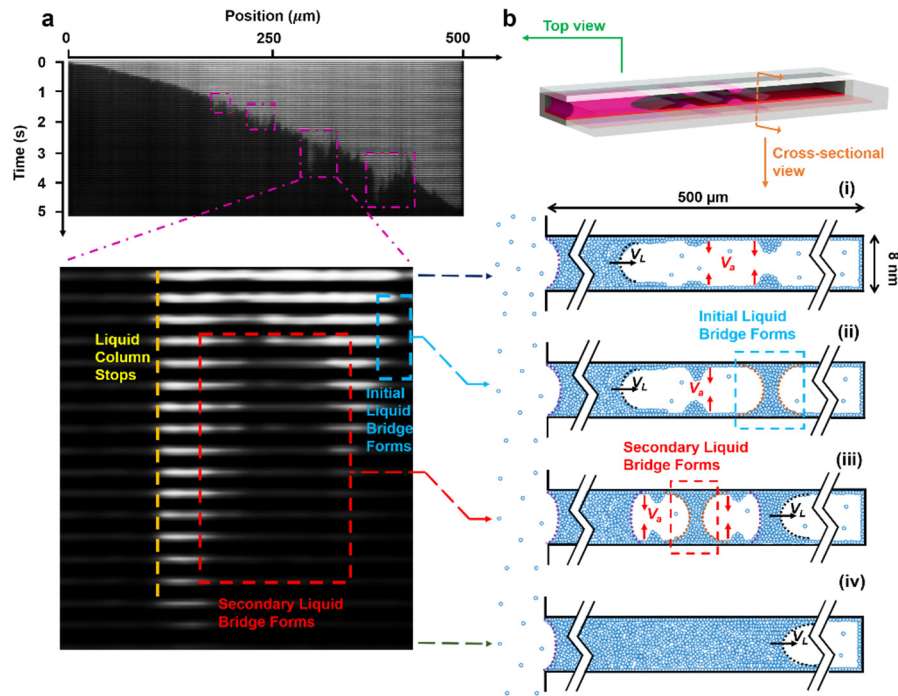


Figure 24 Observation of liquid bridging, nanobubble formation and nanobubble collapse during condensation at the sub-10 nm scale. (a) Condensate growth at 284.15 K and 0.61 MPa (shown in one channel imaged over time, where liquid bridging was observed). Images were stretched horizontally by a factor of 2.5 and contrast-enhanced in black and white for clarity. The enlarged image shows the details of the liquid bridging phenomena, where liquid column growth stops and an initial liquid bridge forms immediately, followed by secondary liquid bridge formation and nanobubble collapse. (b) Schematic of continuous and discontinuous condensate growth as a result of the growth of the liquid column ( $V_L$ ) and growth of adsorbed layers ( $V_a$ ) on the solid surface, (i). Discontinuous condensation occurs in an 8-nm channel when subcooling is low, leading to  $V_a > V_L$ . An initial liquid bridge forms and a nanobubble (main radii within nanoscale) is trapped, (ii). Secondary liquid bridge forms as a result of adsorption at a pressure above the Kelvin pressure, (iii). Nanobubble collapses as a result of liquid bridge formation at multiple locations within, (iv).

For low subcool conditions, bridging effects were observed in addition to continuous condensate growth (Figure 24a). Liquid bridging during condensation has been reported at the  $\sim 100$  nm scale previously, where the liquid bridge formed at relatively high subcool conditions as a result of capillary pressure-driven flow. However, at the sub-10 nm scale, multi-liquid-bridging was observed at low subcool. This result cannot be explained through similar condensate growth theory developed for  $\sim 100$  nm confinement or larger systems. Figure 14b shows a series of schematics illustrating the mechanisms behind this phenomenon. At any given condition above the Kelvin pressure, two liquid formation mechanisms act within the nanochannel: the propagation of the liquid column as a result of both capillary condensation and capillary filling ( $V_L$ , shown in Figure 21b (i)), and the molecular adsorption on the solid surface ( $V_a$ , shown in Figure 24b (i)). When subcool is high (e.g., 2.3 K at 282.15 K/0.61 MPa),  $V_L$  is much larger than  $V_a$ , which results in continuous condensate growth (Figure 13b). When subcool is low (e.g., 0.3 K at 284.15 K/0.61 MPa),  $V_L$  is reduced significantly (here by a factor of  $\sim 10$  based on both experimental observations

and model predictions), while  $V_a$  will remain largely unchanged (only proportional to saturation ratio, here from 1.032 to 1.008). In addition,  $V_L$  will decrease with the condensate length increasing (Figure 23a). As a result, liquid bridging is most likely to happen at low subcool and at long liquid column conditions, as observed here (Figure 24a). Once the initial liquid bridge forms (Figure 24b (ii)), the vapor pressure in the resulting nanobubble will be above the Kelvin pressure due to the pinned interface, resulting in internal adsorption and condensation. Fast adsorption and condensation within the nanobubble can lead to secondary liquid bridging (Figure 24b (iii)), repeating until nanobubble collapse (Figure 24b (iv)). These experimental results shed new light on liquid bridging phenomena at the sub-10 nm scale and provide direct support for the predictions of previous simulations.

### Component 3: Single component hydrocarbon bubble nucleation in 1-D sub-100 nm channels

The superheating and cavitation measurements along with the saturation curve are shown in the phase diagram of propane in Figure 25. The dependence of the cavitation pressure on liquid phase temperature has been obtained. The values of  $\Delta T_{\text{sup}}$  (superheat) and  $\Delta P_{\text{cav}}$  (cavitation pressure) decrease as the experimental condition moves toward the critical point of propane. The maximum value of the superheat measured in the experiments is  $\Delta T_{\text{sup}} = 31.6$  K at liquid pressure  $P_l = 1.30$  MPa. Similarly, the maximum value of cavitation pressure in the experiments is  $\Delta P_{\text{cav}} = 1.26$  MPa at  $T_l = 342.4$  K. Each measurement point in Figure 25 is a result of the average of at least three independent, repeated cavitation-experiments in two separate micro/nanofluidic chips.

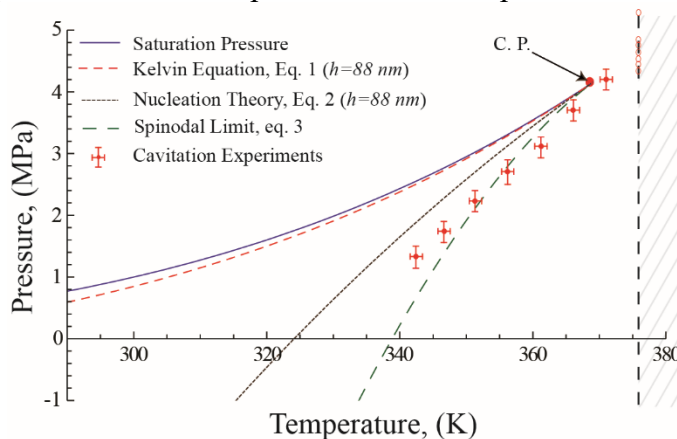


Figure 25 Measurements of bubble nucleation in 88-nm deep nanochannels. Plotted for comparison are the saturation vapor pressure, capillary pressure calculated from the Kelvin Equation, the prediction from the classical nucleation theory, and the spinodal limit.

As shown in Figure 25, the Kelvin saturation line corresponds closely to the bulk propane saturation line – indicating that the minimum superheating condition in the 88-nm channel is not significantly influenced by the channel dimensions. In general, for a liquid that completely wets a solid substrate such as propane (contact angle  $\sim 0$ ), nucleation is expected to occur slightly below the homogeneous nucleation theory prediction (less superheat). The early onset of nucleation was attributed to surface roughness and wetting characteristics. However, our results demonstrate a

delayed bubble nucleation in nanochannels that is shifted beyond the classical homogeneous nucleation prediction. The maximum deviation is  $\sim 4$  K and this deviation decreases as the experimental conditions approach the critical point. This deviation is not the result of roughness and is attributed to nanoconfinement.

As shown in Figure 25, three of seven nucleation measurements lay between the prediction from the classical nucleation theory and the spinodal limit, while four of them exceed the spinodal limit. Although the shift in critical point is not the main focus of this work, we continued the isothermal nucleation experiment by increasing the temperature beyond the critical point with the similar step size in temperature. The difference of the reflective light intensity between vapor and liquid decreased as the measurements moved towards the critical point. At  $375.9 \pm 1$  K no liquid to vapor phase transition was observed (vertical). The last detected nucleation point ( $T_l = 371.0 \pm 1$  K) is only  $\sim 1.3 \pm 1$  K higher than the critical point (369.7 K). Thus while the nucleation experiments here demonstrate significant shift from classical nucleation theory, no significant critical point shift was detected.

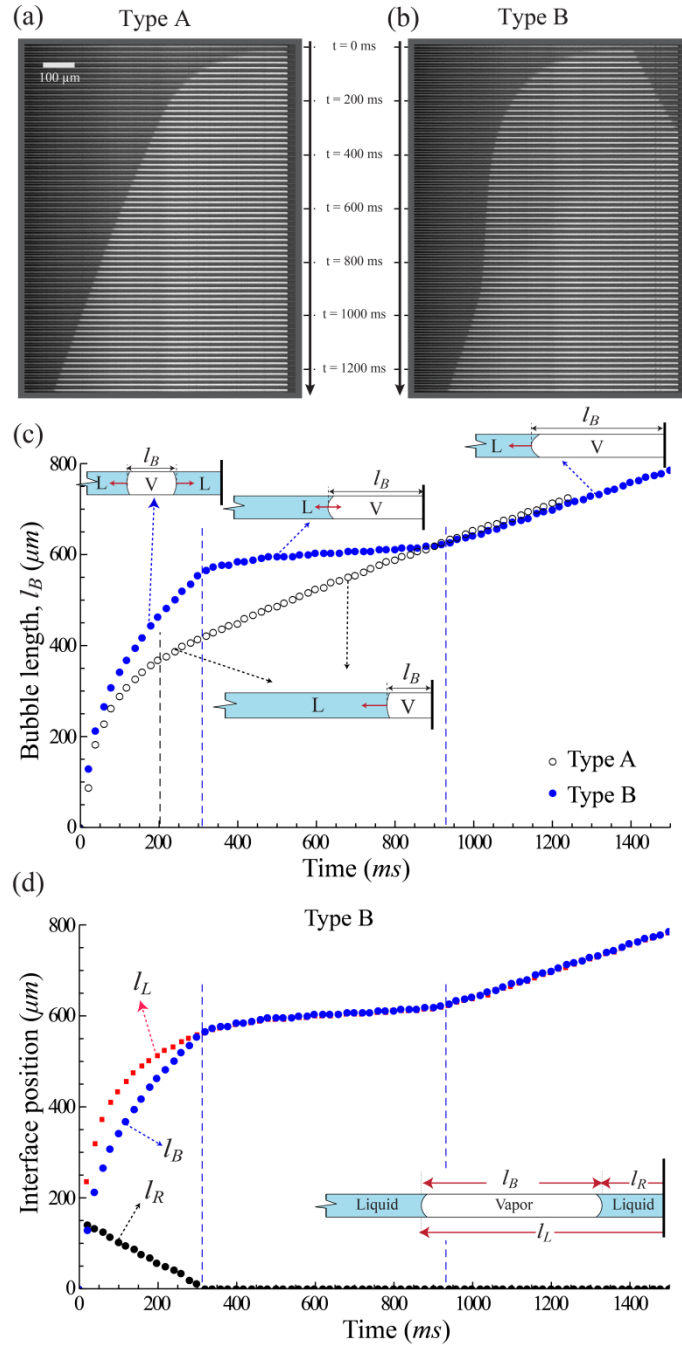


Figure 26 Mechanisms of bubble column growth at  $T_I = 346.3$  K and  $P_I = 1.60$  MPa: a) Image sequence of Type A growth where vapor bubble nucleates at channel-end; b) Image sequence of Type B where vapor bubble nucleates along the channel; c) Bubble length  $l_B$  versus time of Type A and B growth; d) Positions of left and right liquid-vapor interfaces,  $l_L$  and  $l_R$ , of Type B growth. Following nucleation of a vapor bubble, a vapor column grows in the nanochannels. In all the cavitation tests, we observed two types of bubble column growth mechanisms according to the location of bubble nucleation: Type A where the bubble nucleates at channel-end, and Type B where the bubble nucleates along the channel.

As shown in Figure 26, Type A growth experiences two regimes, namely “transient start-up” and “steady linear growth”. In contrast, the Type B growth curve presents three different regimes, namely “transient start-up”, “transitional” and “steady linear growth” regimes, as shown in Figure 26C. In the Type B growth, both the right and left interface movement contribute to the vapor bubble column growth, as shown in Figure 26D. Surprisingly, for each of the nucleation conditions, the bubble growth curves converge eventually in steady linear growth regime regardless of type or initial nucleation location.

The calculated  $P_v$  in the steady linear growth regime is found to be  $\sim 14\%$  on average lower than  $P_{sat}$  at different nucleation conditions: 14% (342.4 K), 10% (346.3 K), 13% (351.3 K), 17% (356.2 K), and 14% (361.2 K). The somewhat lower prediction of pressure ( $P_v$ ) is an indication of higher viscous friction in the nanochannels as compared to the theoretical value. In general, this phenomenon has been attributed by others to surface roughness, the presence of bubbles, and/or the formation of highly viscous layers near the interface.

#### Component 4: Mixture hydrocarbon phase behavior at a mixed nano-macro length scale

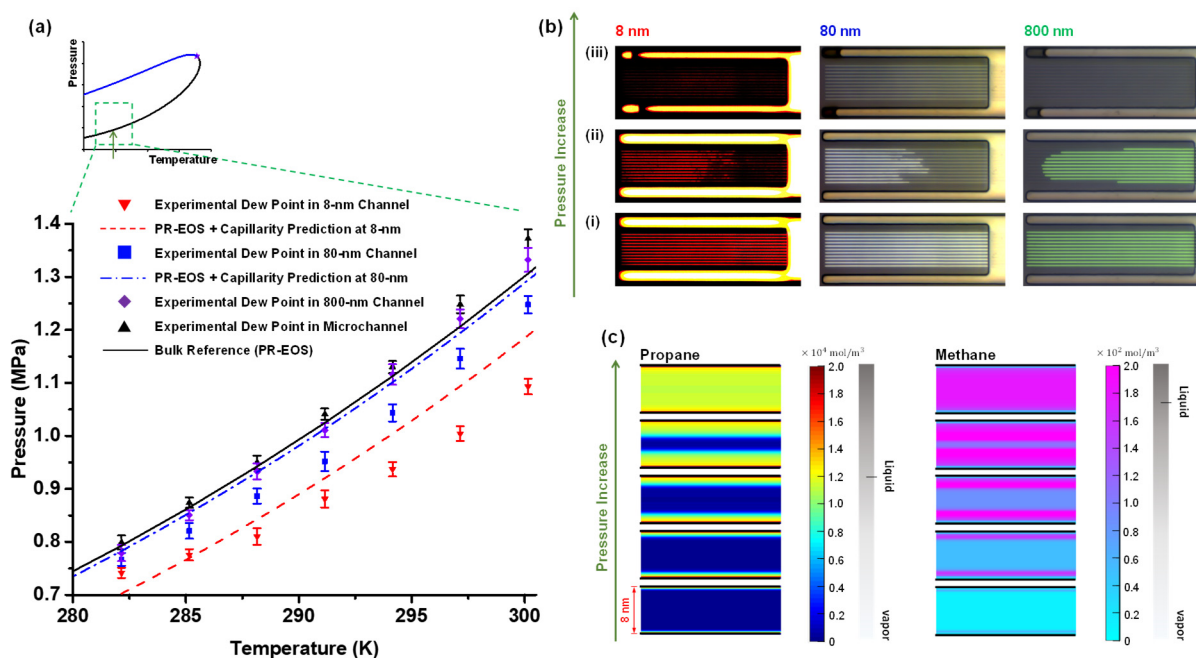


Figure 27 Early condensation of a methane/propane mixture (1:4 overall mole ratio) in nanoconfinement compared to bulk. (a) Dew point data detected in 8-nm, 80-nm, 800-nm and microchannel (bulk), where condensation occurs earlier (at lower pressures) as channel size decreases. The experimental results show a larger shift (lower pressures) than predicted by theory based on capillary condensation alone. Each point represents the average of a total of 33 measurements (3 runs with 11 nanochannels). (b) Representative images of early condensation observed at the three different lengthscales, at 288.15 K: i, vapor phase observed throughout at low pressure; ii, early condensation in nanochannel with liquid (the darker phase) initiating from the inlet in both 8-nm and 80-nm cases, while from the dead-end in 800-nm; and iii, condensation

observed in microchannel. (c) DFT calculation results of propane and methane molecules accumulating in 8-nm channel with pressure increasing.

To test the effect of nanoconfinement on the mixture dew point (i.e., pressure and temperature of liquid phase first formed in pure gas phase), we directly measured the initiation of condensation in nanochannels at different isothermal conditions (ranging from 282.15 to 300.15 K). By injecting premixed gas-phase hydrocarbon mixtures into the system and increasing the system pressure stepwise at isothermal condition, we were able to identify the condensation initiation conditions (Figure 27a) at different scales of nanoconfinement directly through real-time optical images (Figure 27b). The liquid was formed first at the entrance of the nanochannels in the 8- and 80-nm cases, but at the opposite (deadend) in the 800-nm and microchannel cases. This effect is due to the size-dependent competition between vapor adsorption and vapor transport, in agreement with previous results.

The measured initiation pressure was further compared to the Peng-Robinson equation of state (PR-EOS) with capillary pressure model – widely used to predict the hydrocarbon mixture phase behavior at nanoscales<sup>18</sup>. Both the experiment and theory show the condensation pressures at the nanoscale ( $P_{dew}^{nano}$ ) below the bulk dew point ( $P_{dew}^{bulk}$ ). However, the theory generally underestimates the shift in small channels (8-nm and 80-nm, Figure 27a), compared to experiments. The EOS model includes powerful capillarity effects, but cannot account for compositional changes expected in multi-component, nanoconfined systems.

To better understand the effect of nanoconfinement on hydrocarbon mixture condensation, we performed density functional theory (DFT) calculations for the 8-nm case at 288.15 K. Within the framework of DFT<sup>43</sup>, the chemical potentials of species in the nanochannel are identical to those in the microchannel, and those obtained from the PR-EOS. As shown in Figure 27c, when system pressure is low, both propane and methane form adsorption layers on the solid surface. However, due to a stronger Van der Waals interaction between the propane molecule and solid channel surface, propane is the dominant adsorbed species, by two orders of magnitude. As the system pressure increases, the adsorption layers grow continuously, and the middle of the pores contain a vapor mixture of propane and methane similar to the bulk. At  $P_{dew}^{nano}$ , the average density of propane and methane in the middle of the pores suddenly increases from vapor- to liquid-like, where the average propane/methane mole ratio has a value of 77. At the same temperature, the propane/methane mole ratio in bulk liquid phase at  $P_{dew}^{bulk}$  is only 68. The fraction of the heavier component in the nanoconfined liquid phase is 13% higher than bulk liquid due to the stronger surface adsorption of propane and the large surface to volume ratio in nanochannel. This compositional shift to the heavier components is expected to lead to a further reduction of the dew point in connected nanochannels, in addition to capillarity effects included in the PR-EOS results (Figure 27a). For example, the composition change in the 8-nm channel at 288.15 K here led to the dew point reduction of 0.029 MPa (difference between the experimentally measured dew point and the PR-EOS + Capillarity model prediction). This reduction in dew point pressure is on the order of that expected in bulk, with a compositional shift of the magnitude predicted by the DFT simulations. The deviation is also a significant 21% of the total deviation from bulk to nano dew point (i.e.,  $P_{dew}^{bulk} - P_{dew}^{nano}$ , Figure 27a) at this temperature. At higher temperatures, this deviation increases further with increasing adsorption selectivity of the heavy component on the nanochannel surface (e.g., ~43% at 300.15 K, Figure 27a).

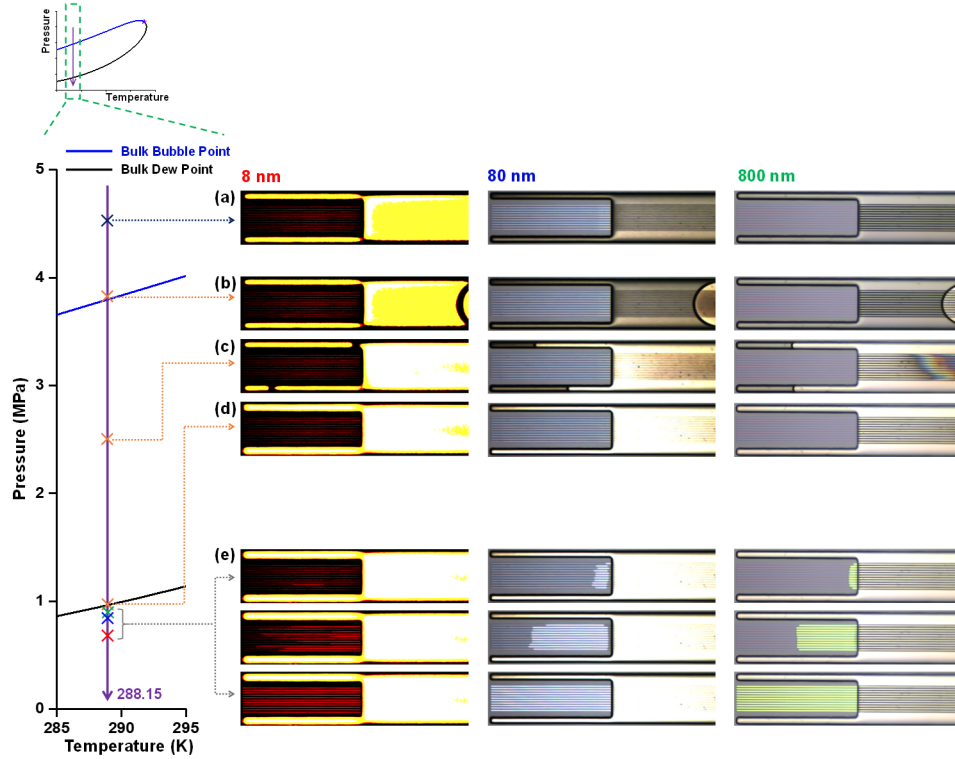


Figure 28 Vaporization of the methane/propane mixture (1:4 overall mole ratio) in nanoconfinement comparing to bulk in an isothermal (288.15 K) near-equilibrium pressure drawdown process. (a) Initial liquid phase throughout at  $P = 4.50$  MPa. (b) Vaporization happens in microchannel at  $3.82 \pm 0.11$  MPa. (c) Liquid-vapor condition reaches equilibrium in microchannel at 2.50 MPa. (d) Mixture fully vaporizes in the microchannel at  $0.93 \pm 0.07$  MPa. (e) Mixture vaporization in the nanochannel through cavitation/evaporation. In all cases (8-nm, 80-nm and 800-nm), vaporization of mixture in nanochannel only happens below bulk dew point, and vaporization pressure decreases with nanochannel size ( $0.72 \pm 0.03$  MPa,  $0.84 \pm 0.04$  MPa,  $0.88 \pm 0.02$  MPa). Cavitation also dominates evaporation as channel dimension decreases. Each point here represents the average of a total of 33 measurements (3 runs with 11 nanochannels).

To study the mixture bubble point (i.e., pressure and temperature of gas phase first formed in pure liquid phase) in connected nanochannels, we performed a near-equilibrium pressure drawdown similar to *in-situ* shale oil production (Figure 28). Initially the whole system was in liquid phase ( $P = 4.50$  MPa, above theoretical bulk bubble point  $P_{bubble}^{bulk} = 3.77$  MPa at 288.15 K based on the PR-EOS). When system pressure was slowly reduced to a value (3.82 MPa), close to  $P_{bubble}^{bulk}$ , cavitation initiates first in the microchannel (Figure 28a, b). Further reducing the system pressure led to the vapor phase growing into the two control microchannels (Figure 28c). Complete vaporization of mixtures in the microchannel (Figure 28d) took place at a pressure (0.93 MPa) close to the theoretical bulk lower dew point ( $P_{dew}^{bulk} = 0.94$  MPa, based on the PR-EOS). However, in all three cases, the liquid phase in the nanochannel remained throughout the process without bubble formation or detectable evaporation. To vaporize the liquid phase confined in the nanochannel, the system pressure needed to be reduced further, below the bulk dew point for the mixture,  $P_{dew}^{bulk}$ . The effective bubble point in the nanochannels,  $P_{bubble}^{nano}$ , decreased as channel size decreased (0.72 MPa in 8-nm channel, 0.84 MPa in 80-nm channel and 0.88 MPa in 800-nm channel). Furthermore, the liquid and vapor phase did not exist in equilibrium in the nanochannel,

as is typical of mixtures at larger scales. Rather, vaporization took place effectively instantly and in full, once pressure reduced to  $P_{bubble}^{nano}$ . In this regard, the effective phase diagram for hydrocarbon mixtures in connected nanopores contains no bubble point in the traditional sense, and rather exhibits a phase diagram without an appreciable two-phase envelope, more akin to pure substances.

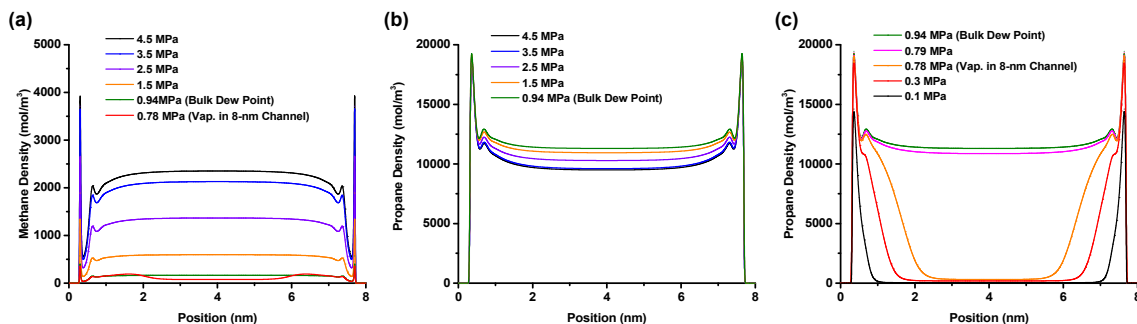


Figure 29 DFT simulation results for molar density distributions of propane and methane in the 8-nm channel during the near-equilibrium isothermal (288.15 K) pressure drawdown. (a) During pressure drawdown, the average density of methane decreases continuously. (b) When system pressure is below the bulk bubble point (3.77 MPa), the average density of propane molecules in the nanochannel increases with decreasing pressure, reaching a maximum at the bulk dew point (0.94 MPa). (c) Further reducing system pressure below the bulk dew point, the average density of propane starts to slowly decrease. At certain threshold (0.78 MPa), a significant reduction of propane density occurs, predicting vaporization in the 8-nm channel.

We employed DFT to calculate the density distributions in the 8-nm channel in the near-equilibrium pressure drawdown case at 288.15 K. The model effectively captures the influence of the mixture of lengthscales (nanopores connected to bulk volumes) by assuming a semi-infinite slit pore geometry of the nanochannel in equilibrium with a microchannel (bulk). As shown in Figure 29a, during the pressure drawdown from 4.5 MPa to  $P_{dew}^{bulk}$  (0.94 MPa), the lighter component (methane) is continuously released from the nanochannel. The methane is replaced by propane due to the preferential adsorption of the heavier component as well as evaporation in the microchannel enriching the concentration of propane in the liquid phase. As a result, the average density of propane in the nanochannel slowly increases (Figure 29b), and the hydrocarbon mixture confined in nanochannel becomes denser as pressure declines to  $P_{dew}^{bulk}$ . Further reducing the system pressure leads to slow release of propane molecules (Figure 29c). At  $P_{bubble}^{nano}$  (0.78 MPa from DFT calculation on the point of equilibrium transition), the average density of propane molecules in the nanochannel suddenly drops, predicting capillary evaporation/cavitation of hydrocarbon mixtures under nanoconfinement. The DFT approach further predicts  $P_{bubble}^{nano}$  is even lower than  $P_{dew}^{nano}$  due to hysteresis, as also been observed in our experiments.

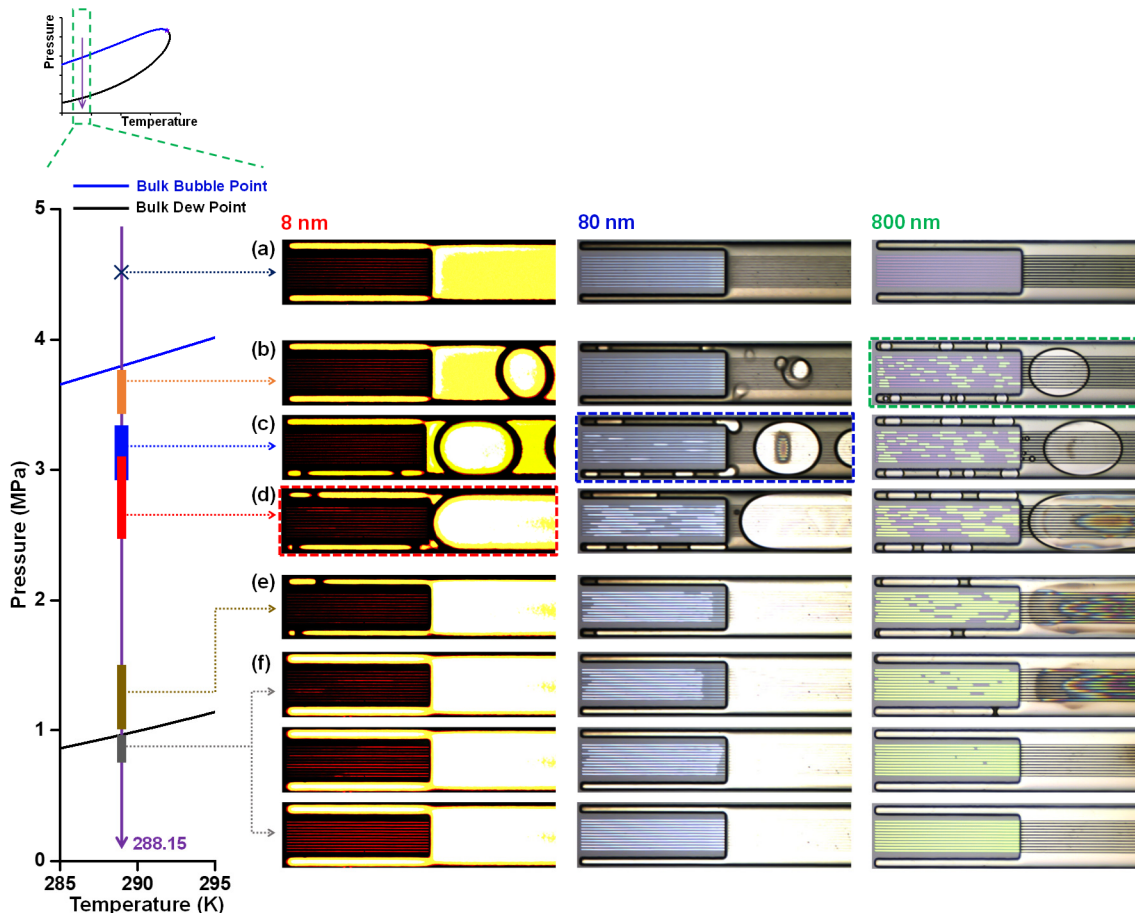


Figure 30 Non-equilibrium, fast pressure drawdown vaporization process for the hydrocarbon mixture in nanoconfinement compared to bulk, at isothermal conditions (288.15 K). (a) Initial liquid phase at 4.5 MPa. (b) Vaporization occurs in the microchannel and 800-nm channel in the range of 3.4 to 3.7 MPa. (c) Cavitation initiates in 80-nm channel in the range of 2.8 to 3.3 MPa, and (d) in 8-nm channel in the range of 2.4 to 3.1 MPa. (e) Further reducing the pressure, the bubble in the 8-nm channel collapses while bubbles in the 80-nm and 800-nm channels grow. (f) Secondary vaporization in the 8-nm channel and fully vaporization of mixture in 80-nm and 800-nm channel (0.7 to 0.9 MPa). These results are from a total of 33 measurements (3 runs with 11 nanochannels).

The effect of the exchange of mixture components between bulk volumes and connected nanopores, can be assessed experimentally by limiting the time available for the molecular exchange. Our experimental system readily permits the study of a rapid, non-equilibrium pressure drawdown process for comparison. Specifically, the near-equilibrium test indicated that both a preferentially adsorbed heavy fraction into the nanopores, and an exchange of light components with connected bulk volumes resulted in strongly deviated phase behavior (effective bubble point below the bulk dew point in nanoconfined mixtures). Here we depressurize at a rate that is an order of magnitude faster than that required to approach equilibrium concentrations in the nanochannel, effectively isolating the nanopore from the surrounding larger connected structures.

To perform the non-equilibrium process, we reduced the system pressure through fast volume expansion. As shown in Figure 30, the observed phase behavior in this case is markedly different from that in the near-equilibrium pressure drawdown process. Initially the system temperature and pressure were set at 288.15 K and 4.5 MPa (Figure 30a). When the pressure dropped below  $P_{bub}^{bulk}$  (here ranging 3.4 to 3.7 MPa < 3.77 MPa), cavitation initiated in the microchannel, as well as in the 800-nm channel (Figure 30b). By further reducing the pressure, cavitation also initiated in the 80-nm (2.8 to 3.5 MPa, Figure 30c) and the 8-nm channels (ranging from 2.4 to 3.1 MPa, Figure 5d). In stark contrast with the near-equilibrium test results, all three channel sizes produced bubbles at conditions within the classical two-phase envelop. Following formation, behavior of the entrapped bubbles was nanochannel size-dependent. For the 800-nm and 80-nm channels, the bubble grew continuously with decreasing pressure, and eventually expanded to fill the nanochannel (Figure 30e, f). In the 8-nm channel (Figure 30e, f), the bubble first collapsed, and did not regenerate until the system pressure dropped below  $P_{dew}^{bulk}$  (0.7 to 0.9 MPa).

The differences between the dynamics of vaporization in the 8-nm vs. the 80- and 800-nm channels is attributed to the influence of the thermodynamic equilibrium bubble radii inherent to mixtures. Specifically, bulk fluid mixtures exhibit an unstable equilibrium bubble radius ( $R_e$ ) and a stable equilibrium bubble radius ( $R_E$ ,  $R_e < R_E$ ) as thermodynamic properties. An initially triggered bubble in the mixture needs to be larger than  $R_e$  to grow to  $R_E$ , otherwise the bubble will collapse. The specific values of  $R_e$  and  $R_E$  are in general a complex function of the mixture components and are further influenced by surface effects particularly in confined geometries. However, for the hydrocarbon mixture here an  $R_e$  value on the order of a few nanometer is expected based on homogenous nucleation theory, while  $R_E$  is experimentally shown here to be at the microscale. With equilibrium radii on these scales, it is expected that the initial bubble radius in the 8-nm channel was smaller than  $R_e$  and thus unstable, while the bubble radius in the larger nanochannels exceeded  $R_e$ , and thus grew continuously (Figure 30f).

In summary, the rapid depressurization tests here effectively isolate the nanochannels from the larger connected volumes. The resulting vaporization occurred much earlier in these cases as compared to the near-equilibrium tests in which the nanochannel mixture was in full communication with the larger volume ( $\sim 3$  MPa vs.  $\sim 1$  MPa). These results highlight the dramatic role of the exchange of mixture components between the nanochannels and larger connected volumes in lowering the effective bubble point.

### **Component 5: Single component hydrocarbon evaporation in 2-D sub-10 nm nanogrids**

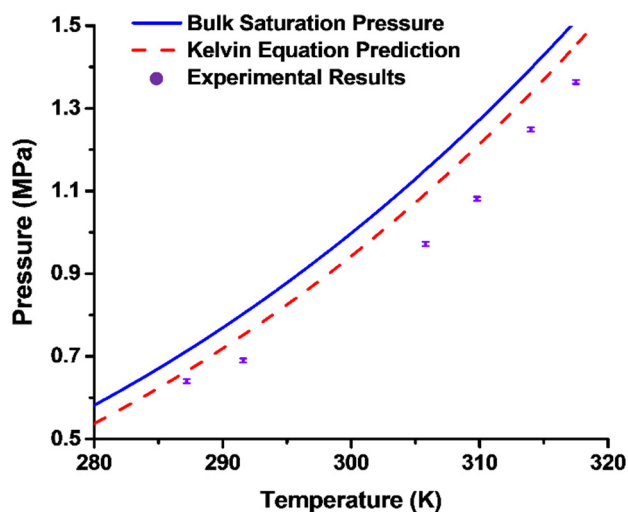


Figure 31 Onset of evaporation in the 2D nanoporous media compared to the bulk saturation pressure (from NIST) and the capillary pressure as determined through the Kelvin equation for the 2D nanoporous media geometry. Each experimental data point is an average of three separate experiments. Error bars represent the maximum pressure variation observed between fluctuation of pump and error among three replicates ( $\pm 0.005$  MPa).

Propane was injected in liquid phase and pressures were lowered to below the saturation pressure of propane to observe evaporation. Once the pressure was lowered below the saturation pressure, the liquid in the bulk reservoir evaporated almost instantaneously. The onset of evaporation was measured under isothermal conditions with temperature ranging from 287.2 K to 317.5 K and results are shown in Figure 31. For reference, Figure 31 also shows both the saturation pressure for bulk (from NIST) and the Kelvin equation predictions for the experimental nanopore geometry. The deviation from the pressure predicted by the Kelvin equation ranged from 3.3% to 11.1%.

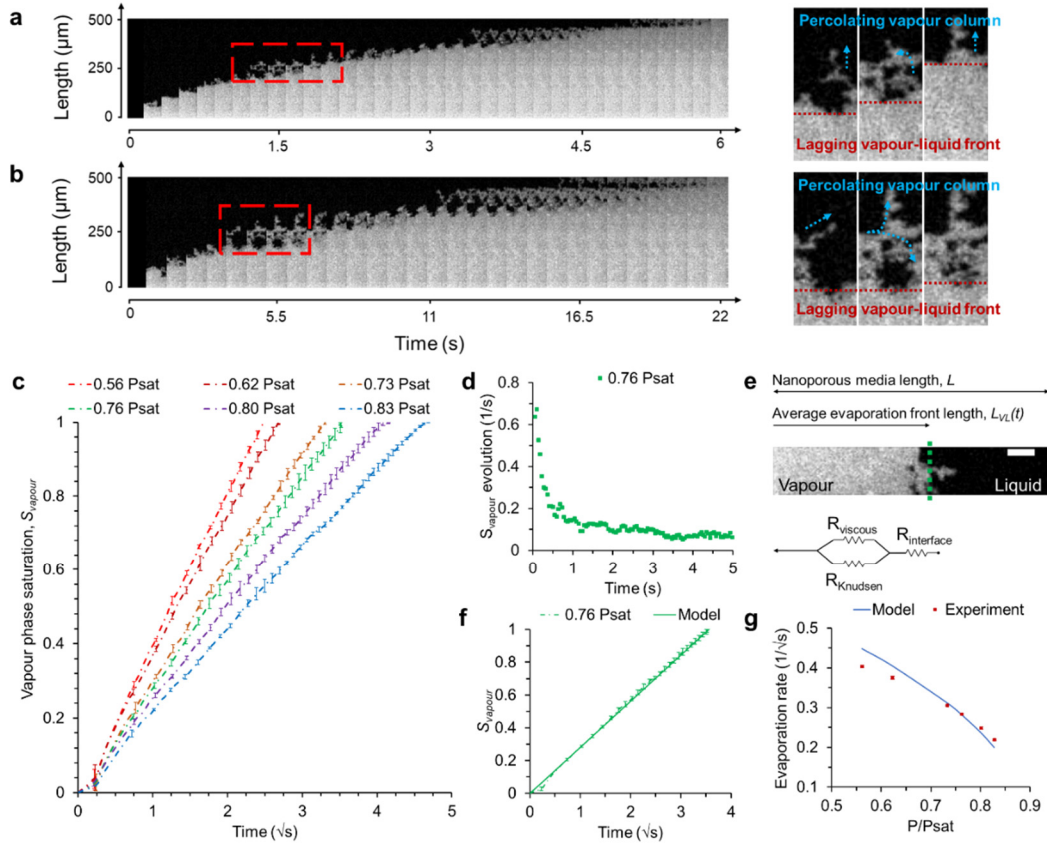


Figure 32 Evaporation dynamics and model at 287.2 K ( $P_{sat} = 0.716$  MPa) (a) Time-lapse sequence of evaporation at  $0.56 P_{sat}$  (0.402 MPa) and (b)  $0.83 P_{sat}$  (0.594 MPa). The images have been converted to grayscale and processed by subtracting the background and enhancing the contrast. Here, the vapour phase appears bright and the liquid phase appears dark. Only chosen frames are displayed for clarity. A zoom-in in (a) and (b) shown adjacent to respective panels highlighting the vapour phase percolation mechanism. (c) Vapour phase saturation ( $S_{vapour}$ ) evolution for six different target pressures plotted as a function of square root time (all experiments performed at 287.2 K). (d)  $S_{vapour}$  evolution as a function of time during the early stages of evaporation for the 0.76  $P_{sat}$  case. (e) Resistance model considering vapour mass transport and evaporation at the liquid-vapour interface. Vapour phase saturation is determined by taking the ratio of the calculated evaporation front length ( $L_{VL}$ ), and the nanoporous media length ( $L$ ). Scale bar represents 50  $\mu\text{m}$  (f) Example of model predictions compared to experimental results at 0.76  $P_{sat}$  (g) Comparison of evaporation rates calculated from model to experimental data. Error bars in (c), (e) and (f) represent standard deviation from three repeated experiments performed on two different nanoporous media each (six replicates). Only representative standard deviation errors bars are shown in (c).

To study the evaporation dynamics, experiments were conducted for different conditions at 287.2 K and six different drawdown pressures (ranging from  $0.56 P_{sat}$  to  $0.83 P_{sat}$ ). Figure 32 a and b show time-lapse sequence of evaporation images obtained with high superheat ( $0.56 P_{sat}$ ) and low superheat ( $0.83 P_{sat}$ ). The evaporation front is more uniform in the case of high superheat. Figure 32c shows the vapour phase saturation ( $S_{vapour}$ ) evolution over time at different target pressures.

The vapour phase saturation for all runs show a square-root-of-time dependence. The  $S_{vapour}$  evolution falls drastically within the first second of evaporation and then plateaus as shown for the  $0.76 P_{sat}$  case in Figure 32d. To model the observed evaporation dynamics, we take into consideration vapour flow resistance and interfacial resistance and assume that the evaporation front ( $L_{VL}$ ) is uniform as shown in Figure 32e. Figure 32f compares the experimental result obtained for at  $0.76 P_{sat}$  with that predicted by the resistance model. Figure 32g shows a comparison for all experimental cases to model prediction (within  $\pm 10\%$  deviation). The vapour mass transport resistance significantly dominates the interfacial resistance, with almost equivalent contributions from the Knudsen flow resistance and viscous flow resistance.

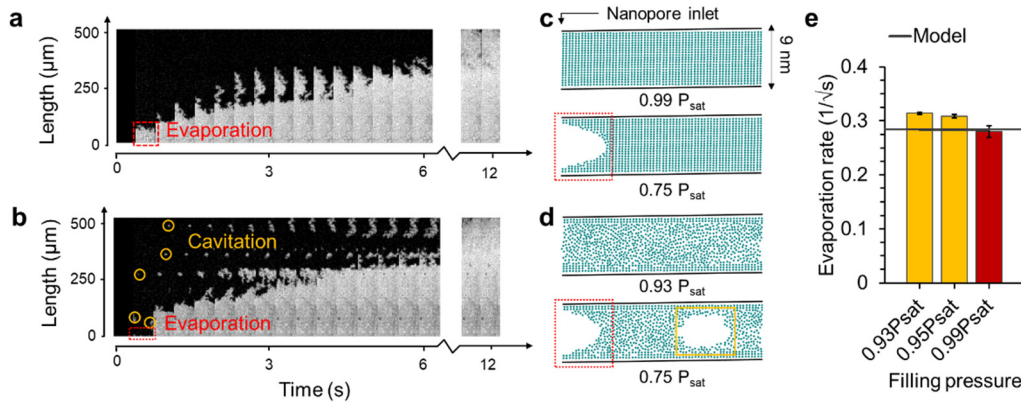


Figure 33 Evaporation mechanisms induced by initial loading pressures in the capillary condensation regime. (a) Time-lapse sequence of continuous evaporation at filling pressures of  $0.99 P_{sat}$ . (b) Time-lapse sequence of discontinuous evaporation at filling pressures of  $0.93 P_{sat}$ . In both (a) and (b), the final pressure was reduced to  $0.75 P_{sat}$  to observe evaporation. (c) Cross-sectional schematic showing proposed mechanism via which continuous evaporation and (d) discontinuous evaporation proceed. The red box indicates evaporation from the inlet of the nanoporous media and yellow boxes indicate cavitation. (e) Comparison of evaporation rates at different loading pressures. Error bars represent standard deviation over three replicate experiments. Yellow bars indicate conditions that led to discontinuous evaporation and red bars indicates conditions that led to continuous evaporation. The horizontal black line shows the evaporation rate predicted by the resistance model for reference.

Additionally, a distinct form of liquid-to-vapour transition was observed when the initial liquid pressure was between the Kelvin equation predicted pressure and the bulk saturation pressure. The chip was loaded at three different initial saturation conditions ranging from  $0.93 P_{sat}$  to  $0.99 P_{sat}$  ( $P_{Kelvin} = 0.93 P_{sat}$ ) and pressure was reduced to a constant value of  $0.75 P_{sat}$  ( $T = 291.6 \text{ K}$ ). With initial liquid pressure close to bulk saturation pressure, smooth evaporation from the nanopore inlet was observed (“continuous evaporation”) as shown for the  $0.99 P_{sat}$  case in Figure 33a. At initial liquid pressures below bulk saturation, we observed nucleation of vapour bubbles along with evaporation from the inlet (“discontinuous evaporation”) as shown for the  $0.93 P_{sat}$  case in Figure 33b. With lower initial liquid pressures, we speculate that the liquid phase has a lower density of molecules and weaker structuring of molecules resulting in cavitation (especially in at sites with local height expansions or defects). This proposed mechanism is shown in Figure 33c

and d. Despite the two mechanisms we see that evaporation rates are comparable to each other and to the model as shown in Figure 33e (within  $\pm 10\%$  deviation).

### Component 6: 2-D nanogrids in screening enhanced tight oil recovery strategies

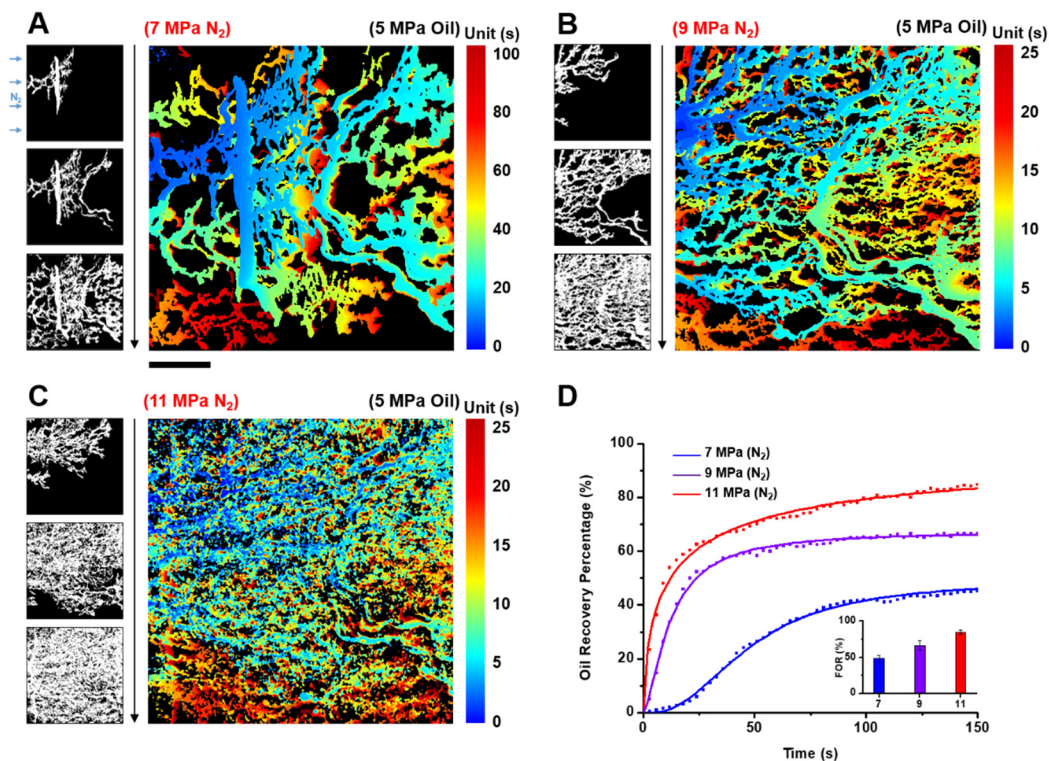


Figure 34 Nanomodel screening of immiscible N<sub>2</sub> flooding in tight oil reservoirs. (A)-(C) Oil recovery history of immiscible N<sub>2</sub> flooding at 7, 9 and 11 MPa. At test pressures below 7 MPa, the gas was prohibited from flooding the nanomodel due to capillary force. The scale bar represents 200  $\mu\text{m}$ . (D) Cumulative oil recovery changes with time. The inset figure shows the final oil recovery percentage (FOR) at different N<sub>2</sub> pressures. The error bar is from three independent nanoporous media. The oil reservoir pressure on chip was held constant at 5 MPa.

Nitrogen injection is an EOR strategy that is commonly applied in conventional reservoirs. Nitrogen is relatively low cost, non-corrosive and can provide excellent performance. For these same reasons, N<sub>2</sub> injection in nanoporous shale is of interest, but the performance, or potential, of N<sub>2</sub> injection in nanoconfinement is largely unknown. While the literature is scarce, Nitrogen pilots have been reported on wells in Appalachian basin where nitrogen gas is used as fracturing fluid with a report of 28% improvement in estimated ultimate recovery compared to a foam-based method. Here after filling the nanomodel with oil, the oil reservoir pressure was set at 5 MPa (simulating near-wellbore depleted reservoir pressure following primary recovery). N<sub>2</sub> was then injected at pressures ranging from 5 MPa to 11 MPa. The injection pressure was kept constant for the duration of each test, and tests were run at 5, 5.5, 6, 6.5, 7, 9, and 11 MPa. Due to a high N<sub>2</sub>-oil minimum miscibility pressure ( $\sim 40$  MPa), all N<sub>2</sub> experiments were *immiscible* floods, in keeping with the expected conditions for N<sub>2</sub> in many tight oil reservoirs (e.g. Bakken formation). The initiation of N<sub>2</sub> flooding happening first at 7 MPa, and no detectable N<sub>2</sub> flooding occurred in

lower pressure tests. With the oil side reservoir pressure maintained at 5 MPa, these results indicate a significant pressure difference threshold (2 MPa) required for immiscible flooding in nanoconfinement that has no analog in conventional, microporous reservoirs. This threshold is a product of the strong capillarity effects in nanoconfinement. From theory the capillary pressure generated at the N<sub>2</sub>-oil interface is predicted to be ~1.4 MPa. When the pressure difference between N<sub>2</sub> and oil is below this threshold, the system simply reaches a pressure equilibrium at the liquid-gas interface, that is, the fracture-nanoporous media interface. This pressure requirement is a barrier to injection and ultimately recovery in these systems. While in conventional reservoirs, the pore size is at the micrometer or even millimeter scale, and thus the capillary force is reduced by more than 1000 times (~ 1 kPa), and is thus negligible in the context of injection pressures and viscous pressure drops in conventional operations.

Figure 34A-C presents the composite spatio-temporal advancement of nitrogen into the oil phase with the color bands showing relative timing during the injection process (that is, the color reflects the first instant that a given pore was cleared), at 7, 9 and 11 MPa. For clarity, greyscale image sequences are provided in each case at left (Figure 34A-C). At these injection conditions the N<sub>2</sub>-oil systems exhibited capillary fingering behavior reflective of the low Ca (~10<sup>-5</sup>), high mobility ratio (~10<sup>2</sup>) zone in the Lenormand phase diagram. As the gas pressure was increased from 7 to 11 MPa, the gas fingers become smaller and exhibit a higher spatial density leading to higher recovery in keeping with the classical theory. While the fingering effect is an inherent limitation in immiscible flooding, increasing the injection pressure can improve EOR productivity in nanoconfinement. In this test, the ultimate oil recovery in the nanomodel increases from 48% to 86% by increasing the injection pressure from 7 to 11 MPa (Figure 34D).

In terms of operations, these immiscible N<sub>2</sub> flooding results offer some insights. While it is typical for micro- and nanomodel results to overestimate recovery in general, the difference here in the side-by-side comparison of nanomodels indicates the significance of the initial gas pressure on the performance of immiscible gas flooding in nanoporous systems. The nanomodel results also clearly indicate limitations in terms of the ultimate applicability of immiscible EOR in shale. Specifically, the smaller pore throats in shale formations can be a few nanometers, in which case the capillary pressure influence observed here is expected to be further increased to tens of MPa. This pressure is on the same order as initial reservoir pressure and effectively prohibits immiscible gas access into these pores. Generating gas flow in nanoporous media already introduces significant viscous pressure drop (scaling with the square of pore size), and the additional overhead of significant capillary pressure is likely to make immiscible gas flooding impractical for most shale reservoirs.

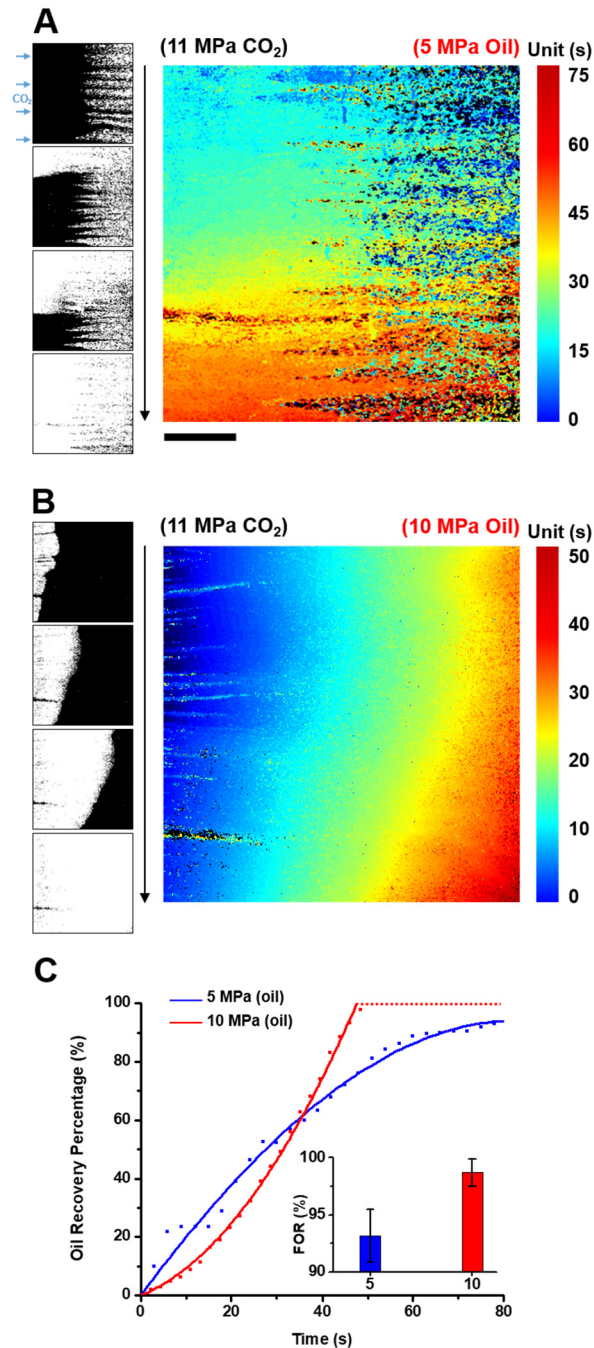


Figure 35 Screening conditions for miscible gas flooding (11 MPa CO<sub>2</sub>) in a shale/tight oil reservoir at 323 K, and (A) relatively low pressure reservoir (5 MPa) and (B) high pressure reservoir (10 MPa). The scale bar represents 200  $\mu\text{m}$ . (C) Cumulative oil recovery plotted vs. time. The inset figure shows the final oil recovery percentage (FOR) at different reservoir pressures. The error bar is from three independent nanoporous media.

CO<sub>2</sub> is another injection gas candidate for enhanced oil recovery. EOR using CO<sub>2</sub> can not only improve oil recovery efficiency, but can also serve a carbon storage goal. CO<sub>2</sub> flooding is widely

applied in conventional medium to heavy oil reservoirs, and has recently been piloted in the Jilin tight Oil field (China), with reports of oil recovery factor increasing 4.5 % with 0.26 million tons of CO<sub>2</sub> been injected underground after 6 years of operation<sup>38</sup>. Compared to nitrogen, the minimum miscibility pressure of CO<sub>2</sub> in light oil is significantly lower due to light component extraction from the oil into CO<sub>2</sub> at relatively low pressures. The minimum miscibility pressure of CO<sub>2</sub> with the light oil in this study (i.e., West Texas crude) at 323 K was determined to be ~10 MPa. Here, we found the minimum miscibility pressure in the nanomodel to approximate this bulk value. The miscible CO<sub>2</sub> flooding experiments were conducted under two conditions, at (i) low initial oil pressure well below the minimum miscibility pressure (5 MPa), and (ii) high initial oil pressure where CO<sub>2</sub>-oil miscibility is expected (10 MPa). These two cases simulate EOR in shale formations with low and high reservoir pressures, respectively. The CO<sub>2</sub> was injected at 11 MPa to maintain initial miscible flooding conditions for both cases.

The spatio-temporal advancement of the CO<sub>2</sub> phase into the oil for both the low and high initial reservoir pressures is shown in Figure 35A and B, respectively. For the low reservoir pressure case (5 MPa), oil displacement was first observed as gas break-out close to the oil reservoir side (right). A significant film-wise displacement followed, (i.e., miscible flooding) initiating from the gas channel (left), ultimately resulting in a clean sweep of the trapped oil in the nanoporous media. This early gas break-out is attributed to a change in miscibility conditions across the nanomodel. Specifically, on the injection side CO<sub>2</sub> is miscible with the oil phase and enters readily, however, as the CO<sub>2</sub> migrates across the nanomodel, the local pressure drops below the minimum miscibility pressure (~10 MPa) and CO<sub>2</sub> gas emerges as a distinct phase. The strong capillary forces surrounding the gas phase (noted earlier as a significant flooding barrier) serve a powerful recovery role here, when generated within the nanoporous media. The overall flooding result in terms of oil recovery percentage (93%, Figure 35C) is notably better than that in the immiscible N<sub>2</sub> flooding case (86%), under the same gas pressure condition (11 MPa).

Relating these results to nanoporous tight oil and shale reservoirs, the gas break-out mechanism observed here (Figure 15A) can also be expected if minimum miscibility pressure is between the injecting CO<sub>2</sub> pressure and that of the reservoir. The diffusion length of CO<sub>2</sub> into the tight oil reservoir is longer than the displacement CO<sub>2</sub>-oil film front within the first few months of the production period (due to the extreme low permeability of shale hindering the pressure driven film-wise displacement). In this scenario, CO<sub>2</sub> diffused deeply into the reservoir, far away from the film front, can exceed solubility locally. Gas phase can then break out into fingers as observed here, providing additional oil recovery through a mechanism akin to local immiscible flooding but without the initial capillary pressure barrier. This recovery mechanism is unique to nanoporous reservoirs and is a product of both nanoconfinement and thermodynamics. A trade-off of this strategy would be the relatively high CO<sub>2</sub> to oil ratio in the produced fluids, which can be remedied by surface-based thermal separation and reinjection of CO<sub>2</sub>.

For the high pressure reservoir case (10 MPa), the oil displacement process is uniformly film-wise throughout, exhibiting highly efficient oil recovery with only 1 MPa driving pressure difference (~100% cumulative oil recovery percentage, Figure 35C). For miscible flooding, the interfacial tension between gas (here CO<sub>2</sub>) and oil is significantly reduced (approaching zero). The oil capillarity in nanoporous media is thus minimized compared to immiscible flooding. For an additional comparison, we also tested the efficiency of N<sub>2</sub> flooding at 11 MPa, with oil reservoir pressure kept at 10 MPa. We found that there was no flooding observed, in keeping with the earlier

finding that  $\sim 2$  MPa differential is required for Nitrogen to overcome the capillary pressure inherent to the nanoporous media. Further increasing the  $N_2$  pressure to 12 MPa achieved flooding, however, the cumulative oil recovery percentage was only 31%, which is much lower than all the  $CO_2$  miscible flooding results. In addition to reducing capillary force, the diffusion of  $CO_2$  into the oil phase also eases the flow of oil by reducing the oil viscosity (the viscosity of supercritical  $CO_2$  being two orders of magnitude lower than that of the oil).

Together, these  $N_2$  and  $CO_2$  flooding results indicate the importance of engineering nanoporous EOR interventions to ensure miscibility, or partial miscibility in these reservoirs. The minimum miscibility pressure value measured at bulk scale is reasonably representative at the  $\sim 60$  nm pore scale used here, and can serve as a general guide to understanding EOR effectiveness in these systems. While miscibility is generally helpful in conventional reservoirs, the elimination of capillary force barriers is paramount in unconventional, nanoporous reservoirs. The strength of these capillary forces can be additionally leveraged in a hybrid miscibility strategy where the gas is injected above MMP such that gas breakout occurs within the pore space, driving oil to the producer. This is a viable nanoporous EOR strategy demonstrated here, with no analog in conventional operations.

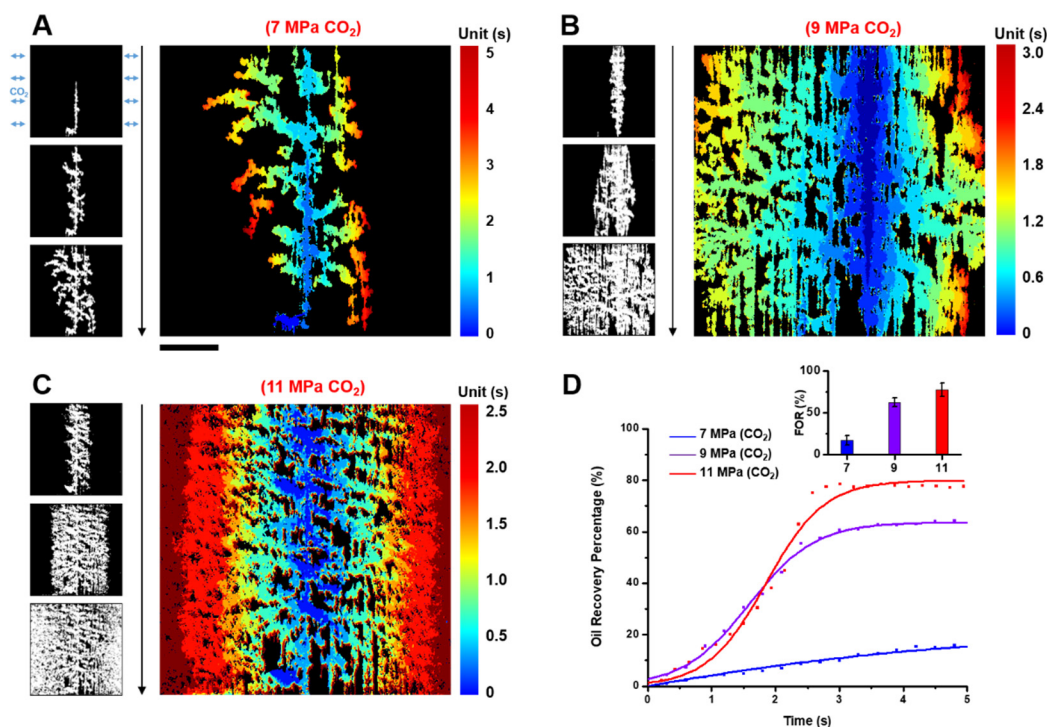


Figure 36 Screening conditions for  $CO_2$  huff-and-puff in a shale nanomodel.  $CO_2$  was initially injected into the nanomodel (filled with oil) at (A) 7, (B) 9 and (C) 11 MPa, respectively (huff). The scale bar represents  $200 \mu m$ . After soaking for one hour, the system pressure was rapidly reduced to 1 MPa (Puff). Oil was produced from the nanomodel during the production process, with (D) accumulative oil recovery changing with time plotted. The inset figure shows the final oil recovery percentage (FOR) at different injecting  $CO_2$  pressures. The error bar is from three independent nanoporous media.

Traditional gas flooding requires continuous gas injection into the reservoir, with associated costs in terms of pumping energy, facilities, and gas usage. Flooding also necessitates the use of at least two wells for injection and production. Huff-and-puff is an iterative, single-well alternative to traditional flooding where gas is injected for a time, allowed to soak into the reservoir, and then the mixture is produced from the same well. This method is gaining traction with tight oil and shale producers, with pilot field tests in the Bakken formation<sup>40</sup>. However the overall performance on improving oil recovery has not been significant to date due to gas leakage issues. The fundamental potential for huff-and-puff in shale is thus of both academic and industrial interest<sup>29</sup>. We reproduce this process in the nanomodel with the configuration shown in Figure 1B. After filling the nanoporous media with oil and cleaning the adjoining microchannels, we injected CO<sub>2</sub> symmetrically at the target pressure (5, 7, 9 or 11 MPa) and sealed for 1 hr to allow sufficient CO<sub>2</sub> to diffuse into the oil. The system was then depressurized (~20 s) to 1 MPa to produce oil from the nanomodel. The pressure conditions chosen here are similar to previous shale core tests reported.

Production results from initial injection pressures of 7, 9, and 11 MPa in the huff-and-puff strategy are shown in Figure 36A-C. All three cases show significant production, with the miscible (11 MPa) injection case showing the highest sweep efficiency with more interconnected and film-wise displacement, especially near the injection channels. The cumulative oil recovery (Figure 16D) is increased from 17% at 7 MPa to 77% at 11 MPa. In all cases gas breakout and expansion within the reservoir is a primary recovery mechanism. The miscible case outperforms due to a combination of increased CO<sub>2</sub> input and associated viscosity reduction, as well as significant initial direct extraction of light hydrocarbon components during injection. These measurements are in very close agreement with a previous core test (Eagle Ford formation), where miscible CO<sub>2</sub> injection at 10 MPa improved the oil recovery efficiency from ~20% of immiscible CO<sub>2</sub> injection at 6 MPa to ~70%.

While the cases shown in Figure 36 all show recovery, it is equally informative to consider running conditions that were ineffective. Firstly, lower injection pressure (5MPa) resulted in negligible production, and secondly, lower pressure drawdown rates (~ 200s) resulted in negligible production at all test pressures. At lower injection pressures, the main issue is capillary pressure in nanoconfinement decreasing the CO<sub>2</sub> solubility, and ultimately reducing the density of CO<sub>2</sub> in the oil below that needed form a gas bubble. Specifically, at 5 MPa the oil pressure was actually 4 MPa due to capillary pressure drop across the interface, and the CO<sub>2</sub> concentration in the oil reaches a maximum of 25 kg/m. Even with significant pressure drawdown this density is insufficient to overcome nanoconfinement capillary force and form bubbles. In contrast, with CO<sub>2</sub> at 7 MPa, the internal oil pressure would be 6.3 MPa, bringing the CO<sub>2</sub> concentration to 103 kg/m<sup>3</sup>, which is sufficient to drive bubble formation within the nanoporous media upon drawdown. Lower drawdown rates also proved ineffective at all injection pressures. Reducing from injection to production pressure over 200 s (vs. 20 s as shown in Figure 36), resulted in no observable oil recovery. The key mechanism here is gas diffusion out of the nanoporous media during drawdown. If pressure reduction is slow, CO<sub>2</sub> diffusion out of the oil can reduce the concentration to below that required to generate a gas bubble internally. In short, huff and puff in nanoconfinement relies on an asymmetry: during injection phase one must provide sufficient time and gas pressure for deep diffusion of CO<sub>2</sub>, and during production, one must provide insufficient time for diffusion.

To relate these results to similarly nanoporous reservoirs in the field, the mechanisms identified here are relevant but must be adjusted for the much larger length- and timescales. Specifically, the

distance between wells in shale reservoirs is  $>10$  m, and the time to approach the equilibrium dissolved gas concentration via diffusion through a nanoporous media of this scale is a prohibitively long  $10^9$  s, or  $\sim 32$  years. Thus in practice  $\text{CO}_2$  reach into the reservoir is finite, and optimizing this process requires compromise, balancing the injection pressure, injection/soak time to achieve sufficient  $\text{CO}_2$  density near the well. In this case, the nanomodel results show clearly the importance of having a sufficient drawdown rate in order to ‘beat’ local diffusion of  $\text{CO}_2$  back out the nanoporous matrix. These results resolve a general debate regarding drawdown rates (low vs. high) with both physical evidence and key mechanisms resolved. Another example of field-scale utility of the nanomodel testing is in measuring, and mitigating, the many impacts of nanoporous capillary pressure – a field relevant variable replicated at scale in our device. The huff-and-puff results here show the dual role of capillary pressure in limiting solubility and increasing the barrier to gas phase formation unique to nanoporous reservoirs. Likewise results from bulk scale solubility tests and microporous EOR pilots are thus likely to overestimate the total amount of gas dissolved in nanoporous reservoirs, and must be reconciled with the many implications of nanoporous capillary pressure clearly resolved in the nanomodel.

### Component 7: 2-D nanogrids in simulating shale gas primary recovery

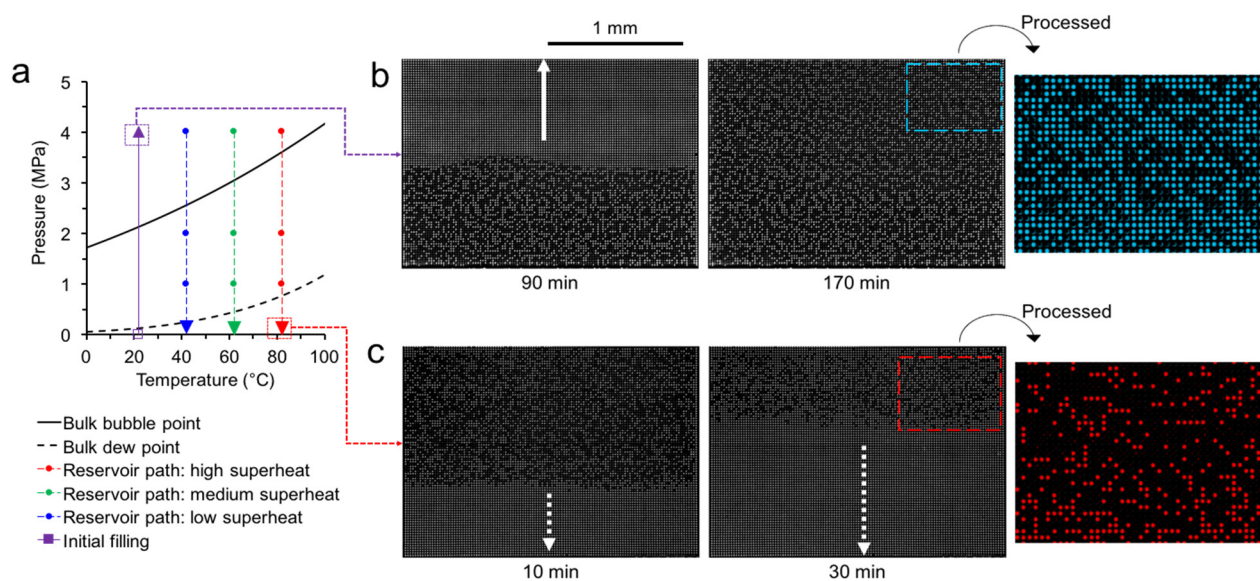


Figure 37 Experimental method overview, showing filling and evaporation conditions and dynamics in the shale nanomodel. (a) Bulk pressure-temperature plot for the C1-C3-C5 mixture (0.1/0.4/0.5 mol. fraction) (b) Initial filling of the nanomodel with the mixture sample at 4 MPa. Dark circles are liquid-filled pores while bright circles are empty or isolated pores. The solid white arrow represents the liquid-filling direction. The processed image portion shows liquid-filled pores colored blue. (c) Images taken during the vaporization process at high superheat. The dashed white line represents the direction of vapor transport. The processed image portion shows all connected vaporized pores in red.

The hydrocarbon mixture was chosen to reflect a typical liquid-rich natural gas stream with 10% methane, 40% propane and 50% pentane (mole fraction). The phase diagram of the prepared

mixture sample is presented in Figure 37a. After vacuuming the nanomodel for three hours, the hydrocarbon mixture was injected into the chip above the bulk bubble point pressure at room temperature as indicated by the purple line in Figure 37a. Figure 37b shows the nanomodel during and after the filling process. Additionally, an image following processing shows the liquid saturated pores in blue and isolated pores in grey at the end of the filling process. Once injected, liquid quickly filled the supply microchannel and slowly started flowing into the nanoporous media from the inlet. At a filling pressure of 4 MPa, the total filling time was approximately 3 hours. During this process, time-lapse images were recorded every 2 minutes. The spatio-temporal map illustrating the filling dynamics at 4 MPa is shown in Figure 38a. The filling proceeds in a fairly uniform fashion. Figure 37b shows pore-scale observations of the filling process in a 3 x 2 set of pores midway in the filling process. Initially the pores are empty. As filling progresses, grey liquid films first coat the large nanopore boundaries before completely filling the large nanopore. These filling dynamics can be attributed to corner-flow effects characteristic of micropores. Figure 37c shows the percentage of filled pores as a function of time with 4 MPa filling pressure. Additionally, Figure 37c also plots the Hagen-Poiseuille predicted filling rate using a simplified physical model of large nanopores series-connected by singular 5-nm throats. The time required to fill a large nanopore through a 5-nm throat is determined by relating the volume of a large nanopore to the volumetric velocity in the upstream set of liquid-filled 5-nm throats. The calculation results in a series of step-functions with a general square-root-of-time dependence that is typical of filling problems. The horizontal steps represent the time necessary to fill a large nanopore with liquid and the vertical jumps represent the relatively fast filling of 5-nm throats. In contrast to the analytically predicted case, the experimentally observed filling process was approximately four times slower and highly linear with respect to time. We attribute this delayed, and more constant liquid filling rate to evaporation of lighter components, particularly at earlier times, at the liquid front – an effect not captured by the analytical model. To remove any potential concentration gradients resulting from the filling process, the chip was left to equilibrate for ~ 12 hours prior to running the evaporation experiments.

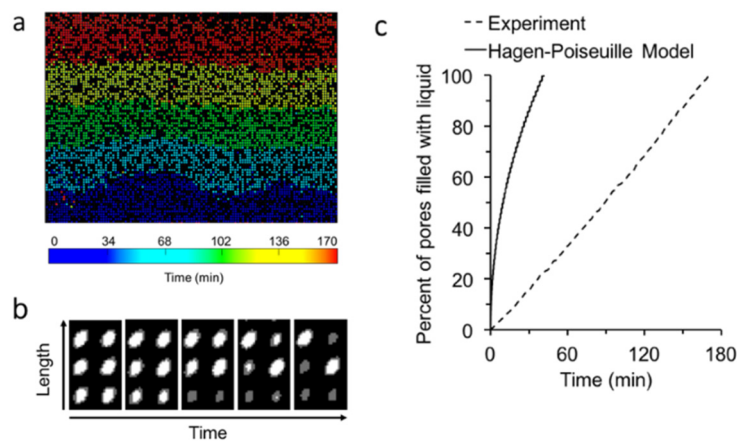


Figure 38 Liquid filling dynamics in the nanomodel. (a) Spatio-temporal progression of chip filling at 4 MPa. Color represents relative time at which a pore fills with liquid (b) Pore-scale visualization of filling in a 3 x 2 set of pores at ~70 minutes. Each image is taken after an interval of two minutes. (c) Global filling dynamics at 4 MPa in the nanomodel shows a linear dependence on time in contrast to the Hagen- Poiseuille prediction.

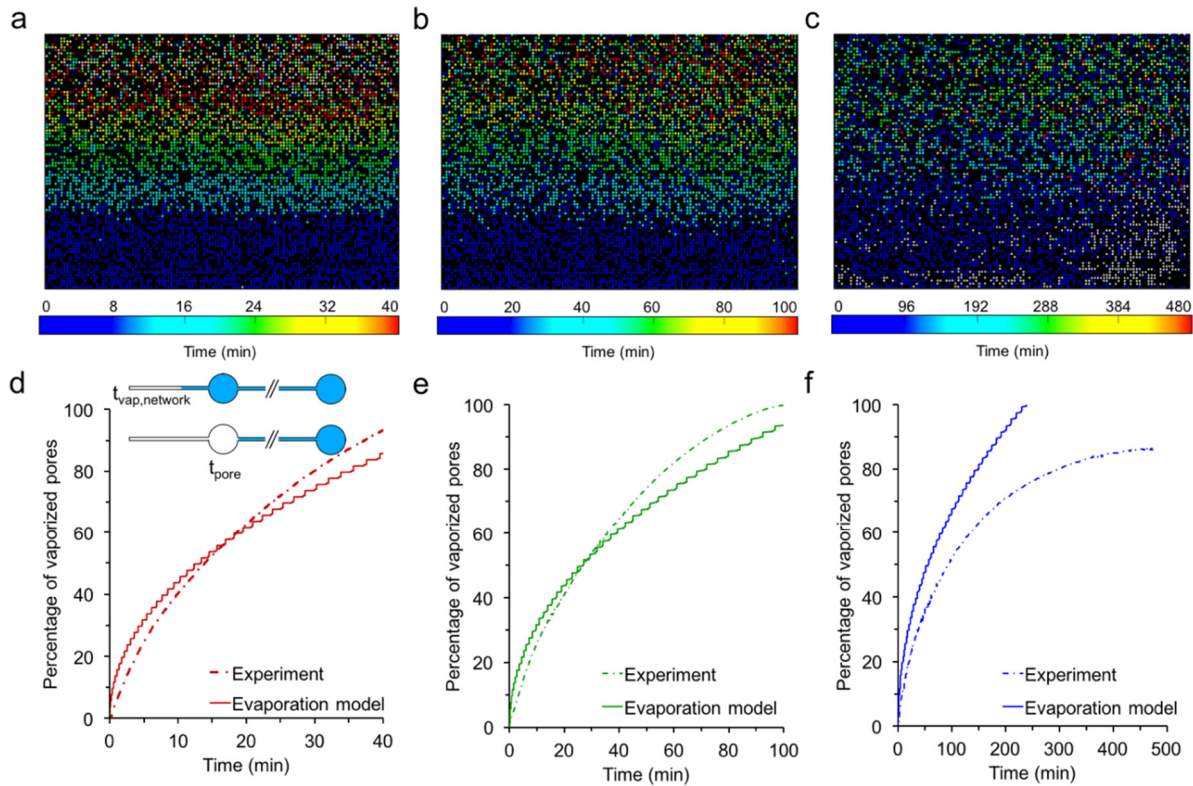


Figure 39 Spatio-temporal progression of vaporization events in the nanomodel. Each panel is 2 mm in width and 1.5 mm in length and contains  $\sim 5800$  connected pores. All isolated pores have been subtracted from the image. Grey pores represent pores that remained saturated with liquid and did not vaporize in the time period (a-c) Map showing dynamics in the high-superheat run  $\sim 0.76$  MPa, medium-superheat run  $\sim 0.44$  MPa, and low-superheat run  $\sim 0.25$  MPa. (d-f) Comparison of vaporization progression determined through experiment and vapor transport governed evaporation model as a function of time corresponding to high superheat, medium superheat and low superheat. Each data experiment was repeated twice. Inset image in (d) shows a simplified schematic of geometry used to calculate the evaporation dynamics (top-view). The time taken for vapor flow through the small pore network,  $t_{vap, network}$ , is calculated by determining the volumetric flow rate through small pores using a resistance model containing both Knudsen flow resistance and viscous flow resistance contributions. The time taken to transport vapor volume held in a large pore,  $t_{pore}$ , is calculated by using the small pore network volumetric flow rate and the volume of a large pore.

Once the entire chip was saturated with liquid and equilibrated, drawdown pressure was initiated under isothermal conditions. The system temperature was controlled by electric heating elements, at  $82.5^\circ\text{C}$ ,  $62.5^\circ\text{C}$  and  $42.5^\circ\text{C}$  for cases of high, medium and low superheat. After the temperature stabilized, the pressure was lowered stepwise as shown in Figure 37a. Time-lapse images of the process were recorded every 10 seconds. At each solid circle in Figure 19a we set a waiting time of 15 minutes to observe potential phase change. In a control experiment, we waited for 60 minutes

and observed similar results. As the pressure was lowered below the bulk bubble point, vapor bubbles started to appear in the microchannel with no detectable change in the nanomodel. This result is similar to that observed in recent experiments in single 1-D nanochannels and associated density functional theory modelling where a two-phase envelope was not observed for hydrocarbon binary mixtures at steady-state, and pressures below the bulk dew point were required for vaporization in sub-10nm channels.

Figure 39 shows the spatio-temporal dynamics of vaporization for the three conditions (from high superheat to low superheat) showing markedly slower and less spatially uniform vaporization fronts at reduced superheats. The high superheat case (Figure 39a) exhibited a vaporization front that initiated from the inlet of the nanomodel and progressed quite uniformly into the nanomodel. In the medium superheat case (Figure 39b) vaporization events were commonly observed ahead of the vaporization front. Vaporization ahead of the front has previously been reported in nanoporous media as a result of pre-pressurization conditions, and slow drying rates in single-component systems. Here, this effect is attributed to lighter components preferentially vaporizing ahead of the front. In contrast to the high and medium superheat cases, vaporization in the low superheat case (Figure 39c) was slower and scattered throughout the media. After 480 minutes, approximately 760 pores (~14% of large pores), remained saturated with liquid. These were mainly grouped near the entrance of the nanomodel and are colored grey in Figure 39c.

Figure 39d, e and f plot the percentage of vaporized pores as a function of time for all three superheat conditions (from high to low superheat). All cases exhibit a square root of time dependence. For comparison, analytical results are plotted from a vapor transport resistance model that includes the serially connected geometry (inset in Figure 39d). In the model, we assume a pure substance, and evaporation limited only by vapor transport resistance in the 5-nm pores wherein the transport is comprised of both Knudsen flow and viscous flow components acting in parallel.

The cumulative evaporation dynamics are stepwise with an overall square root of time dependence. The horizontal steps indicate the emptying time for the volume in the large pores while the jumps indicate the relatively fast transport of vapor in the 5-nm network. A longer time is required to empty each successive large pore as the transport resistance through the 5-nm network progressively increases. The step-wise growth is indicative of the fact that production of vapor from large pores is mainly limited by the transport resistance in the small throats. As an example, for the high superheat case, the model predicts a vaporization time of ~48 minutes. However, without the gating 5-nm throat network the model predicts vaporization in a simple channel with depth matching the large pores (82-nm deep, 1.5 mm in length) to be less than 1 second at otherwise similar conditions. This 3000-fold difference is a result of the mixed geometry alone, that is, large pores gating by small throats. Likewise, the vaporization time in a simple channel of nanoscale throat depth (5.5-nm deep, 1.5 mm in length) is only 50 s. This calculated time is of similar magnitude to that measured experimentally for evaporation in ~9 nm deep 2D nanopores. These differences highlight the strong influence of mixed geometries, and suggest that work to

date in single-depth nanochannels or networks would tend to overestimate transport as compared to real shale reservoirs where multiple length scales are the norm.

The simplified evaporation model adequately describes the experimental results for the high superheat cases at 0.76 MPa and 0.44 MPa. In these cases, the relatively high evaporation driving force leads both light and heavy components to vaporize readily from the nanopore inlet as evidenced in the spatio-temporal plots in Figure 39a and b. In these cases the dual-mixture problem is reduced to a single mixture problem, that of mixed geometry. The dynamics are thus mainly governed by vapor transport and rightly captured in the model. However, in the low superheat case (0.25 MPa), experimental results indicate additional delays in vaporization not captured by the pure-substance analytical model. Specifically, the model overpredicts the vaporization dynamics especially at later times (30% deviation between model and experimental data at ~200 min). At low superheat, we expect lighter components to preferentially cavitate throughout the nanomodel enriching liquid within the nanoscale throat network with heavier pentane that is slower to vaporize (for reference, in bulk systems and at ambient pressures, the vaporization points of methane, propane and pentane are  $-161.5^{\circ}\text{C}$ ,  $-42^{\circ}\text{C}$  and  $36.1^{\circ}\text{C}$ , respectively). The evaporation model prediction for pure pentane trends towards the experimental data obtained for the low superheat case. This indicates that methane and propane vaporize at early stages with the remaining liquid being pentane-rich). In this regard the mixture vaporization process is dominated by the thermodynamics of the heaviest component.

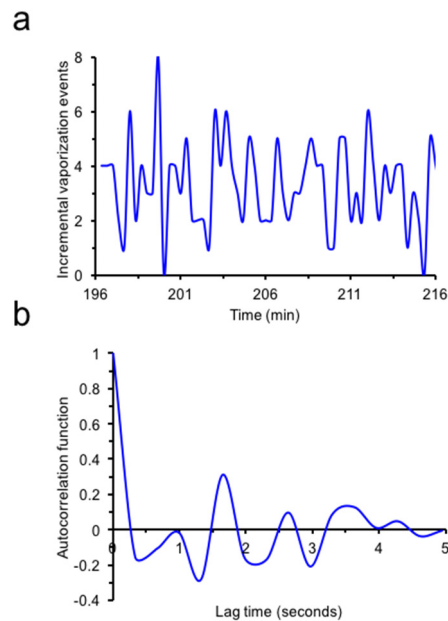


Figure 40 Spatio-temporal analysis of vapor formation behaviour for the low superheat case. (a) Example set of vaporization events for the low superheat case observed over time. Data points are collected every 0.3 seconds (b) Corresponding time series autocorrelation data

By resolving individual pore dynamics in the network, the nanomodel provides the opportunity to additionally assess the impact that local cavitation phase change has on surrounding pores. Vincent et al. observed such an influence by studying stochastic cavitation of pure water in a ink-bottle type system with an ordered array of very large pores (on the order of microns) above a bulk nanoporous media.<sup>2</sup> Their experimental system also showed that vapor bursting behavior was periodic with 1-7 events in quick succession followed by a ~15-minute period of no activity. Inspired by this finding, we analyzed the cavitation behavior obtained in the shale-relevant nanomodel to determine if phase change in pores influenced near-by pores with results shown in Figure 40a. In our system, vaporization is relatively continuous and does not show the dramatically periodic behavior observed by Vincent et al. We do note that incremental number of emptying pores as a function of time and the corresponding time series autocorrelation function followed an oscillatory pattern as shown in Figure 40b, however, we conclude that in this system phase change in a given pore was largely independent of phase change in neighboring pores. Differences with the system of Vincent et al. include higher superheat levels and less extreme difference in the pore geometry in the shale-inspired cases studied here. Collectively, the results here illustrate that complex dual-mixture effects, resulting from the confinement of multi-component fluids in multi-scale nanopores, are central to the study of phase change as relevant to shale gas production.

### Key Alberta Innovates points:

- Nanofluidics allows direct observation of fluid behaviors down to an extreme sub-10 nm region, providing unique opportunity for shale relevant fluid study;
- At nanoscale, hydrocarbon fluid is preferential at liquid phase, proving by hydrocarbon early condensation and delayed vaporization compared to bulk;
- Hydrocarbon mixture phase behaviors in a nano-micro confinement deviate significant from the classical theory, specially the deeply reduced bubble point in nanoconfinement is found to be below bulk dew point;
- Hydrocarbon phase change dynamics at nanoscale is mainly governed by fluid mass transport instead of liquid-vapor interface dynamics at bulk;
- Miscible gas injections in shale reservoirs are promising in enhancing tight oil recovery, by limiting the extreme capillarity across injecting phase and oil;
- The effect of Huff-and-puff injections depends on multiple factors, including injecting gas pressure, soaking time and puff time, where gas diffusion matters;
- Huff-and-puff recovery with CO<sub>2</sub> found to be very effective at this scale
- Gas production within shale is extremely limited by sub-10 nm pore throat;
- The gas production dynamics can be quantitatively described through a transport resistance model, by taking the Poiseuille flow, Knudsen flow effect and pore throat effect into consideration.

## 3.5 Project outcomes

### 3.5.1 Training HQP's – Full project

HQP	Name	Role	Period	Current Status
M.A.Sc.	Arnav Jatukaran	Investigate dual porosity nanomodel in simulating shale gas production	May 2016 to July 2018	Currently at Schlumberger
PhD	Dr. Junjie Zhong	Investigate nanomodel in screening enhanced tight oil recovery	Start of the project to the end	Currently at PDF in Prof. David Sinton Group at University of Toronto
PhD	Dr. Bo Bao	Investigate cavitation and evaporation of hydrocarbons in nanochannels	Start of project to September 2016	Currently Assistant Professor at East China University of Science and Technology
PDF	Dr. Aaron H. Persad	Develop thermodynamic theory of phase-change at the nanoscale	June 2016 to June 2017	Currently PDF in Prof. Rohit Karnik group at Massachusetts Institute of Technology
PDF	Dr. Seyed Hadi Zandavi	Develop thermo-resistance and flow transport theory of phase-change at the nanoscale	Start of project to July 2016	Currently PDF in Prof. Gang Chen group at Massachusetts Institute of Technology
PDF	Dr. Huawei Li	Fabrication of sub-10nm nanochannels	Start of project to August 2016	Currently Assistant Professor at Guangdong University of Technology

**Table 5.** List of Highly Qualified Personnel trained during the project's second year.

HQP's have obtained the following skills through their work in this Alberta Innovates project:

### Micro/nanofabrication

- Utilized highly specialized clean room facilities at the University of Toronto for fabricating nanofluidic and microfluidic devices. The importance of these skills are that we are able to match the length scales typically observed during hydrocarbon extraction from shale and tight oil reservoirs.
- Specific techniques and equipment:
  - Deep-reactive ion etching (DRIE)
  - Wet etching
  - Anodic bonding
  - Dicer
  - Low pressure chemical vapour deposition (LPCVD)
  - Plasma enhanced chemical vapour deposition (PECVD)
  - Ellipsometer
  - Photolithography
- Developed characterization and imaging skills. The importance of these skills are that we are able to validate if the final device meets the design specifications (dimensions, roughness etc.)
  - Atomic force microscopy (AFM)
  - Scanning electron microscopy (SEM)
  - Optical profilometer
  - Optical microscopy

### Experimental skills

- Developed skills related to utilizing the nanofluidic devices for studying phase behaviour at the nanoscale at temperatures and pressures relevant to those observed in the reservoir.
- Adhered to strict safety policies and guidelines similar to those followed in the energy industry

### Analytical skills

- Thermodynamics and fluid mechanics, specifically phase behaviour at the nanoscale, are crucial to understanding and optimizing the hydrocarbon recovery process from shale reservoirs. Knowledge and skills in this area were developed by conducting literature reviews, designing experiments and through courses.

Working towards completing academic courses to complement research directly related to sustainable energy. This experience is important as it helps develop skills useful for tackling challenges related to ensuring the long-term environmental and economic sustainability of the energy industry.

### 3.5.2 Commercialization

The nanofluidic chip and setup developed during this project are now commercialized at an Alberta-based startup, Interface fluidics. The company is now providing shale fracturing fluid screening and nanoscale PVT test services, to both Canadian oil/gas companies and international oil/gas companies such as Exxon, BP, and Equinor, as well as chemical companies here and abroad.

**(\*\* see Relevance and Impact section below for more commercialization details \*\*)**

#### **Key Alberta Innovates points:**

- 6 HQP have received training in micro/nano fabrication, performing fluid transport and phase-change experiments, and analyzing and reporting their results in conferences and peer-reviewed publications;
- Two HQP has since received academic positions;
- Two HQP have since joined world-renowned energy groups;
- The project outcome has been successfully transformed to commercial services, providing worldwide unique nanoscale, shale-relevant fluid tests.

## 4. Relevance and impact

- **What do the project results mean for Albertans? Do the project results inform a provincial strategy, policy, regulation or operational practice? Have the results been shared with the relevant body (e.g., government, industry)?**

There are many outcomes of the project for Albertans:

Built on the expertise in micro/nanofluidics developed along this project, we founded an Alberta-based startup company - **Interface Fluidics Ltd** - that is providing shale oil/gas relevant services to companies worldwide. With ~ 20 people in a business office in Calgary and a lab in Edmonton, the company is growing rapidly. The company is all-Alberta, and an Alberta tech success story that is attracting business and investment worldwide. **On August 27, just 3 days before the official end of this project, Interface Fluidics secured \$4,500,000 USD (~ \$6M CAD) in international investment.**

While there are many factors attributed to Interface Fluidic's success, it is interesting to consider this recent investment in Alberta, in the context of AI's investment in this project. **The magnitude (> 2000% in cash) and the immediacy (before end of project) of this provincial investment payback is notable!** This success also speaks to the wisdom of AI investing in AB-relevant projects with good people and good ideas, beyond Alberta borders.

There are additional direct benefits for policy makers and industry more generally. Our experimental results indicate that oil and gas trapped within shale nanopores behave differently in phase change compared to bulk. The experimental conditions, including nanopore size distribution, temperature and pressure are directly relevant to Montney and Viking shale formations in Alberta. Therefore, the shale oil/gas operational PVT database should be updated based on the reservoir conditions, especially the pore size distribution for a specific reservoir, which serves as an important provincial field operational strategy.

The primary shale oil recovery efficiency is low (~5% of the resource). Conventional enhanced oil/gas recovery strategy could fail in improving shale resources efficiency, due to the extremely low permeability of shale (at nano- to microDarcy). Specially, the nanopore preferentially traps heavy oil phase in shale, where gas phase escapes from the micro fractures, leading to a further reduced liquid mobility in shale. Therefore, improving the gas content in nanopores after primary recovery to improve the oil mobility is an important strategy in enhancing shale oil production. Our results suggest the Alberta provincial technology policy should encourage relevant recovery strategy development, such as CO<sub>2</sub> or lean gas huff-n-puff.

- **Qualitative and quantitative (where possible) discussion about the economic, environmental, GHG and social benefits resulting from the completed project, including immediate benefits and potential future impacts.**

The most immediate and quantitative economic benefit to Alberta is the ~ \$6M CAD international investment into Alberta associated with our startup company, Interface Fluidics.

In addition, the economic potential of Alberta's shale gas and tight oil resources is very significant, and this research project informs operators, policy makers and the public on this potential and how it could be fully achieved. Perhaps most notably, improving shale oil production can maximize the overall profit for each well drilled. Our results directly prove that strategies like miscible gas flooding and huff-n-puff can contribute to a higher shale oil recovery factor. In terms of field practice, huff-n-puff is practical – and we have shown effective – at these scales. An increase of ~5% shale oil production from the resource is expected to double the economic payback, which is highly promising based on our nanofluidic experiments.

The resources studied here are also vast in the context of potential CO<sub>2</sub> emissions – both upstream and downstream. Our work informs on the upstream side, informing on the resource and helping operators reduce the emissions associated with recovery (which are substantial in these resources). Our results also show how the potential for CO<sub>2</sub> enhanced oil recovery style methods in tight oil recovery. Specifically, supercritical CO<sub>2</sub>, uniquely, enabled the efficient recovery of a tight oil mixture from a nanoporous media. This finding motivates an approach akin to that employed successfully in the Weyburn field (one of the largest CO<sub>2</sub> utilization projects in the world), to be applied to Alberta's nanoporous reservoirs. Our results also show how methane leakage is a concern for shale oil/gas production, as heavy components are trapped within shale nanopores, while light components (e.g., methane) leave shale through microfractures. The global warming potential of methane is ~90 times higher than CO<sub>2</sub> over 20 years.

In summary the impacts of the project are multifaceted, including direct financial investment in AB, AB-based tech development and excellence, specific knowledge on AB-based resources and methods to better understand the development of those resources and the potential for utilizing CO<sub>2</sub> in the process.

## 5. Overall conclusions and outlooks

The high pressure, high temperature silicon-glass nanofluidics developed in this AI project is a powerful tool in quantifying fluid behaviors at nanoscale. It is robust within a wide range of temperature and pressure conditions, and is highly compatible with the optical microscope to provide important real-time information. These benefits allow it to be commercialized for many industrial applications, especially in the shale oil/gas industry (e.g., Interface Fluidics Inc. located in Alberta, Canada). The mature fabrication technique guarantees a relatively low cost for the chip (\$100 to \$1000 per chip), with other apparatus highly accessible to the industry (e.g., optical microscope and ISCO pump). It has thus great potential compared to microfluidics in providing fast and parallel industrial relevant detections where nanoscale fluid behaviors matter (e.g., shale industry). Compared to the bulk PVT cell providing bulk PVT data for conventional reservoir fluids, the nanofluidic chip is a unique substitution where fluid PVT data at nanoscale matter, for example, recovering shale gas and tight oil stored in the nanoporous shale reservoir. These fundamental nanoscale fluid properties accurately detected by nanofluidic device can be also easily incorporated with commercial simulators (e.g., UTcomp) to improve the accuracy of simulation predictions. These potentials are demonstrated here through components 1-5.

The nanofluidic device can efficiently validate shale industrial relevant recovery strategies, such as gas injections for enhanced tight oil recovery, fracture fluid trapping during reservoir fluid flowback within the shale nanopores as well as effectiveness of different surfactants in nanoconfined reservoir fluids. These engineering contents are now mostly tested in black-box bulky core sample, with experimental results hard to be repeat due to the randomness of shale core samples in terms of the pore size distribution and surface condition. The nanofluidic device can identically reproduce the designed nanopore size distribution as well as nanopore surface condition, by which is capable of accurately capturing fluid interactions at nanoscale with highly repeatable results. The much less fluid volume in the nanofluidic chip compared to that is required in the shale core sample also permits fast response to any change within nanopores for a time efficiency in each test. By directly observing the in-situ results from the nanofluidic device (instead of a black-box core system), one can not only obtain simple inputs and outputs, but also understand a reasonable trend based on fundamental fluid behaviors in nanopores to efficiently improve the test. The compatibility to image results indicate the great potential of an artificial-intelligence-guided nanopore scale fluid test as well. These potentials have been demonstrated here through components 6-7.

Overall, the current nanofluidic approach targeting on shale application creates a simplified and idealized nanoporous system, that can serve as test bed with which operators and service companies can assess the effectiveness of recovery strategies and chemical treatments. Critically, the device allows a window into these complex, incredibly small porestructures – a unique capacity of this technology.

More broadly than oil and gas and subsurface CO<sub>2</sub> utilization applications, there are many other nanoporous systems confining important fluids/molecular species, such as the nanoporous catalyst in chemical reactions. The nanofluidic chip is a good platform in deeply understanding the fundamental mass transport mechanisms, and optimizing nanoporous structures to further enhance chemical reactions. The nanofluidic device is also able to create environment for a single molecular level detection and reaction, for example in detecting genes on a DNA string, as well as protein synthesis. Compared to microfluidics, nanofluidics is still a young field, and the findings and methods developed here are expected to inform a broad range of applications on the long term.

## 6. Next steps

One direct next step is to build on the success of this project, and associated commercialization at **Interface Fluidics**, and propose a co-funded project with Interface Fluidics and AI that would enable our lab to further develop and commercialize some of the technologies seeded here.

Another next step for my academic lab is to move beyond chemical/process effectiveness testing into industrial fluid *design*. Specifically we are applying what we learned in high pressure fluid handling through this project, and integrating machine learning and automation to develop technology that can design and optimize working fluids for heavy industry. The first project anchoring this new approach is funded by an **Alberta-based startup - Eavor technology** – and focuses on developing phase change slurry for high efficiency geothermal recovery. The key novelty of this project is combining the high-throughput micro/nanofluidics and the data-hungry artificial intelligence to automatically optimize the phase change slurry composition, for reaching a much higher geothermal recovery efficiency compared to conventional water-based system in general. This project is very relevant to AI goals and existing AI investments in this area, and an AI-match to the Eavor research funding would greatly accelerate this project, for near-term commercial and environmental impact in Alberta.

## 7. Scientific achievement

In addition to the detailed descriptions above, the scientific accomplishments of this project are documented in a distinguished list of publications. The relative prestige of these journals is very high – as quantified by the object measure of journal impact, impact factor. Most notably the impact factor of *ACS Nano* is ~ 14 while the average for mechanical engineering journals is ~ 1-1.5. Based on the strength of these contributions, the team was invited to submit a full article to the prestigious review journal *Accounts of Chemical Research*. That submission is being reviewed now, and if finally accepted will add to the list below with an impact factor of 21.

### Published in peer-reviewed journals

1. Jatukaran, A., Zhong, J., Abedini, A., Sherbatian, A., Zhao, Y., Jin, Z., Mostowfi, F. and Sinton, D. Natural Gas Vaporization in a Nanoscale Throat Connected Model of Shale: Multi-scale, Multi-component and Multi-phase. *Lab Chip*, 2019, 19, 272. (Featured by editor as top 10% HOT papers published in Lab on a Chip)
2. Zhong, J., Abedini, A., Xu, L., Xu, Y., Qi, Z., C., Mostowfi, F. and Sinton, D. Nanomodel Visualization of Fluid Injections in Tight Formations. *Nanoscale*, 2018, 10, 21994.
3. Hasham, A.A., Abedini, A., Jatukaran, A., Persad, A. and Sinton, D. Visualization of fracturing fluid dynamics in a nanofluidic chip. *Journal of Petroleum Science and Engineering*, 2018, 165, 181-186.
4. Zhao, Y., Wang, Y., Zhong, J., Xu, Y., Sinton, D and Jin, Z. Bubble Point Pressures of Hydrocarbon Mixtures in Multiscale Volumes from Density Functional Theory. *Langmuir*, 2018, 34, 14058.
5. Zhong, J., Zhao, Y., Lu, Xu, Y., Jin, Z., C., Mostowfi, F. and Sinton, D. Nanoscale Phase Measurement for the Shale Challenge: Multicomponent Fluids in Multiscale Volumes. *Langmuir*, 2018, 34, 9927.
6. Jatukaran, A., Zhong, J., Persad, A.H., Xu, Y., Mostowfi, F. and Sinton, D. Direct Visualization of Evaporation in a Two-Dimensional Nanoporous Model for Unconventional Natural Gas. *ACS Appl. Nano Mater*, 2018, 1, 1332.
7. Zhong, J., Talebi, S., Xu, Y., Pang, Y., Mostowfi, F. and Sinton, D., Fluorescence in Sub-10 nm Channels with An Optical Enhancement Layer. *Lab Chip*, 2018, 18, 568.
8. Zhong, J., Riordon, J., Zandavi, S.H., Xu, Y., Persad, A.H., Mostowfi, F. and Sinton, D., Capillary Condensation in 8-nm Deep Channels. *J. Phys. Chem. Lett.*, 2018, 9, 497.
9. Zhong, J.\*, Zandavi, S.H.\*, Li, H., Bao, B., Persad, A.H., Mostowfi, F. and Sinton, D., Condensation in One-dimensional Dead-end Nanochannels. *ACS Nano*, 2017, 11, 304.

10. Li, H., Zhong, J., Pang, Y., Zandavi, S.H., Persad, A.H., Xu, Y., Mostowfi, F., Sinton, D., Direct Visualization of Fluid Dynamics in Sub-10 nm Nanochannels. *Nanoscale*, 2017, 9, 9556.
11. Bao, B., Zandavi, S.H., Li, H., Zhong, J., Jatukaran, A., Mostowfi, F. and Sinton, D., Bubble Nucleation and Growth in Nanochannels. *Phys. Chem. Chem. Phys.*, 2017, 19, 8223.